

DISSERTATION

ORGANIC FLUXES AS A TOOL FOR SOLID-STATE SYNTHESIS

Submitted by

M. Jewels Fallon

Department of Chemistry

In partial fulfillment of the requirements

For the Degree of Doctor of Philosophy

Colorado State University

Fort Collins, Colorado

Summer 2022

Doctoral Committee:

Advisor: James R. Neilson

Richard G. Finke

Carmen S. Menoni

Kristen S. Buchanan

Copyright by M. Jewels Fallon 2022

All Rights Reserved

ABSTRACT

ORGANIC FLUXES AS A TOOL FOR SOLID-STATE SYNTHESIS

Solid-state materials allow us to charge our phones, store information on a computer, and harvest energy from the sun, among many other applications. They are the backbone of many modern technologies. However, making solid-state materials remains challenging. Traditional solid-state synthesis involves heating materials up to high temperatures to promote reactivity. These high temperatures make controlling the reactions and directing product formation difficult, as they generally form products that are stable at those high temperatures. There are limited techniques to make solid-materials, especially those that are not stable at high temperatures. In order to advance modern technologies based on solid-state materials, more well-understood, controllable synthetic techniques are necessary.

This thesis describes a new technique for making solid-state materials. This technique is based on using molten organic materials, called organic fluxes, to enable selective reactivity between solids at lower temperatures. Owing to the lower reaction temperatures, this synthesis can form materials that are traditionally more difficult to make.

The concept of an organic flux is introduced through a case study where triphenylphosphine, the organic flux, is used to make the low-temperature phase of iron selenide. This study demonstrates the efficacy of organic fluxes and provides insight to their mechanism of reactivity. Then, triphenylphosphine fluxes are further explored through reactions involving other metal chalcogenide binaries. By analyzing a variety of systems, the guiding principles behind the reactivity of triphenylphosphine fluxes are determined. Next, the ability of organic fluxes to aid materials discovery is shown through the formation of a new cobalt-selenium-triphenylphosphine complex. Finally, preliminary work exploring other organic fluxes and the future prospects for this synthetic scheme are discussed.

This research introduces a new technique to target low-temperature materials. The tunability of organic fluxes enables the design of synthesis for selective reactivity in the solid-state. Adding to the library of synthetic tools available to solid-state chemists is a step towards materials discovery and the advancement of technologies based on solid-state materials.

ACKNOWLEDGEMENTS

This research would not have been possible without the support and guidance I received from so many people along the way. I truly cannot express my gratitude to everyone who has helped me along this journey.

First and foremost, I want to thank Jamie for his incredible mentorship. Without the guidance, patience, and encouragement from Jamie, I would not have made it this far. Jamie handled my many breakdowns with so much understanding and never lost faith in me. He has been an outstanding PI who balanced pushing me to do my best with supporting me in a way that made me a better researcher, mentor, and person. I am endlessly grateful for all that he has taught me about science and about life.

I would like to thank both my past and present committee members: Rick Finke, Carmen Menoni, Kristen Buchanan, Alan Van Orden, and Jose de la Venta. I appreciate the advice, feedback and encouragement throughout my time here. I especially want to thank Rick for all the support. Rick has always been there for me with helpful advice anytime I've struggled with something, either work-related or in my personal life, and I am very grateful.

I would also like to thank the National Science Foundation (DMR-1653863) for funding my research during graduate school.

I want to acknowledge my undergraduate research advisor, Chuck Williamson. Thank you for laying the groundwork for who I am as a scientist and presenter.

Thanks to all the Neilson lab members who have been present throughout my time at Colorado State University. I am grateful for the guidance and encouragement in lab as well as the friendships and shenanigans outside of work. Thank you for the many research discussions, pomodoros, game nights, puzzle parties, craft nights, and late nights talking about random stuff.

I am also grateful for all the friends who have been there for me through this point. To my friends from before graduate school: thank you for the baking parties, trips to SF, late night conversations, and most importantly, the constant support and patience. To the chemists I have met

during graduate school: thank you for all the helpful discussions, brunches, hikes, and other adventures. To the climbers: thank you for the many hours hanging out in the gym, adventures to Carter lake, hot tub conversations, and encouragement when I needed it the most.

To Clara: thank you for all the encouragement and support in every aspect of my life. I would not have gotten to this point without you. You helped motivate me, keep me focused when I had to be, and distract me when I needed it. Thank you for the many years of studying together, helpful discussions, hiking, kitchen floor chats, cooking, and the rest of our crazy adventures. You have made me a better person and I cannot thank you enough.

Lastly, I want to thank my family for everything. I am incredibly grateful for the endless love and support. Who else is going to hang up a framed copy of your first publication (I love you, Mom) or drive 2,430 miles in less than 48 hours to make sure you can come home for the holidays (I love you, Dad and Paul). Thank you for always believing in me, sending me cards, board games, and scones when I was struggling, being there to celebrate my successes, and teaching me all the tough lessons. I would not be the person I am today without you all. So again, thank you for everything.

DEDICATION

I would like to dedicate this thesis to my family, both chosen and given.

TABLE OF CONTENTS

ABSTRACT	ii
ACKNOWLEDGEMENTS	iv
DEDICATION	vi
LIST OF TABLES	ix
LIST OF FIGURES	x
Chapter 1	Introduction 1
1.1	Challenges of low-temperature solid-state synthesis 1
1.1.1	Techniques for solid-state synthesis are limited 1
1.1.2	Challenges accessing low-temperature phases 2
1.2	Techniques for low-temperature materials synthesis 4
1.2.1	Flux-based low-temperature materials synthesis 5
1.3	Organic flux synthesis 7
Chapter 2	Low-Temperature Synthesis of Superconducting Iron Selenide Using a Triphenylphosphine Flux 10
2.1	Overview 10
2.2	Introduction 11
2.3	Experimental 12
2.4	Results and Discussion 15
2.5	Conflicts of interest 20
Chapter 3	The Reactivity of Triphenylphosphine Fluxes in the Synthesis of Metal Chalcogenides 23
3.1	Overview 23
3.2	Introduction 24
3.3	Experimental 25
3.3.1	Synthesis 25
3.3.2	High dimensional data analysis and feature selection 26
3.4	Results and Discussion 28
3.4.1	Thermodynamic hypothesis based on phase diagrams 29
3.4.2	Exploring kinetic factors 32
3.4.3	Creating a model to predict reactivity 35
3.5	Conclusions 38
Chapter 4	A New Cobalt-Selenium-Triphenylphosphine Cluster Synthesized with a Triphenylphosphine Flux 40
4.1	Overview 40
4.2	Introduction 40
4.3	Experimental 42
4.3.1	Synthesis 42

4.3.2	Crystallization attempts	42
4.3.3	Matrix-Assisted Laser Desorption/Ionization Mass Spectrometry (MALDI-MS)	43
4.3.4	X-ray diffraction	44
4.3.5	Fourier transform infrared spectroscopy	44
4.3.6	Magnetism	45
4.3.7	Ultraviolet-Visible spectroscopy	45
4.4	Results	45
4.5	Discussion	51
4.5.1	Hypothesis: $\text{Co}_{12}\text{Se}_{16}(\text{PPh}_3)_{10}$ Cluster	51
4.5.2	Alternate Hypothesis 1: Selenium radical	54
4.5.3	Alternate Hypothesis 2: Cobalt Selenide	55
4.6	Conclusions	57
Chapter 5	Preliminary Results Exploring Other Organic Fluxes	58
5.1	Overview	58
5.2	Introduction	58
5.3	Experimental	59
5.4	Results and discussion	59
5.5	Conclusion	60
Chapter 6	Conclusions and Future Directions	62
6.1	Summary of organic flux reactions	62
6.2	Future directions for organic fluxes	64
Bibliography	66
Appendix A	Supplemental Information: Low-Temperature Synthesis of Superconducting Iron Selenide Using a Triphenylphosphine Flux	75
Appendix B	Supplemental Information: The Reactivity of Triphenylphosphine Fluxes in the Synthesis of Metal Chalcogenides	79
Appendix C	Python Code: The Reactivity of Triphenylphosphine Fluxes in the Synthesis of Metal Chalcogenides	87
Appendix D	Overview of Other Contributions	124
Appendix E	Jargon-Free Research Overview	126
Appendix F	Photos of Colorado	128
LIST OF ABBREVIATIONS	129

LIST OF TABLES

3.1	Table of the attempted triphenylphosphine flux reactions, the dwell times, products, and no-flux control reaction products. Mole percents, as determined through Rietveld analysis, are written in parentheses for the reactions where there were multiple products. Table continued on following page.	30
3.2	Table of the attempted triphenylphosphine flux reactions, the dwell times, products, and no-flux control reaction products. Mole percents, as determined through Rietveld analysis, are written in parentheses for the reactions where there were multiple products. Continued from previous page.	31
3.3	Table of test reactions including the features, predicted outcome, and actual outcome. Continued below.	38
3.4	Table of test reactions including the features, predicted outcome, and actual outcome. Continued below.	39
3.5	Table of test reactions including the features, predicted outcome, and actual outcome. Continued from above.	39
A.1	Phase fraction (mol%) determined through Rietveld analysis of PXRD patterns of products formed from reactions with varying fluxes.	75
A.2	Inorganic reaction products across the ternary Fe-Se-PPh ₃ phase space. Phase fraction (mol%) are written in parentheses.	77
A.3	Formation energies accessed from the Materials Project (Date: 5/16/2019). [1]	77
B.1	List of the sources and purity of each reactant used.	80
B.2	Energies of the chalcogen and chalcogen adducts from DFT calculations.	80
B.3	Table of the chemical properties used to analyze the reactivity of these systems. Continued on following pages.	81
B.4	Table of the chemical properties used to analyze the reactivity of these systems. Continued from the previous page.	82
B.5	Table of the chemical properties used to analyze the reactivity of these systems. Continued from the previous page.	83
B.6	Table of the chemical properties used to analyze the reactivity of these systems. Continued from the previous page.	84
B.7	Table of the chemical properties used to analyze the reactivity of these systems. Continued from the previous page.	85
B.8	Table of the chemical properties used to analyze the reactivity of these systems. Continued from the previous page.	86
B.9	Table of all the algorithms explored and their accuracy.	86

LIST OF FIGURES

1.1	S _N 2 reaction to form ethyl chloride from ethyl bromide.	2
1.2	Synthetic scheme of the traditional solid-state reaction to form the low-temperature iron-selenide phase. [2]	3
1.3	Solvothermal reaction set up scheme adapted from Yang <i>et al.</i> . [3]	5
1.4	Photos taken every 0.04 s during the metathesis reaction between NbCl ₅ and Li ₃ N. Figure from Meyer. [4]	6
2.1	(a) PXRD of the products of the iron selenide reactions completed with triphenylphosphine. A Rietveld refinement modeling 99% β-FeSe and 1% Fe (starred peak) is shown in red with the difference curve in blue. The structure of β-FeSe with iron (blue) and selenium (gold) is shown to the right. (b) Temperature versus 4πχ of iron selenide prepared using a triphenylphosphine flux measured with the MPMS.	16
2.2	PXRD of the products of the iron selenide reactions completed with (a) no flux, (b) eicosane, and (c) triphenylamine. The peaks barely visible above the background (marked by an asterix) are from residual PPh ₃ . Rietveld refinement modeling β-FeSe for each diffraction pattern is shown in orange and the fit for the remaining phases is shown in blue.	17
2.3	Diffraction patterns of a 2Fe + 2Se + PPh ₃ reaction collected <i>in situ</i> upon heating with each temperature offset for clarity in 25 °C increments. The most intense peak for each phase is labeled; note the logarithmic intensity axis.	18
2.4	PDF analysis of total scattering data collected <i>in situ</i> from the reactions of (a) iron and selenium in a triphenylphosphine flux and (b) selenium and triphenylphosphine upon heating. Data shown in black and fits shown in color gradient from blue to red upon heating.	18
2.5	(a) Ternary phase map between iron, selenium, and triphenylphosphine. The binary iron selenide phase diagram is shown above. The dots on the ternary phase map represent completed reactions; the red dot is the optimized reaction. (b) Formation energies (T = 0 K, DFT) [1] of computed and stable Fe-Se species that form the convex hull without triphenylphosphine (black line) in contrast to the offset line showing the extrapolated effective chemical potential of selenium (as to avoid FeSe ₂ formation) in the presence of excess triphenylphosphine (red line).	21
2.6	³¹ P NMR spectrum of the triphenylphosphine flux from the iron selenide reaction completed at 325 °C for 24 h with a 30 h cool.	22
3.1	Example phase diagram of tin sulfide containing just the most stable phases showing the minimum and maximum possible change in chalcogen chemical potential for a single phase to remain on the hull.	28
3.2	Computed formation energies (T=0 K, DFT) of compounds in the iron-sulfur system illustrating the convex hull (black line). [1] The offset red line approximates the convex hull with the addition of triphenylphosphine which lowers the effective chemical potential of sulfur.	29

3.3	Chemical potential range where each given phase is the only phase on the convex hull. Black dashed lines represents the proposed chemical potential change of each adduct.	33
3.4	Plots of each feature graphed versus the minimum change in chemical potential analyzed using SVM. The accuracy is written in the bottom right corner of each graph.	36
3.5	(a) Visualization of the dimensionally reduced data set (from 19 to 2 dimensions) plotted along the 2 principal component axis determined from PCA. The individual points are color coded by their classification of hypothesis supported: Yes/No. (b) Relative feature contributions to the two principle components used to plot the data in (a).	37
3.6	How well each feature separates reactions that follow the thermodynamic hypothesis from those that do not based on the random forest algorithm.	38
4.1	Picture of the completed reaction in sealed tube (left) with the blue material on the top of cobalt selenide powder. The product after solidifying and being ground (middle) and the crystals scraped from the side of the tube (right).	42
4.2	Picture of the crystals formed after slow-evaporation of Benzene.	43
4.3	Complete MALDI-MS spectrum of the blue material (top) and zoomed in section of the spectrum (bottom) labelled with the hypothesized cluster size and peak differences corresponding to loss of selenium and loss of cobalt.	46
4.4	PXRD of the blue material	47
4.5	PDF analysis of the blue material fit with CoSe (red line) with the difference curve in blue.	48
4.6	Diffraction pattern of the products from the attempted recrystallization reaction at 500 °C. Rietveld refinement (red line) includes the materials listed in the upper right with their weight percents. Inset shows the tube when it was removed from the furnace.	48
4.7	Diffraction pattern of the products from the attempted recrystallization reaction at 400 °C. Tick marks show the peaks for the phases listed in the top right.	48
4.8	Full FTIR spectra (left) and spectra zoomed in on the lower wavenumber peaks (right) of triphenylphosphine (orange) and the blue material (blue).	49
4.9	Magnetic susceptibility (left) and inverse magnetic susceptibility (right) versus temperature of the blue material.	50
4.10	Kubelka Monk function converting the reflectance data into absorbance of the blue material from diffuse reflectance data.	50
4.11	Sealed ampoule containing the cobalt-triphenylphosphine reactions (left) and the blue material from this reaction after being removed from the ampoule (right).	51
4.12	Structure of the $\text{Co}_{12}\text{Se}_{16}(\text{PEt}_3)_{10}$ cluster with blue being cobalt, green being selenium, orange being phosphorous, and grey being carbon. Hydrogens omitted for clarity. Figure from Champsaur <i>et al.</i> . [5]	52
4.13	PDF analysis of the blue material compared with a calculation of the $\text{Co}_{12}\text{Se}_{16}(\text{PEt}_3)_{10}$ cluster (red line) with the difference curve in blue.	53
4.14	Section of the FTIR spectra of triphenylphosphine (orange) and the blue material (grey). Arrows show the mass-dependant peak shift	54
4.15	Structure (top) and absorbance spectrum (bottom) of the selenium radical complex. Figures from Zhang <i>et al.</i> . [6]	56

5.1	PXRD of the products of the iron selenide reactions completed with triphenylphosphine (left) and boric acid (right). Rietveld refinements are shown in red with tick marks below indicating the peak locations for each phase. The phases used for the refinement are in the upper right with mole percents. The difference curve is below each graph in blue.	60
5.2	Formation energies (T = 0 K, DFT) [1] of computed and stable Fe–Se species that form the convex hull without triphenylphosphine (black line). Extrapolated effective chemical potential of selenium in the presence of excess triphenylphosphine (red) and boric acid (blue).	61
6.1	Formation energies (T = 0 K, DFT) [1] of computed and stable Cu–S species that form the convex hull.	64
A.1	Diffraction pattern of products from the reaction between PPh ₃ Se and Fe. Rietveld analysis is shown in red and difference curve in blue. The tick marks indicate peak locations for β-FeSe (grey), α-FeSe (green), and Fe (pink) and the phase fraction (mol%) is shown in the upper righthand corner.	76
A.2	Phase fraction (mol%) of each phase determined from Rietveld analysis of PXRD data collected <i>in situ</i> during the iron selenide reaction.	76
A.3	<i>Ex situ</i> PDF analysis of of 8Fe + Se + PPh ₃ reaction product. The phase fractions (mol%) of the refined phases are included in the top right corner. The data are shown as black circles, the fit is the red line, and the difference is the blue line.	78
A.4	<i>Ex situ</i> PDF analysis of the iron starting material. The phase fractions (mol%) of the refined phases are included in the top left corner. The data are shown as black circles, the fit is the red line, and the difference is the blue line.	78

Chapter 1

Introduction

1.1 Challenges of low-temperature solid-state synthesis

Solid materials are the backbone of our society making up computers, cars, and many modern technologies. Since the beginning of civilization, solid materials have played a key role in shaping our technologies. Solid-state materials have been so crucial to our evolution as a species that we have named ages of history after our abilities to make new solid-state materials. For example, the stone age became the bronze age with the knowledge of alloying copper with tin, arsenic, or other metals enabling widespread use of bronze. The transitions from stone age to bronze age and bronze age to iron age were only possible due to our abilities to make each new material. Now, in the age of silicon, we are still striving for the next solid-state material to revolutionize modern technologies such as batteries and hard drives. To improve on these technologies, new solid-state materials are necessary. To discover these new materials, new synthetic techniques will be necessary. The limited number of techniques available in solid-state synthesis makes synthesis by design (and therefore materials discovery) more difficult.

1.1.1 Techniques for solid-state synthesis are limited

Despite the importance and widespread use of solid-state materials, how to make them is not as well understood as one would think. This is especially clear when comparing synthesis in solid-state chemistry to organic chemistry. In organic chemistry, the guiding principles of reactivity and how to direct product formation are more generally understood. There is a large library of well-known, commonly used, named reactions that can be drawn from and strung together to target specific materials. [7] Organic reactions can be highly selective and tuning selectivity to achieve a desired outcome is more well understood. This allows for rational design of syntheses. For example, S_N2 reactions are one of the most commonly used reactions in organic chemistry, and

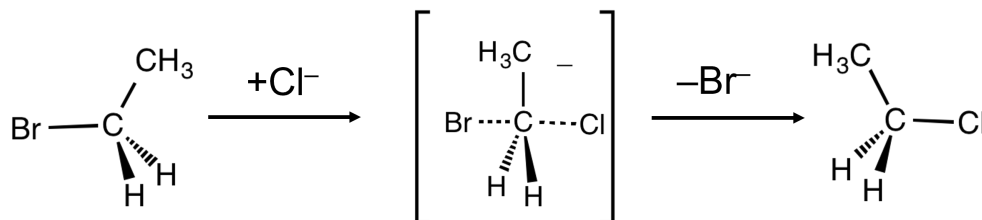


Figure 1.1: S_N2 reaction to form ethyl chloride from ethyl bromide.

they provide stereospecificity (Figure 1.1). With an S_N2 reaction, the leaving group bond breaks as the bond to the nucleophile forms. Since this occurs simultaneously, the reaction is selective for a product with a specific stereochemistry. Using tools such as S_N2 reactions allows organic chemists to direct product formation whereas in solid-state chemistry, selectively forming a desired product can be more difficult as these guiding principals behind reactions are less well understood. There are fewer reaction schemes to use when designing a synthesis and this often limits the materials able to be made. This is particularly true for materials that have limited stability, such as materials that are only stable at lower temperatures.

1.1.2 Challenges accessing low-temperature phases

Many materials in solid-state chemistry are only stable at lower temperatures, and therefore more challenging to make. Solid-state synthesis traditionally forms thermodynamically stable phases due to the high temperatures necessary for reactivity. These high temperatures form thermodynamically stable phases as they provide enough thermal energy for materials to find the energetic minimal configuration. Achieving kinetic control to target non-thermodynamically stable phases, such as low-temperature phases, can be difficult in the solid state. [8] A balance must be found between overcoming solid-state diffusion to promote reactivity, which is traditionally done using heat, while also stabilizing low-temperature phases. Therefore, making low-temperature phases using traditional solid-state synthesis often requires multi-step reactions with complex heating schedules.

For example, the formation of the low-temperature phase of iron selenide using traditional solid-state techniques is relatively difficult (Figure 1.2). [2] The low-temperature iron selenide

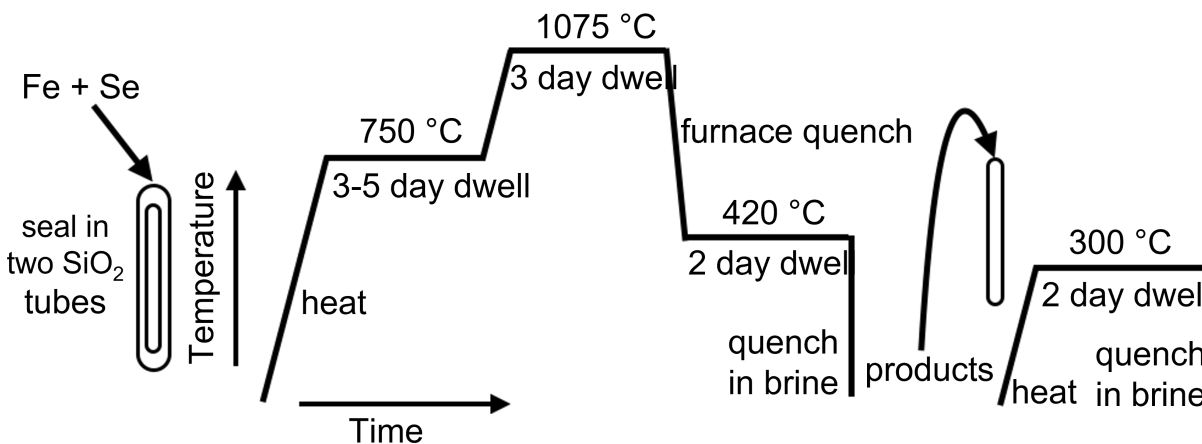


Figure 1.2: Synthetic scheme of the traditional solid-state reaction to form the low-temperature iron-selenide phase. [2]

phase, β -FeSe, converts to the high temperature phase, α -FeSe, at 457 °C; however iron and selenium together do not melt until 1075 °C. Therefore, a multi-step heating process is necessary to first achieve a melt to react iron and selenium and then convert the product to the low-temperature phase. To set up the reaction, iron and selenium must be sealed in two ampoules to contain the reaction in case the inner ampoule breaks. This double ampoule set up is then heated at 750 °C for 3-5 days to provide time for the selenium to partially react and reduce the risk of bursting the ampoules. The temperature is then increased to 1075 °C for 3 days to allow the iron and selenium to melt and react. The reaction is then moved into a different furnace set at 420 °C for 2 days. The quick temperature change is necessary to keep the material molten while reducing the temperature to the point where the low-temperature phase is stable. If the material is allowed to cool to that temperature over time, it will stabilize as the thermodynamically-stable, high-temperature phase (α -FeSe). The ampoules are then quickly cooled to prevent the formation of undesired phases, and the product is transferred to another ampoule. This second ampoule is heated to 300 °C for 2 days to improve the crystallinity of the product. Overall, this reaction takes 10-12 days, 3 ampoules and a furnace capable of high temperatures. This reaction is only one example demonstrating the difficulty accessing low-temperature phases in solid-state synthesis.

There are numerous other materials with similarly challenging syntheses. For example, both GaTe and SnS require multiple heating cycles at high temperatures. [9] Syntheses of these materials are designed to provide enough heat to encourage reactivity and still stabilize the low-temperature phase through the following steps. These processes are time-consuming and cannot be used to access all materials as some materials are unable to be stabilized using traditional solid-state reactions, even with the complex heating schemes. To simplify the process of making these materials and expand the number of materials able to be made, the search for new low-temperature synthetic techniques is ongoing. [8]

1.2 Techniques for low-temperature materials synthesis

There are a number of non-traditional techniques currently used in solid-state synthesis. The main non-traditional techniques used to target low-temperature solid-state phases are solvothermal reactions, metathesis reactions, and flux reactions. Solvothermal reactions involve heating a reaction in a solvent often above the melting point of the solvent (Figure 1.3). [3] In solvothermal reactions, the use of a solvent replaces the need to fully melt your reactants to promote reactivity as is done in traditional reactions. The use of heated solvent can aid the solubility of solids, which helps overcome solid-state diffusion to enable reactivity at lower temperatures. For example, powdered iron selenide can be made solvothermally using ethylene glycol and ammonium chloride as solvents. [10] This reaction requires placing all the starting materials in an autoclave and heating to 200 °C for 5-10 days, which is much simpler than the traditional reaction shown in Figure 1.2. The solvents in this reaction were chosen to optimize their coordinating ability for iron and selenium. Reactions using just ethylene glycol had remaining starting materials indicating the solvent was not completely dissolving the reactants. The introduction of ammonium chloride allowed for complete solvation of reactants and the ratio of iron and selenium starting materials is then varied to purify the product. Solvothermal reactions are a useful tool; however, as they require an appropriate solvent for the desired system, they are not applicable for all reactions.

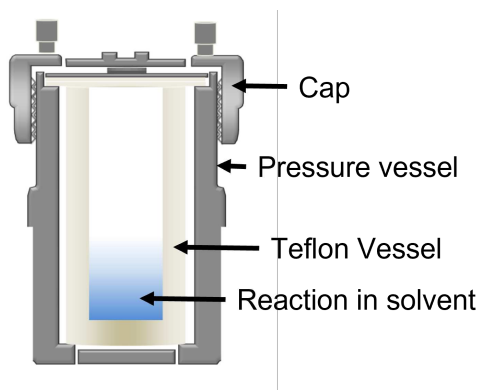


Figure 1.3: Solvothermal reaction set up scheme adapted from Yang *et al.*. [3]

Metathesis reactions are another synthetic tool for solid-state materials. Metathesis reactions are double exchange reactions that use the formation of a highly stable salt side-product to drive the reaction to completion. [4] For example, Li_7NbN_4 can be synthesized through a reaction between NbCl_5 and Li_3N . In this case, the formation of the LiCl side product drives the reaction and since this is a self propagating reaction, it only requires an initial ignition to complete. Once this reaction is ignited with a hot plate, it will go to completion. These reactions often occur quickly and exothermically as seen in Figure 1.4. Therefore, metathesis reactions can be difficult to control and finding appropriate starting materials to produce both the desired phase and a stable salt can be challenging.

Both solvothermal and metathesis reactions are useful techniques in solid-state synthesis; however, the library of known syntheses is still very limited. Finding more synthetic techniques that can access a wide variety of phase would be valuable in simplifying known syntheses and enabling materials discovery. Flux reactions are another technique used to promote reactivity at lower temperatures. As the focus of this thesis, flux reactions are discussed in more detail below.

1.2.1 Flux-based low-temperature materials synthesis

Similar to solvothermal reactions, fluxes promote reactivity at lower temperatures by providing a solvent that helps overcome solid-state diffusion. Instead of this solvent being a liquid at room temperature as is used in solvothermal reactions, a flux is solid at room temperature, but molten at

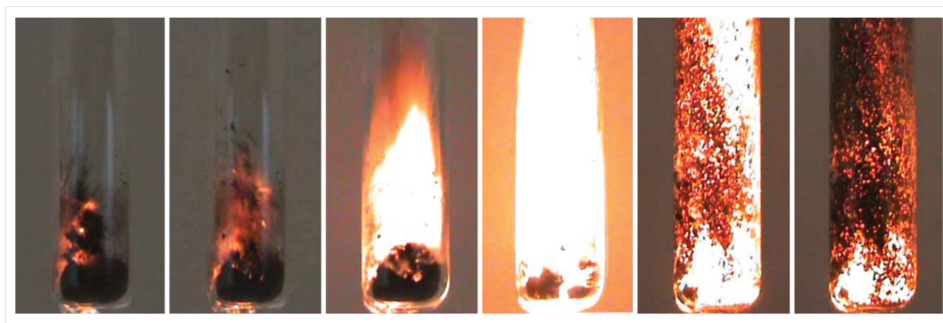


Figure 1.4: Photos taken every 0.04 s during the metathesis reaction between NbCl_5 and Li_3N . Figure from Meyer. [4]

the reaction temperature. Fluxes can either provide only a molten medium to encourage mixing, or they can also be reactive. Additionally, since fluxes often melt at a lower temperature than would be otherwise required for the reaction, flux reactions can occur at a lower temperature than traditional solid-state syntheses and can be used to target low-temperature phases. The low-temperature phase of iron selenide can also be made using a flux reaction where the flux only provides a molten medium. [11] In this case, a molar excess of KCl is mixed with iron and selenium and heated. Since KCl melts at $770\text{ }^\circ\text{C}$ and acts as a solvent, the reaction only needs to be heated to a maximum temperature of $850\text{ }^\circ\text{C}$ and takes 4 days. Again, this is much simpler than the traditional iron selenide reaction scheme shown in Figure 1.2. Reactive fluxes are also often used to make solid-state materials, such as in the reaction to form VSn_2 from vanadium and tin. [12] For this reaction, an excess of tin acts as a self-flux where it is both a solvent and a reactant that becomes part of the product. In this way, the barrier of solid-state diffusion can be overcome while also providing a reactant. In both of these cases, the use of a flux enables a lower reaction temperature which can stabilize low-temperature phases easier than traditional solid-state synthesis.

Generally fluxes consist of metallic melts, metal chlorides, or alkali chalcogenides as the molten phase. [8, 13] Since the fluxes act as solvents, difficulties with solubility, similar to those with solvothermal reactions, can occur. As you need a solvent that will coordinate the reactants, finding a flux that is appropriate for a given system can be challenging. Therefore, new fluxes are essential for progressing solid-state flux synthesis. Additionally, the temperature of these reactions

is often dictated by the temperature at which the flux melts. So to target materials that are only stable at low temperatures, fluxes that are molten at lower temperatures, coordinate the reactants, and are easy to separate from the products are necessary.

This thesis will focus on organic fluxes as a tool for low-temperature solid-state synthesis. Organic materials have been used in solid-state synthesis as solvents, reactants, and selectivity agents. Previously, triphenylphosphine was used to promote reactivity in a metathesis reaction between CuCl_2 and Na_2Se_2 to form a metastable phase of CuSe_2 . [14] In this synthesis, the triphenylphosphine lowers the activation barrier for the reaction, allowing for the selective formation of the metastable phase before it can convert to the more stable polymorph. The success of triphenylphosphine-mediated metathesis reactions suggests the potential for organic flux reactions.

1.3 Organic flux synthesis

This work represents the first example, to our knowledge, of an organic flux synthesis. Organic fluxes use organic materials as the molten material to enable reactivity. Since organic materials are made of molecules that can be carefully tuned to control the chemistry, these reactions can be used to selectively target low temperature phases. This work explores the idea of using organic compounds that act as reactive fluxes. Rather than the tin self-flux example provided above, these organic fluxes do not generally become a part of the primary product. The organic fluxes interact with the reactants, forming an intermediate that enables selective product formation. Excess of this intermediate may remain as a side product; however, the organic flux generally does not incorporate into the main product. This thesis discusses how triphenylphosphine flux reactions are selective, the guiding principles behind whether or not a given reaction is successful, a new material discovered through a triphenylphosphine flux reaction, and the prospect of controlling reactivity through changing the flux.

In the second chapter, the idea of an organic flux is introduced through a case study of using triphenylphosphine to make the low-temperature phase of iron selenide. [15] As described above, this phase is traditionally synthesized through a multi-step, 10 day reaction that requires a special-

ized furnace capable of reaching over 1000 °C. Using triphenylphosphine simplifies the reaction to a single-step, low-temperature, 5-day reaction. Triphenylphosphine was found to react with selenium, changing the reactivity of the selenium, and enabling selective reactivity between the iron and the triphenylphosphine selenide to form iron selenide at a low temperature. This provides a proof of concept that triphenylphosphine flux reactions can be used for selective low-temperature synthesis in the solid state.

The third chapter further explores the use of a triphenylphosphine flux, expanding it to the synthesis of other metal chalcogenides and explaining the guiding principals behind reactivity. Triphenylphosphine flux reactions were shown to enable selective reactivity in a number of different binary metal chalcogenide systems. A combination of thermodynamic properties and properties such as metal density as proxies for kinetic behavior are demonstrated to be predictors for how a given system will react. This provides more knowledge on how triphenylphosphine flux reactions can be used in the future for targeted synthesis.

The fourth chapter discusses a new cobalt-selenium-triphenylphosphine material that was synthesized using a triphenylphosphine flux, demonstrating the potential of organic fluxes for materials discovery. The data presented support the identification of the material to be a cluster of approximately $\text{Co}_{12}\text{Se}_{16}(\text{PPh}_3)_{10}$ size. Alternate hypotheses for the identification of this material are also discussed as a smoking gun for phase assignment is lacking. Regardless, it is clear that this material is a new cobalt-selenium-triphenylphosphine compound, which shows the ability of organic fluxes to discover new solid-state materials.

In the fifth chapter, preliminary results exploring another organic flux are discussed. The impact of using a flux that is a Lewis acid instead of a Lewis base was explored through the use of boric acid. Boric acid selectively forms FeSe_2 demonstrating how changing the flux can change which product is targeted. This demonstrates the potential for tunable solid-state synthesis.

The concluding chapter discusses the future prospects of this work including exploring other organic fluxes and targeting different materials. Future work focused on gaining an understanding

of how to use organic fluxes for selective synthesis is proposed. Additionally, the expansion of organic flux synthesis to ternary materials or other clusters is discussed.

Appendices include the supplemental information for chapters 2 and 3, the code for the analysis discussed in chapter 3, an overview of my contributions to publications where I was a second author, a list of abbreviations used throughout this thesis, a jargon-free overview of my research, and a selection of my favorite photos I have taken during graduate school.

Chapter 2

Low-temperature synthesis of superconducting iron selenide using a triphenylphosphine flux¹

2.1 Overview

Many functional materials have relatively low decomposition temperatures ($T \leq 400$ °C), which makes their synthesis challenging using conventional high-temperature solid-state chemistry. Therefore, non-conventional techniques such as metathesis, hydrothermal, and solution chemistry are often employed to access low-temperature phases; the discovery of new chemistries is needed to expand access to these phases. This contribution discusses the use of triphenylphosphine (PPh_3) as a molten flux to synthesize superconducting iron selenide ($\text{Fe}_{1+\delta}\text{Se}$) at low temperature ($T = 325$ °C). Powder X-ray diffraction and magnetism measurements confirm the successful formation of superconducting iron selenide while nuclear magnetic resonance spectroscopy and in situ X-ray diffraction show that the formation of superconducting FeSe at low temperatures is enabled by an adduct between the triphenylphosphine and selenium. Exploration of the Fe-Se- PPh_3 phase space indicate that the PPh_3 -Se adduct effectively reduces the chemical potential of the selenium at high concentrations of triphenylphosphine. This contribution demonstrates that the use of a poorly-solvating yet reactive flux has the potential to enable the synthesis of new low temperature phases of solid materials.

¹This chapter is a published paper with M. Jewels Fallon as primary experimenter and author (Fallon; Martinolich; Maughan; Gallington; Neilson. Dalton Trans. 2019, 48, 16298-16303). Preliminary experiments were completed by Andrew J. Martinolich, experiments at Argonne National Laboratory were completed with the help of Annalise E. Maughan and Leighanne C. Gallington. James R. Neilson provided valuable guidance with experiments, data analysis, and editing. This work was supported by the National Science Foundation (DMR-1653863). JRN acknowledges partial support from a Sloan Research Fellowship and a Cottrell Scholar Award. This research used resources of the Advanced Photon Source, a U.S. Department of Energy (DOE) Office of Science User Facility operated for the DOE Office of Science by Argonne National Laboratory under Contract No. DE-AC02-06CH11357.

2.2 Introduction

Many important functional inorganic materials are only stable, or are only able to be synthesized, below temperatures that are typically required for traditional reactions. [8] Phases which are only stable below $T \sim 400$ °C are often challenging to synthesize and require complex or non-traditional synthetic methodologies that may limit potential applications. For example, many metal chalcogenides are only accessible with more challenging techniques such as high pressure or multiple complex regrinding and reheating schedules. [2, 16] The discovery of new synthetic methods to access materials phases with stability only at low temperatures is therefore paramount for advancing materials discovery and will enable more widespread use of materials that are otherwise challenging to synthesize. [8]

Flux synthesis is a synthetic technique in which a compound that is molten at the reaction temperature is used to promote diffusion and enable reactivity between solid phases at lower temperatures. Traditionally, flux synthesis involves metallic melts (Sn, Bi), metal chlorides (LiCl, KCl), or alkali chalcogenides (Na_xS_y) as the molten phases. [8, 13] For example, the eutectic mixture of NaCl and KCl has been used to grow single crystals of FeSe at $T = 850$ °C. [17] This compliments solvothermal synthesis, in which solvents are heated past their normal boiling points by heating in a closed vessel designed to hold elevated pressures. A solvothermal approach using ammonium chloride and ethane-1,2-diol has been used to prepare FeSe powders from elemental precursors at $T = 200$ °C relative to the salt flux or reaction from the elements. [10] These methods are all used to promote reactivity by aiding in mass transport at relatively low temperatures.

In this contribution, we illustrate the use of a hybrid approach: an organic flux that enables the reaction between iron and selenium at low temperatures. These molecules have long been used to control the size and morphology in the synthesis of nanocrystals. [18] Since the superconducting phase of iron selenide, β -FeSe, is only stable below 457 °C [19], its synthesis requires two heating cycles and an annealing cycle [2, 20] or a solvothermal synthesis as previously discussed. [10, 21] Due to the presence of competing phases (β -FeSe, α -FeSe, Fe_7Se_8) β -FeSe provides a good system for use as a case study to investigate alternative synthetic techniques. We previously demon-

strated the role of triphenylphosphine in promoting reactivity between CuCl_2 and Na_2Se_2 to form a metastable polymorph CuSe_2 in a metathesis reaction. [14] Triphenylphosphine also has a reasonable range at which it is molten and stable making it suitable for reactions at elevated temperatures suitable for producing extended solids ($T_m = 80\text{ }^\circ\text{C}$, $T_{decomp} > 400\text{ }^\circ\text{C}$). The formation of $\beta\text{-FeSe}$ is confirmed by powder X-ray diffraction (PXRD) and magnetism measurements. Control reactions without a flux and with non-Lewis basic fluxes demonstrate the necessity of a molten and reactive flux. Nuclear magnetic resonance (NMR) and *in situ* X-ray diffraction (XRD) and pair distribution function (PDF) analysis suggest that the formation of an adduct between the selenium and triphenylphosphine promotes mass transport between the iron and the selenium while also serving to decrease the chemical potential of selenium. Overall, this research shows that triphenylphosphine fluxes can enable the synthesis of low-temperature phases of solid-state materials and may aid in the discovery of new functional materials.

2.3 Experimental

Purified iron powder (NOAH Technologies Corporation, 99.9%), selenium shot (Alfa Aesar, 99.999%) or powder (Sigma Aldrich, 99.5%), and triphenylphosphine flakes (Alfa Aesar, 99+%) in a 1:1:1.5 mole ratio were sealed in a fused SiO_2 ampoule (10 mm ID/12 mm OD) under vacuum ($p \leq 10\text{ mTorr}$). The ampoule was heated at a rate of $10\text{ }^\circ\text{C}/\text{min}$ to $325\text{ }^\circ\text{C}$ and dwelled for 117 h in a muffle furnace before quenching in water. Iron powder was purified of surface oxides by sealing it in a fused SiO_2 ampoule under vacuum ($p \leq 10\text{ mTorr}$). The ampoule was heated at a rate of $10\text{ }^\circ\text{C}/\text{min}$ to $980\text{ }^\circ\text{C}$ and dwelled for 16 h before cooling in the furnace. The iron was transferred to a new evacuated ampoule and the heating cycle was repeated until the iron appeared shiny. Diffraction analysis with an internal standard reveals that the iron is $\sim 75\text{ wt}\%$ amorphous.

A series of exploratory reactions were completed by varying the reaction conditions as summarized in detail in the Supplemental Information[†]. For each reaction, purified iron powder, selenium shot, and triphenylphosphine flakes in the desired stoichiometric quantities were sealed under vacuum in a SiO_2 ampoule. The sealed ampoule was heated in a furnace at a ramp rate of $10\text{ }^\circ\text{C}/\text{min}$

up to the final temperature for the desired reaction time. The "air-cooled" reactions were removed from the furnace and left at room temperature; quenched reactions were taken from the furnace and placed directly into a water bath. The reactions above 350 °C were sealed in 4 mm ID, 6 mm OD ampoules and were placed in metal piping (open both ends) to contain reactions in the event of gas formation (no ampoules failed). Several control reactions were completed: without flux, with eicosane (Acros Organics, 99%), and with triphenylamine (TCI America, 98%). Once the reactions were completed, the organic materials were mechanically removed with a steel spatula from each reaction and set aside for additional analysis. The remaining material was washed in ~10 mL benzene (EMD Millipore, 99%) per 500 mg FeSe and stirred until the residual flux dissolved. Samples for magnetic characterization were kept air-free once the reaction had completed. For these samples, the ampoules were opened in an argon-filled glove box and rinsed with degassed, dry benzene (deoxygenated over CaH₂ and distilled) in the glovebox. For all samples, once the triphenylphosphine dissolved, the samples were ground with a mortar and pestle for 2-3 min until homogenous.

Laboratory powder X-ray diffraction data were collected on a Bruker D8 Discover diffractometer with CuK α radiation and a Lynxeye XE-T position-sensitive detector. Samples were prepared on a zero-diffraction Si wafer. *Ex situ* total X-ray scattering data sets for pair distribution function (PDF) analysis were collected on a Panalytical Empyrean Diffractometer with the GaliPIX 2D detector using AgK α radiation. Samples were packed in 0.0395 in outer diameter kapton capillaries sealed with modeling clay.

The samples for *in situ* analysis were prepared for analysis by ball milling iron, selenium, and triphenylphosphine in a 1:1:0.5 mole ratio at T = 77 K using a Retsch cryomill. The samples were milled in a stainless steel jar with stainless steel ball bearings at 30 Hz for 15 min after cooling. Milling was performed to provide an intimate mixture and to facilitate capillary packing. The mixture was then packed in a 1.1 mm borosilicate capillary in air and immobilized with quartz wool and measured in a flow cell furnace [22] using the 11-ID-B beamline at the Advanced Photon Source at Argonne National Laboratory. Surface tension of the melt kept the contents within the

capillary. No apparent oxidation products were observed over the course of the reaction. The reaction was heated up at 10 °C/min to 325 °C taking diffraction patterns every 25 °C from a distance of 1 m for XRD and 200 mm for PDF. A CeO₂ standard was also measured for sample-detector distance calibration. The wavelength was 0.2113 Å, a Q_{min} of 0.5 Å⁻¹ and a Q_{max} of 5.95 Å⁻¹ for XRD or a Q_{max} of 23 Å⁻¹ for PDF was used during data transformation. GSAS-II was used to transform the raw data to PDF and PDFgui was used to analyze the data. [23, 24]

A variety of compositions were picked throughout the phase space and are discussed specifically in the results. All of these reactions were completed following the heating schedule of heating at 10 °C/min up to 325 °C, dwelling for 72 h and slow-cooling for 45 h. After the reactions were completed, organic residue was mechanically separated for NMR spectroscopy experiments. The remaining product powder was ground and analyzed through PXRD. *Ex situ* PDF analysis as described above was completed on the product from the reaction 8Fe + Se + PPh₃ as well as the purified iron powder. This reaction was chosen for analysis due to the lack of iron in the products as observed by PXRD Rietveld refinement.

Magnetism measurements were completed with the Quantum Design Inc. Magnetic Properties Measurement System (MPMS-XL). Samples were prepared for the MPMS in the glovebox by weighing approximately 25 mg of the product into a gelatin capsule. Kapton was wrapped around the sample to keep it air-free. Upon removal from the glovebox, the sample was placed in a straw and loaded in the MPMS. The zero field-cooled magnetization was measured from 1.9 K to 20 K at a field strength of $H = 5$ Oe. The magnetization was converted to volume susceptibility using field strength, mass, and theoretical density of $\rho = 5.68$ g/cm³. [2]

Room temperature ¹H and ³¹P NMR spectra were taken of the white organic residue of several reactions. Samples were prepared for NMR by placing approximately 10 mg of the nominal triphenylphosphine residue into an NMR tube and adding 700 μL of deuterated benzene (Cambridge Isotope Laboratory Inc., 99.5%). Samples were placed in an Agilent (Varian) 400 MHz NMR. Control room temperature ¹H and ³¹P NMR spectra were also taken separately of the deuterated

benzene solvent and a sample of the unreacted triphenylphosphine flakes prepared in the same way as the post-reaction specimens.

2.4 Results and Discussion

Superconducting iron selenide forms with a 1 Fe to 1 Se ratio in a 1.5 molar excess of triphenylphosphine flux at 325 °C after 117 h. PXRD confirms the crystalline purity with only 1 mole percent Fe detected (Figure 2.1a). Based on the onset of volume exclusion of a magnetic field, the superconducting transition temperature is around $T_c = 8.9$ K (Figure 2.1b), and is a gradual transition (in contrast to the sharp $T_c = 8.5$ K transition observed in the literature [2]). The T_c is extremely sensitive to the stoichiometry, $\text{Fe}_{1+\delta}\text{Se}$, with deviations from $\text{Fe}_{1.01}\text{Se}$ causing a decrease in the transition temperature. [2, 20] The positive shift in the $4\pi\chi$ of the iron selenide synthesized using a triphenylphosphine flux compared to the $4\pi\chi$ reported in literature can be attributed to the slight iron excess in the sample. Based on the observed diamagnetic transition, the superconducting volume fraction is around 70% (Figure 2.1b), which was reproducible across multiple samples. The β -FeSe maintains the structure and properties as iron selenide synthesized without significant oxygen contamination or stoichiometric deviation.

To explore how triphenylphosphine impacts the reaction to form β -FeSe, control reactions with different organic molecules (NPh_3 , $\text{C}_{20}\text{H}_{42}$) were completed. A summary of products from these control reactions is shown in Table S2. The reaction without a flux forms a mixture of Fe-Se phases along with Fe, consistent with a mass transport-limited reaction (Figure 2.2a; majority products: β -FeSe, Fe_3Se_4). Performing the reaction in molten eicosane wax ($\text{C}_{20}\text{H}_{42}$, a chemically unfunctionalized alkane) also forms a variety of products indicating that a molten and reactive flux is necessary for a complete reaction (Figure 2.2b; majority products: FeSe_2 , β -FeSe, Fe_3Se_4). Reaction in molten triphenylamine also forms a distribution of products (Figure 2.2c; majority products: Se, FeSe_2). This suggests the Lewis basicity is an important factor for forming the desired product. This is further supported by the successful reaction of Ph_3PSe with iron to form β -FeSe with 96 mol% purity (impurities: 3 mol% α -FeSe, and 1 mol% Fe), indicating that the

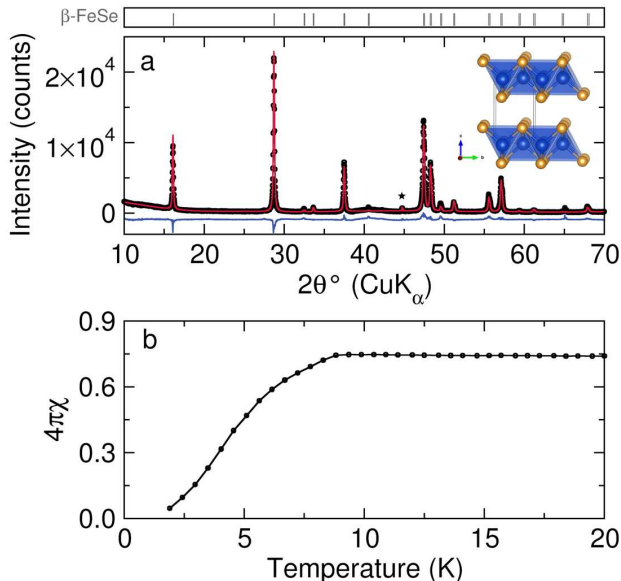


Figure 2.1: (a) PXRD of the products of the iron selenide reactions completed with triphenylphosphine. A Rietveld refinement modeling 99% β -FeSe and 1% Fe (starred peak) is shown in red with the difference curve in blue. The structure of β -FeSe with iron (blue) and selenium (gold) is shown to the right. (b) Temperature versus $4\pi\chi$ of iron selenide prepared using a triphenylphosphine flux measured with the MPMS.

adduct is the reactive species (Figure S1). Together, these controls demonstrate the necessity of a molten and partially reactive flux, where reactivity is dictated by Lewis basicity.

A number of test reactions completed at higher and lower temperatures as well as shorter dwell times yielded impure products. Higher temperatures caused the flux to decompose while reactions completed at lower temperatures showed a mixture of α -FeSe and β -FeSe. Shorter reactions as well as reactions with shorter cool times also contained a mixture of α -FeSe and β -FeSe. Thus it was determined that the length of time at higher temperature is important for complete reaction to β -FeSe.

To gain more insight into the nature of reactivity, *in situ* XRD and PDF experiments were completed on a mixture of iron, selenium, and triphenylphosphine (Figure 2.3). Phase fractions determined through Rietveld refinements are shown in Figure S2. Based on Rietveld analysis of these data where triphenylphosphine selenide formation is observed, triphenylphosphine selenide forms immediately once triphenylphosphine begins to melt around 75 °C. The reaction goes through a phase where everything but the iron is molten, and once a temperature of 275 °C is reached, iron

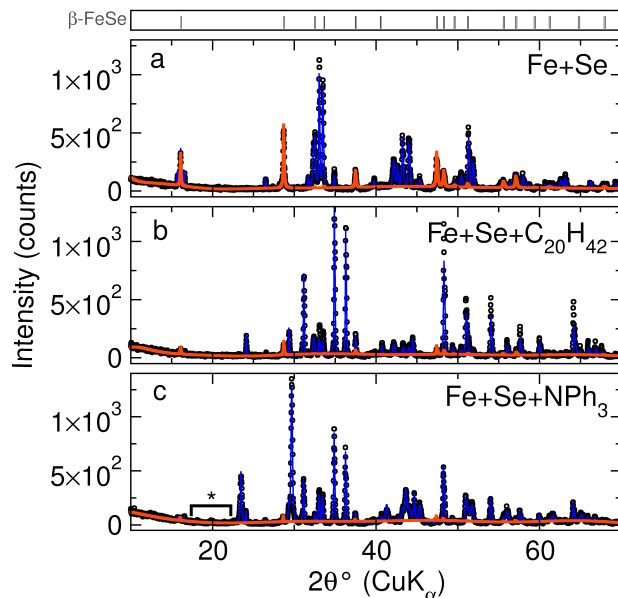


Figure 2.2: PXRD of the products of the iron selenide reactions completed with (a) no flux, (b) eicosane, and (c) triphenylamine. The peaks barely visible above the background (marked by an asterix) are from residual PPh_3 . Rietveld refinement modeling $\beta\text{-FeSe}$ for each diffraction pattern is shown in orange and the fit for the remaining phases is shown in blue.

selenide begins to form. Initially, $\alpha\text{-FeSe}$ and Fe_3Se_4 form and these phases disappear as $\beta\text{-FeSe}$ forms at higher temperatures. It has been suggested that less stable products often form first (e.g., Ostwald's step rule) which explains the formation of these iron selenide phases initially over the expected FeSe product. [25] At 325°C both $\alpha\text{-FeSe}$ and $\beta\text{-FeSe}$ are present indicating that $\beta\text{-FeSe}$ is stabilized through dwelling at the reaction temperature. Incomplete conversion to $\beta\text{-FeSe}$ is observed *in situ* since the reaction was not kept at temperature for an extended period of time. This supports the *ex situ* observation that a long reaction time (~ 117 h) is required for "complete reaction". *In situ* PDF of the reaction between iron, selenium, and triphenylphosphine as well as the reaction between triphenylphosphine and selenium (Figure 2.4) support what is observed in the *in situ* XRD with how the reaction progresses. Additionally the *in situ* PDF analysis shows no indication of large amounts of amorphous materials, as assessed from analysis of the stoichiometry. There is the possibility for small amounts of amorphous phases making up less than 2.5 mol% of the phases present. [26]

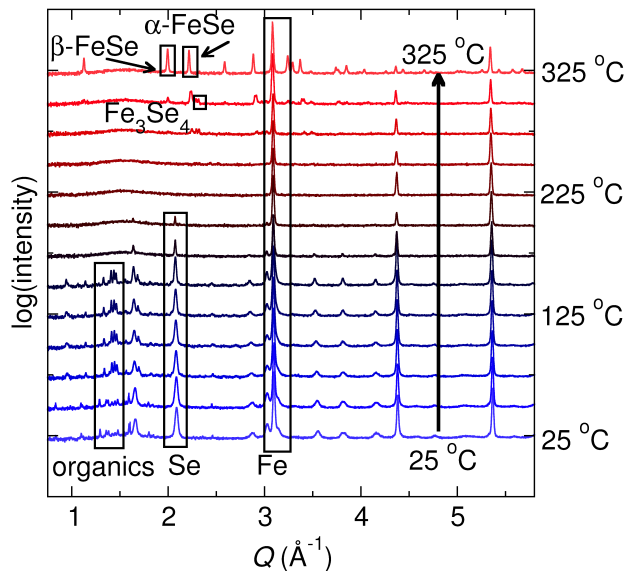


Figure 2.3: Diffraction patterns of a $2\text{Fe} + 2\text{Se} + \text{PPh}_3$ reaction collected *in situ* upon heating with each temperature offset for clarity in $25\text{ }^\circ\text{C}$ increments. The most intense peak for each phase is labeled; note the logarithmic intensity axis.

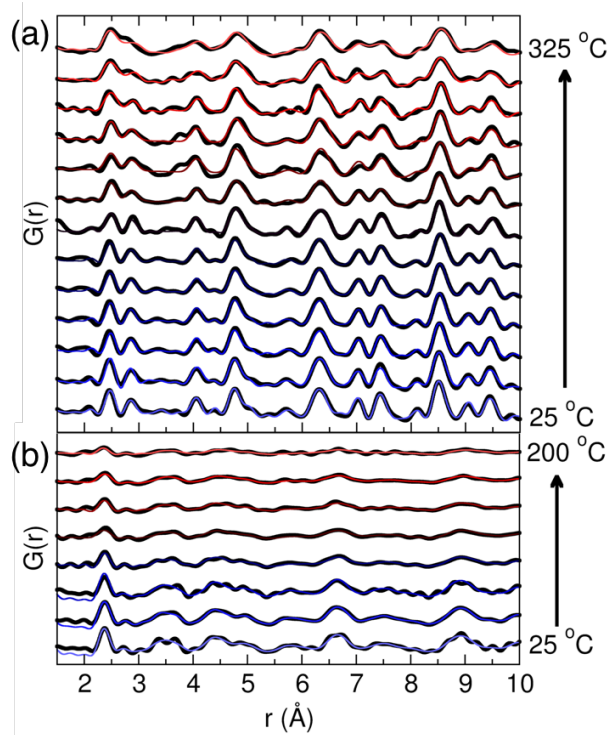


Figure 2.4: PDF analysis of total scattering data collected *in situ* from the reactions of (a) iron and selenium in a triphenylphosphine flux and (b) selenium and triphenylphosphine upon heating. Data shown in black and fits shown in color gradient from blue to red upon heating.

Exploring the ternary phase space demonstrated that the reaction does not follow an extension of the Fe-Se phase diagram. A map of the ternary phase space between iron, selenium and triphenylphosphine is shown in Figure 2.5a. β -FeSe exists as the predominate phase for ≤ 50 mol% Se while other phases are present depending on the ratio of the reactants (Table S2); selenium is the primary phase for ≥ 50 mol% Se. This indicates that reaction in a triphenylphosphine flux preferentially forms β -FeSe. The selenium-rich reactions yield more than three phases, suggesting that the phase map does not represent a true equilibrium, as based on Gibbs' phase rule. Based on the phase fractions calculated from Rietveld refinements in relation to the starting composition, the reaction products are deficient in crystalline iron. PDF analysis of the starting iron as well as a completed reaction indicate a significant fraction of diffraction amorphous iron (e.g. nanocrystalline) present in the precursor, which accounts for the iron missing from analysis of the diffraction data (Figures S3, S4). NMR spectroscopy performed on the post-reaction organic residue samples from these completed reactions reveal signals consistent with triphenylphosphine and triphenylphosphine selenide (Figure 2.6). [27] Reactions completed with excess selenium contained mostly triphenylphosphine selenide, while reactions completed with excess iron contained mostly triphenylphosphine.

The results of these reactions suggest that triphenylphosphine does not just provide a liquid medium for accelerated mass transport, but that triphenylphosphine also reduces the reactivity of selenium. It appears that in reactions containing more triphenylphosphine the product FeSe_2 is avoided, which suggests that the chemical potential of selenium is reduced. This is shown schematically in Figure 2.5b using calculated formation energies for the reportedly stable Fe-Se phases from the Materials Project (Table S3). [1] Extrapolation of the $T = 0$ K calculations suggests that the triphenylphosphine reduces the effective chemical potential by at least 0.5 eV/atom. Chemically this is rationalized by the stability of the dative bond in the Se-PPh_3 adduct, thus reducing the reactivity of the selenium towards iron. This notion of a partially reactive flux provides a handle for designing selective reactions.

Triphenylphosphine acts as a low-temperature, molten flux for materials synthesis as exemplified with β -FeSe. The optimized β -FeSe synthesis reacts the elements in a triphenylphosphine flux at 325 °C for 117 h. *In situ* analysis of the iron selenide reaction shows formation of a Se-PPh₃ adduct that reduces the chemical potential of Se in its reaction towards iron, while also forming a high mobility, liquid phase. This synthetic approach has the potential to improve the syntheses for many solid-state materials at lower temperatures and with chemical selectivity.

2.5 Conflicts of interest

There are no conflicts to declare

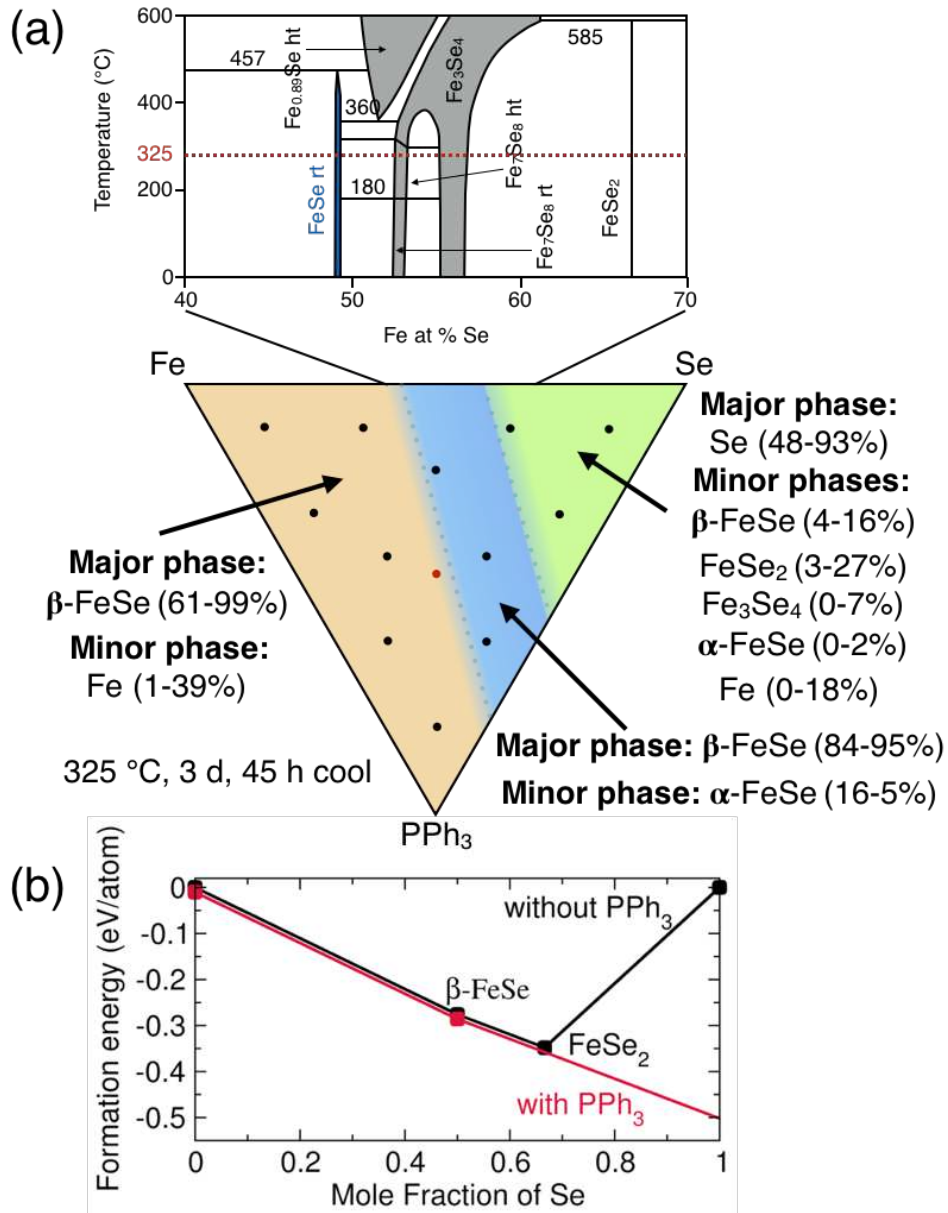


Figure 2.5: (a) Ternary phase map between iron, selenium, and triphenylphosphine. The binary iron selenide phase diagram is shown above. The dots on the ternary phase map represent completed reactions; the red dot is the optimized reaction. (b) Formation energies ($T = 0$ K, DFT) [1] of computed and stable Fe-Se species that form the convex hull without triphenylphosphine (black line) in contrast to the offset line showing the extrapolated effective chemical potential of selenium (as to avoid FeSe_2 formation) in the presence of excess triphenylphosphine (red line).

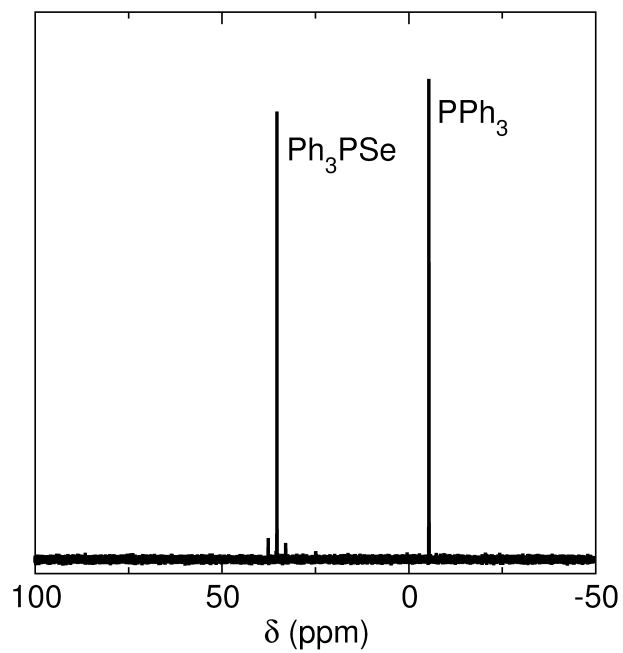


Figure 2.6: ^{31}P NMR spectrum of the triphenylphosphine flux from the iron selenide reaction completed at 325 °C for 24 h with a 30 h cool.

Chapter 3

The Reactivity of Triphenylphosphine fluxes in the Synthesis of Metal Chalcogenides²

3.1 Overview

Solid-state synthesis targeting materials that are only stable at low temperatures ($T \leq 600$ °C) can be difficult owing to slow solid-state diffusion at lower temperatures. Slow solid-state diffusion reduces mobility in the system which inhibits reactivity. There are a limited number of synthetic techniques to access materials that are only stable at low temperatures. Using a material, called a flux, that is molten at the reaction temperature to enable mobility is one technique used to overcome solid-state diffusion at reduced temperatures. In this paper, the utility of a triphenylphosphine flux in solid-state synthesis is explored. A series of reactions varying the metal and chalcogen were completed to gain a better understanding of the guiding thermodynamic and kinetic properties behind the reactivity. Various properties of the system that can be related to kinetic behavior, such as densities, electronegativities, and electron affinities, were analyzed to determine what has the largest impact on reactivity. A smaller subset of the most impactful properties were used to create a model that predicts the outcome of future reactions. This work shows that the triphenylphosphine flux reaction is broadly applicable and adds to our understanding of these reactions through exploring the kinetic and thermodynamic factors that impact reactivity.

²This chapter is a manuscript in preparation. M. Jewels Fallon completed all experiments and wrote the code and manuscript. Anthony K. Rappe completed bond dissociation energy calculations and James R. Neilson provided guidance with experiments, coding and editing. This work was supported by the National Science Foundation (DMR-1653863). The authors wish to thank the Analytical Resources Core (RRID: SCR_021758) at Colorado State University for PXRD instrument access.

3.2 Introduction

The synthesis and discovery of solid-state materials remains challenging. [8] Organic chemistry provides numerous well understood reactions schemes that can be used to target specific materials. S_N2 reactions, for example, provide stereospecificity and therefore can be used to synthesize materials of a specific composition. [7] In solid-state chemistry there are fewer well-understood and selective reactions that can be used to synthesize a desired material. Additionally, there is the barrier of solid-state diffusion that must be overcome for a reaction to progress, which often requires high temperatures. This introduces a different set of challenges, specifically in accessing the numerous phases that are only stable at lower temperatures ($T \leq 600$ °C). [8] Having a larger library of well-understood reaction techniques available to access these compounds would be helpful for solid-state synthesis.

One technique often used to synthesize phases that are only stable at lower temperatures is flux synthesis. [13] Flux synthesis involves the use of an element or compound that is molten at the reaction temperature to act as a solvent and aid solid-state diffusion. Flux synthesis is a powerful synthetic tool that has been used to make many solid-state compounds, but generally fluxes consist of metallic melts [12], metal chlorides [11], or alkali chalcogenides [28]. Recently, the idea of organic fluxes were introduced through the use of triphenylphosphine as a flux to make superconducting iron selenide at a low temperature. [15] That study introduced the idea of using organic fluxes to promote low temperature reactivity and enable more tunability in solid-state synthesis.

Here, we expand the scope of organic fluxes in solid-state synthesis, looking specifically at different binary metal chalcogenide systems to determine the guiding principles behind the reactivity of triphenylphosphine fluxes. Reactions involving sulfur, selenium, and tellurium as well as various transition metals and p-block metals reacted as predicted, demonstrating the broad applicability of this reaction. A thermodynamic hypothesis for predicting product formation is discussed. This hypothesis is based on the assumption that the adduct formation should change the chemical potential by the same amount in every reaction involving a given chalcogen. Thus, by comparing that approximated change in chemical potential to the phase diagrams of each reaction for a given

chalcogen, the product can be predicted. As this does not explain all the reactions, kinetic factors are also explored. Based on the thermodynamic hypothesis and most impactful kinetic factors, a model for predicting reactivity is created. In this contribution, we discuss the guiding principles behind reactivity, building off our previous work to gain a better understanding of how organic fluxes can be employed in solid-state synthesis.

3.3 Experimental

3.3.1 Synthesis

A list of the reactants, their source, and their purity is provided in the supplemental information. A list of all the reactions with the mole ratio of the completed reactants along with the dwell time and products is provided in Table 3.1. The reaction with iron and selenium was completed as previously described, and all reactions involving iron used iron powder that was purified as explained previously. [15] To summarize the purification process, the iron powder was heated to 980 °C for 16 hours in a fused SiO₂ ampoule sealed under vacuum. All metal chalcogenide reactions were set up in the same manner. The desired metal, chalcogen, and triphenylphosphine in the specified mole ratios were sealed in a fused SiO₂ ampoule (10 mm inner diameter/12 mm outer diameter) under vacuum ($p \leq 15$ mTorr). Each ampoule was heated to 325 °C at a rate of 10 °C/min and was held at 325 °C for the time specified in Table 3.1. Each ampoule was then cooled to room temperature in the furnace.

Once the reaction was completed, samples were prepared for powder X-ray diffraction (PXRD). The flux was removed by mechanically scraping most of it away with a metal spatula and then by dissolving the rest by stirring the product in two approximately 10 mL aliquots of benzene (EMD Milipore, 99%) per 500 mg reaction. The product was then ground with a mortar and pestle for 2-3 min until homogenous. Once rinsed and ground, samples were placed on a zero-diffraction Si wafer and a Bruker D8 Discover diffractometer with CuK α radiation and a Lynxeye XE-T position-sensitive detector was used to collect PXRD data. EVA V6 (Bruker) was used for phase identification and Rietveld refinements were completed using TOPAS v6 (Bruker).

3.3.2 High dimensional data analysis and feature selection

Scripts used here are provided as supplemental information. The minimum and maximum change in chemical potential were calculated using the pymatgen python package to interface with the materials project and complete grand potential hull analysis to calculate the phase diagrams. [29, 30] Phase diagrams were calculated at a temperature of 300 °C using the method described by Bartel *et al.*. [30] Phase diagrams were calculated using the Grand Potential, with the system open to the relevant chalcogen. The phase boundaries resulting from these diagrams were used to determine the minimum and maximum bounds to the chalcogen chemical potential for the stability of a given target phase. Figure 3.1 shows the minimum and maximum chemical potential changes for an example phase diagram.

Based on whether each reaction follows the thermodynamic hypothesis and formed the product predicted from the phase diagram, each reaction result was manually classified as either "matches hypothesis", "does not match hypothesis", or "unclear". In this context, "matches hypothesis" means the reaction containing a flux reacted differently from the control reaction to selectively form the product predicted by the thermodynamic hypothesis, "does not match hypothesis" means the reaction with the flux did not react as predicted or reacted the same as the control, and "unclear" means both the flux reaction and control reaction formed the product predicted for the flux reaction. For these categorizations, the mole percents were calculated excluding any chalcogen present. Since the chalcogen in the flux reactions is rinsed away, at least in part, as the adduct when the excess flux is removed at the end of the reaction, it is impossible to know the exact amount of the chalcogen present in the products of the flux reactions. Therefore the chalcogen in both the flux and control reactions was removed when calculating mole percents of the products for the categorizations explained above. More information about these categorizations is included in the discussion section. The three reactions marked as "unclear" were removed from the machine learning analysis as they were inconclusive.

The chemical properties used in the following analysis are listed in Table B.3. Information on where these values are from is provided in the supplemental information. The features explored

in this analysis were chosen as they are chemical properties known to impact reactivity in other systems and be good proxies for kinetic behavior. Additionally, emphasis was put on selecting features that only require knowledge about the reactants so that this analysis would be applied to a wide array of systems.

The seaborn [31] (version 0.11.2) and Scikit-learn [32] (version 1.0.2) python packages were used for this analysis. For this analysis, the data were normalized using the standard scaler in Scikit-learn which transforms the data to have a mean of zero and standard deviation of one. The features that have the largest impact on whether a reaction follows the thermodynamic hypothesis were chosen through three different approaches: a combined thermodynamic and kinetic approach, principal component analysis (PCA), and using a random forest algorithm. For the combined thermodynamic and kinetic approach, the Seaborn python package [31] was used to create a series of plots of the minimum change in chemical potential versus every other feature. These plots were analyzed to determine the features that differentiate the most between reactions that follow the initial thermodynamic hypothesis and those that do not. To analyze each pair of variables and quickly determine the accuracy of each classification based on the limited data set, linear support vector machine (SVM) through the Scikit-learn python package [32] was used. PCA was completed using Scikit-learn to determine which features create the most separation between reactions that follow the thermodynamic hypothesis and those that do not. These features were determined by calculating which component creates the most separation and then looking at how each component was weighted in that component. The Scikit-learn python package was also used to screen various machine learning algorithms (listed in Table B.9) to see which algorithm was initially the best at accurately predicting reactivity. [32] One of the most accurate models, random forest algorithm, was chosen and the importance of each feature was calculated using Mean Decrease Impurity (MDI). The accuracy of all the machine learning algorithms used in this analysis as well as the PCA were determined by splitting the data into a training set and test set using Scikit-learn. The training set of data comprised of 70% of the full sample set and the test set was the remaining 30% of the samples. For each analysis, this was a different random 70:30 split of the data. A tool to

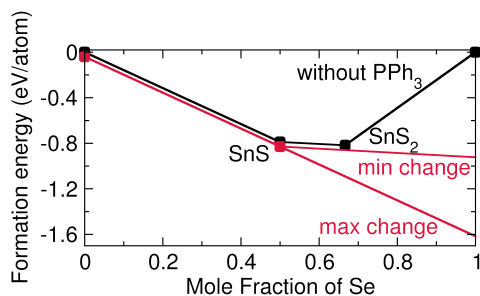


Figure 3.1: Example phase diagram of tin sulfide containing just the most stable phases showing the minimum and maximum possible change in chalcogen chemical potential for a single phase to remain on the hull.

predict future reactions was then created based of the limited features data set using both PCA and machine learning. This model was used to predict the outcome of new reactions. More information on these three analyses is provided in the SI.

3.4 Results and Discussion

Triphenylphosphine flux reactions targeting a variety of different metal chalcogenides show a triphenylphosphine flux is widely applicable; although, it does not enable selective product formation for all reactions. A summary of the triphenylphosphine flux reactions attempted, their products, and the corresponding control reactions completed without a flux is provided in Table 3.1. Of note, the iron reactant is partially amorphous as previously discussed. [15] Many syntheses reacted as expected by selectively forming a phase that is stable at the reaction temperature with the specific product predictable by the phase diagram as described previously. [15] To summarize the phase diagram predictions, the triphenylphosphine lowers the reactivity of the chalcogen through forming the adduct, thus changing the convex hull such that only one product is stable (Figure 3.2). This is the product that is selectively formed in the triphenylphosphine flux reaction. Similar to the iron selenide case, reactions with excess chalcogen still showed selectivity for the product expected according to the phase diagram. Based on the phase diagrams for many of these materials, the expected traditional synthesis would require high temperatures (700 °C to 1100 °C) in order to melt the reactants and encourage reactivity. For example, the reported syntheses of

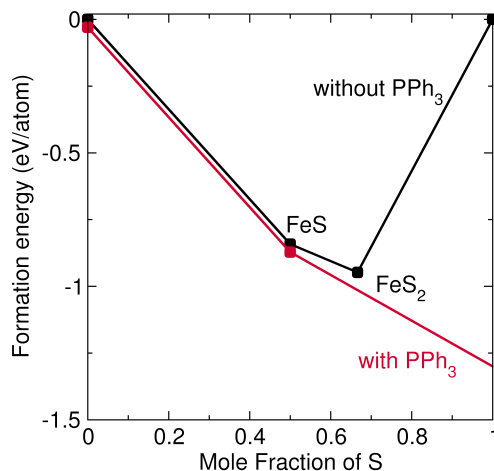


Figure 3.2: Computed formation energies ($T=0$ K, DFT) of compounds in the iron-sulfur system illustrating the convex hull (black line). [1] The offset red line approximates the convex hull with the addition of triphenylphosphine which lowers the effective chemical potential of sulfur.

both GaTe and SnS require multiple heating cycles at high temperatures. [9] A triphenylphosphine flux reaction simplifies these syntheses to a single step that can occur at a lower temperature that is easier to access. Reactions between the elements without a flux at lower temperatures such as 325 °C generally do not selectively form the desired binary product as shown in Table 3.1. This demonstrates the utility of triphenylphosphine in lowering reaction temperatures and simplifying known syntheses of metal chalcogenides with both transition metals and p-block metals.

However, not all syntheses react as predicted by the phase diagrams. Some reactions do not selectively form the predicted product with an initial 24 h reaction time. With longer reaction times, conversion to the expected product is observed. This indicates that selectivity could likely be achieved given a long enough dwell time. Lastly, some reactions did not react at all, showing that a triphenylphosphine flux reaction is not universally applicable. Here, the overarching trends in reactivity will be discussed and then a model will be created that predicts the reactivity of new systems.

3.4.1 Thermodynamic hypothesis based on phase diagrams

The phase diagram can provide an initial explanation for many of the reactions. Comparing the ranges of chemical potential change that would enable selective product formation for each reaction

Table 3.1: Table of the attempted triphenylphosphine flux reactions, the dwell times, products, and no-flux control reaction products. Mole percents, as determined through Rietveld analysis, are written in parentheses for the reactions where there were multiple products. Table continued on following page.

Reaction	Dwell time (days)	Products (mole %)	Control reaction products (mole %)
Fe + Se + 1.5PPh ₃	5	β -FeSe (99), Fe (1)	β -FeSe (46), α -FeSe (6), Fe (8), Fe ₃ Se ₄ (40)
Fe + S + PPh ₃	1	FeS	S (81) FeS ₂ (10), Fe (6), FeS (3)
Fe + 2S + PPh ₃	1	FeS	
Fe + Te + PPh ₃	1	FeTe ₂ (92), Te (8)	FeTe ₂ (29), Te (71)
Co + 2Se + PPh ₃	1	Co ₃ Se ₄ (61), Co (26), CoSe ₂ (13)	
Co + 2Se + PPh ₃	5	Co ₃ Se ₄ (90), CoSe ₂ (10)	
Co + Se + PPh ₃	1	Co ₃ Se ₄ (91), Co ₉ Se ₈ (9)	CoSe ₂ (79), Co ₃ Se ₄ (9), Co (12)
Co + Se + PPh ₃	5	Co ₃ Se ₄ (83), Co ₉ Se ₈ (17)	
Co + S + PPh ₃	1	Co ₉ S ₈	S (85), Co ₃ S ₄ (7), Co (6), Co ₉ S ₈ (2)
Co + 2S + PPh ₃	1	CoS (52), Co ₉ S ₈ (48)	
Co + Te + PPh ₃	1	CoTe ₂ (86), CoTe (14)	CoTe ₂ (75), CoTe (11), Co (14)
Ni + Te + PPh ₃	1	Ni (75), Te (18), NiTe ₂ (4), NiTe (3)	Ni (48), Te (31), NiTe ₂ (17), NiTe (4)
Ni + Te + PPh ₃	5	Ni (57), Te (31), NiTe ₂ (6), NiTe (6)	
Mn + Se + PPh ₃	1	MnSe (62), Mn (38)	Se (62), MnSe (24), Mn (14)
Mn + S + PPh ₃	1	MnS (86), Mn (14)	MnS (23), Mn (17), S (60)
Mn + Te + PPh ₃	1	Te (89), MnTe (9), MnTe ₂ (2)	MnTe ₂ (21), Te (33), Mn (44), MnTe (2)
Mn + Te + PPh ₃	5	Mn (47), Te (44), MnTe (5), MnTe ₂ (4)	

Table 3.2: Table of the attempted triphenylphosphine flux reactions, the dwell times, products, and no-flux control reaction products. Mole percents, as determined through Rietveld analysis, are written in parentheses for the reactions where there were multiple products. Continued from previous page.

Reaction	Dwell time (days)	Products (mole %)	Control reaction products (mole %)
Sn + S + PPh ₃	1	SnS (75), Sn (25)	Sn (2), S (92), SnS (6)
Sn + S + PPh ₃	5	SnS (73), Sn (22)	
Pb + Se + PPh ₃	1	PbSe	PbSe
Pb + S + PPh ₃	1	Pb	PbS (95), Pb (5)
Pb + Te + PPh ₃	1	PbTe (80), Te (20)	PbTe (82), Te (1), Pb (17)
Ga + Te + PPh ₃	1	Te (80), GaTe (20)	Ga (71), Te (28), GaTe (1)
In + Te + PPh ₃	1	In (59), In ₇ Te ₁₀ (2), In ₄ Te ₃ (11), In ₂ Te ₅ (25), In ₂ Te ₃ (3)	Te (75) In ₂ Te ₅ (25)
2Ag + Se + PPh ₃	1	Ag ₂ Se	Ag ₂ Se
2Ag + S + PPh ₃	1	Ag	Ag ₂ S (93), Ag (7)
2Ag + Te + PPh ₃	1	Ag ₂ Te	Ag ₂ Te (68), Ag (29), Ag ₅ Te ₃ (3)
Mo + 2Se + PPh ₃	1	Mo (50), MoSe ₂ (48)	Mo (49), MoSe ₂ (46), Se (5)
Mo + 2S + PPh ₃	1	Mo	Mo (26), S (74)
Ru + 2Se + PPh ₃	1	Ru	Ru (9), Se (91)
Ru + 2S + PPh ₃	1	Ru	Ru (7), S(93)
Ta + Se + PPh ₃	1	Ta	Ta
Ta + S + PPh ₃	1	Ta	Ta
Ta + Te + PPh ₃	1	Ta	TaTe ₄ (89), Ta (11)

gives insight into the reactivity. For each chalcogen, the adduct formation should change the chemical potential by the same amount, regardless of the metal. Graphs of the chemical potential ranges for each phase separated by chalcogen are shown in Figure (3.3). Comparing the chemical potential ranges within each chalcogen allows for the determination of an approximate value for each adduct (marked as a dashed black line on each graph). If this value intersects the chemical potential range for a given reaction, the reaction should be selective for the predicted product. However, if the value for the adduct is below the chemical potential range, no stable binaries would remain on the convex hull and the reaction should instead be selective for the metal. Lastly, if the adduct value is above the chemical potential range for a given reaction, then that reaction should not react selectively. Most reactions are able to be explained by this hypothesis; however, there are still some reactions that do not fit with this explanation, indicating that there are other factors besides thermodynamics that impact reactivity. Based on this hypothesis, the reactions are able to be categorized for further analysis based on whether or not they follow this thermodynamically-based hypothesis as explained in the experimental. Using these categorizations, kinetic factors that may impact reactivity can be explored.

3.4.2 Exploring kinetic factors

To determine what properties had the largest impact on whether or not a reaction follows the thermodynamic hypothesis described above, a combined thermodynamic and kinetic approach, PCA, and a random forest algorithm-based approach were used. A combination of these three techniques was used as each has limitations especially given the small sample size and correlated features being analyzed. The combined thermodynamic-kinetic approach provides a useful starting point, but is ultimately still based on thermodynamics. PCA is not great at feature extraction, but handles correlated data well, which is important given the number of correlated features present used. Random forest algorithms are complimentary to PCA in that they do not handle correlated features well, but are very good at feature extraction. Since all of these approaches have different

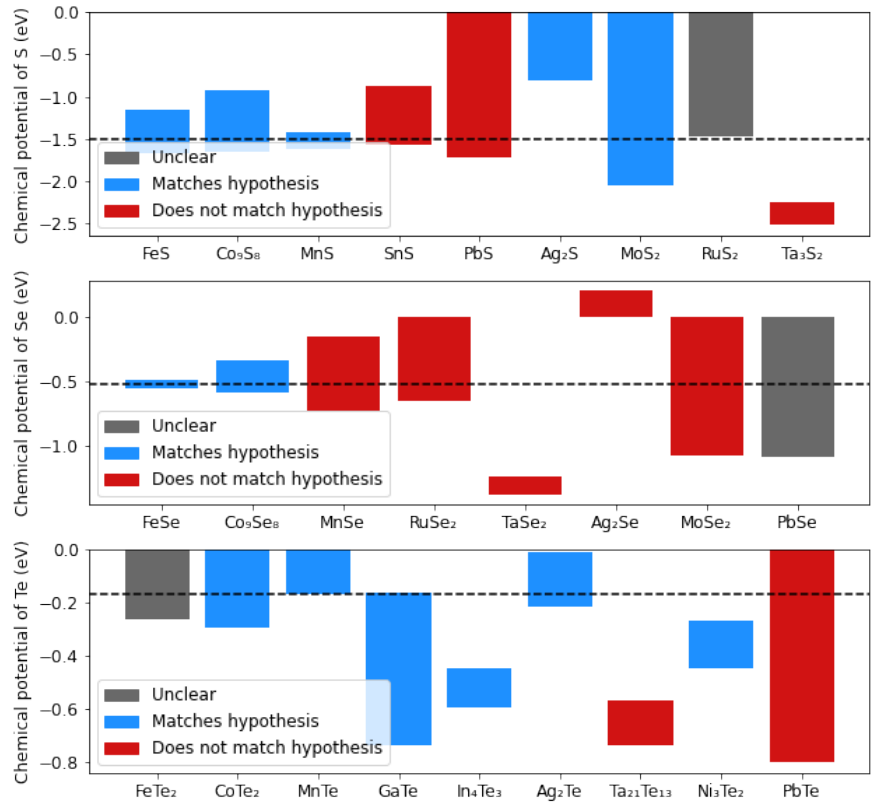


Figure 3.3: Chemical potential range where each given phase is the only phase on the convex hull. Black dashed lines represents the proposed chemical potential change of each adduct.

strengths and weaknesses, using all three can provide the most complete picture of the kinetic properties impacting reactivity.

For the combined approach, the thermodynamic hypothesis was used as a starting point for exploring the impact of the various kinetic factors. Based on the thermodynamic hypothesis discussed above, the minimum change in chemical potential was identified as the main important factor. A series of plots were made graphing each feature versus the minimum chemical potential change. These graphs were then analyzed using linear support vector machine (SVM) to determine which feature creates the most separation and consequently has the largest impact on whether or not a reaction follows the thermodynamic hypothesis (Figure 3.4). This analysis shows that the density of the metal is the most accurate predictor of whether or not a reaction follows the thermodynamic hypothesis. This makes sense as more dense metals are generally less reactive. The second most impactful features for creating separation between reactions that follow the thermodynamic hypothesis and those that do not are as follows: formation energy, adduct bond dissociation energy, metal electronegativity, chalcogen electronegativity, metal melting point, chalcogen melting point, metal atomic number, chalcogen atomic number, and chalcogen ionization energy.

To confirm the combined thermodynamic and kinetic approach, the features were analyzed using two computational approaches: PCA (Figure 3.5) and random forest algorithm (Figure 3.6). PCA does not fully capture the data and is only 71% accurate based on its ability to predict the outcome of the reactions set aside to test the model. The first principal component was determined to create the most separation in the data, thus the composition of this component was used for feature extraction. According to PCA, the features that create the most separation between reactions that follow the thermodynamic hypothesis and those that do not were the chalcogen atomic number, chalcogen density, adduct bond dissociation energy, chalcogen melting point, chalcogen electron affinity, and chalcogen ionization energy (Figure 3.5). Although this a large selection of features, there is overlap with the features selected by the combined thermodynamic and kinetic approach. Machine learning algorithms also do not fit the data very well with most of the algorithms being 71% accurate. The random forest algorithm was chosen as it was one of the most accurate models,

and once it is fine-tuned it is 85% accurate. The most important features according to the random forest algorithm (Figure 3.6) were the metal atomic number, metal electronegativity, average density, metal density, and metal melting point. The features from both PCA and the random forest algorithm show some agreement with the features from the combined thermodynamic and kinetic approach.

The key kinetic properties were picked based on which features are present in at least two of the analysis techniques. Based on this, the minimum change in chemical potential, metal density, bond dissociation energy of adduct, metal electronegativity, melting point of the metal, melting point of the chalcogen, metal atomic number, chalcogen atomic number, and ionization energy of the chalcogen were determined to be the most impactful properties. It is important to note that a number of these properties are correlated, but they still provide a basis to understand the reactivity of these systems. For example, the key properties of the metal such as density and melting point are known proxies for kinetic behavior in reactions. Metals that are dense and have high melting points are known to be less reactive regardless of the thermodynamics of the reaction. Additionally the bond dissociation energy of the adduct in particular makes sense as being important. If the chalcogen-phosphorous bond in the adduct is stronger, the adduct is less reactive and the expected product is less likely to form. Therefore, the reactivity is based on how reactive the metal is and how stable the adduct is. Regardless of potential correlations, the properties listed above were used to create a model to predict the outcome of future reactions.

3.4.3 Creating a model to predict reactivity

Using the limited feature set chosen from the above analysis, a model combining PCA and a machine learning algorithm was created. Using both techniques should provide the greatest accuracy as the techniques are complimentary. A set of new reactions (Table 3.4) was analyzed using this model to predict whether or not the reaction would be successful. The results of these predictions are provided in Table 3.4. The reactions and their corresponding control reactions were completed to demonstrate the efficacy of the model. The predictions align with the exper-

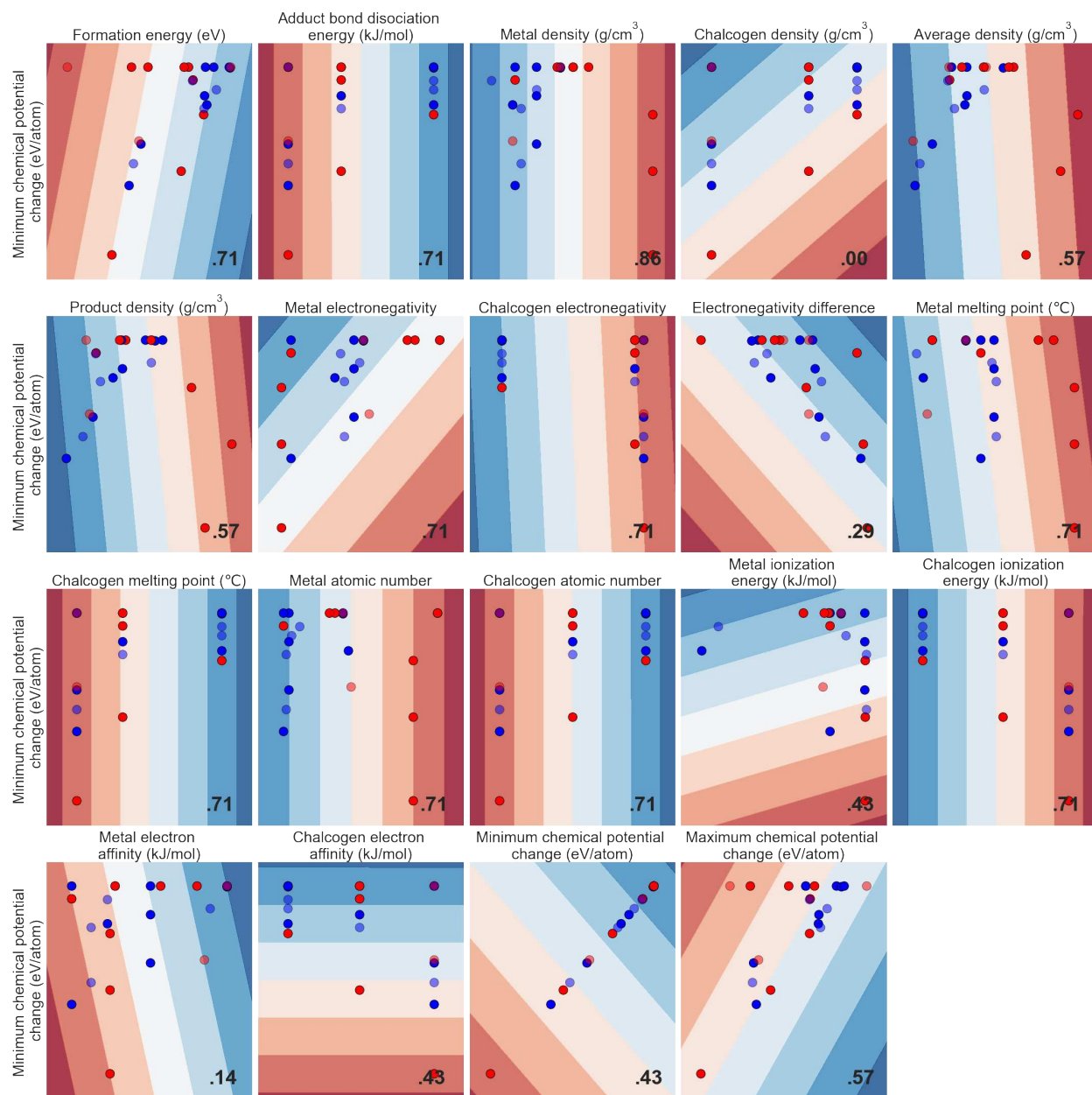


Figure 3.4: Plots of each feature graphed versus the minimum change in chemical potential analyzed using SVM. The accuracy is written in the bottom right corner of each graph.

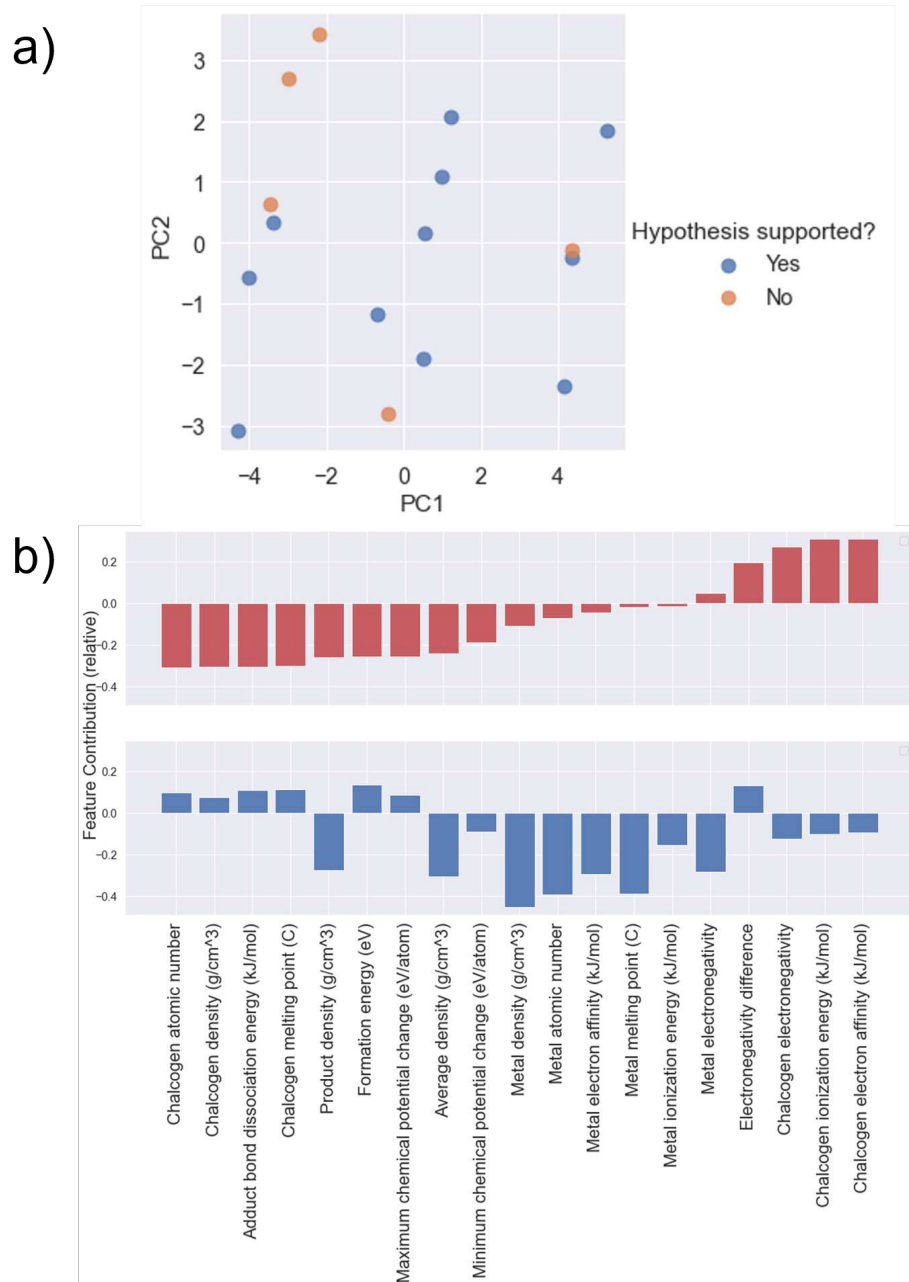


Figure 3.5: (a) Visualization of the dimensionally reduced data set (from 19 to 2 dimensions) plotted along the 2 principal component axis determined from PCA. The individual points are color coded by their classification of hypothesis supported: Yes/No. (b) Relative feature contributions to the two principle components used to plot the data in (a).

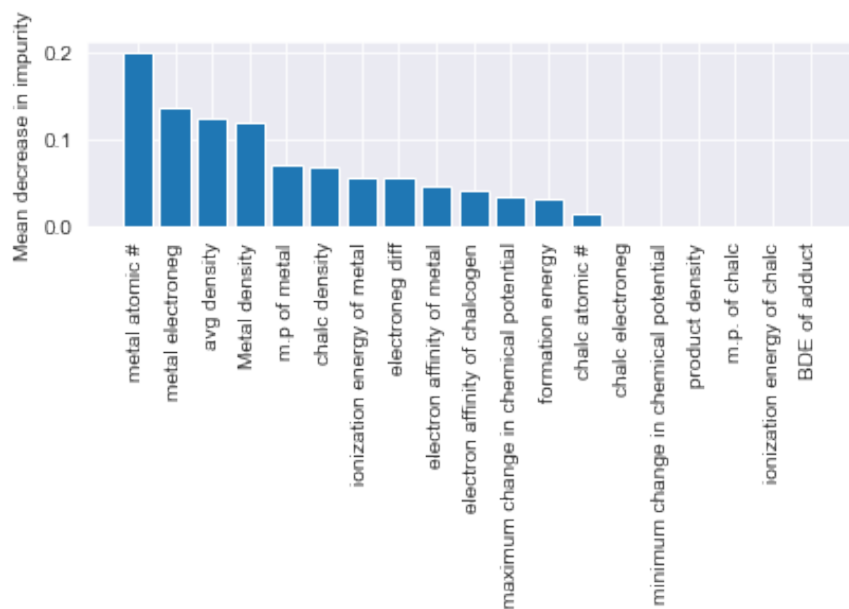


Figure 3.6: How well each feature separates reactions that follow the thermodynamic hypothesis from those that do not based on the random forest algorithm.

Table 3.3: Table of test reactions including the features, predicted outcome, and actual outcome. Continued below.

Reaction	Product according to thermodynamics	Adduct bond dissociation energy (kJ/mol)	Metal density (g/cm ³)	Metal electronegativity
Nb + Se	Nb ₂ Se	-64.95054178	8.57	1.6
Nb + S	Nb ₁₄ S ₅	-78.58340988	8.57	1.6
Cr + Se	Cr ₂ Se ₃	-64.95054178	7.19	1.66
Cr + Te	Cr ₂ Te ₃	-41.1625301	7.19	1.66
Cu + S	Cu ₇ S ₄	-78.58340988	8.96	1.9

imental outcome demonstrating the utility of this model in predicting reactivity and confirming experimentally the importance of the minimum chemical potential change, metal density, adduct bond dissociation energy, metal electronegativity, metal melting point, chalcogen melting point, chalcogen atomic number, and chalcogen ionization energy.

3.5 Conclusions

A variety of metal chalcogenides were successfully synthesized at low temperature using a triphenylphosphine flux showing the broad applicability of these reactions. The phase diagrams

Table 3.4: Table of test reactions including the features, predicted outcome, and actual outcome. Continued below.

Reaction	Metal melting point (°C)	Chalcogen melting point (°C)	Metal atomic number	Chalcogen atomic number
Nb + Se	2477	221	41	34
Nb + S	2477	115.21	41	16
Cr + Se	1907	221	24	34
Cr + Te	1907	449.51	24	52
Cu + S	1084	115.21	29	16

Table 3.5: Table of test reactions including the features, predicted outcome, and actual outcome. Continued from above.

Reaction	Chalcogen ionization energy (kJ/mol)	Minimum chemical potential change (eV/atom)	Predicted product	Did it react as predicted?
Nb + Se	941	-1.5045	Nb	Yes
Nb + S	999.6	-2.5766	Nb	Yes
Cr + Se	941	-0.3694	Cr ₂ Se ₃ or Cr	Yes
Cr + Te	869.3	-0.2793	Cr	Yes
Cu + S	999.6	-1.036	mixture of products	Yes

were found to dictate the product selected for in these reactions as was previously discussed in the case of iron selenide. The reactivity of these systems can be explained looking at both thermodynamics through the phase diagrams and kinetics. The reactivity of the metal and stability of the adduct were found to be the most impactful kinetic properties in determining whether or not a given reaction would be selective. A model was created and its efficacy was demonstrated as it was used to predict the outcome of new reactions. This chapter demonstrates the ability of triphenylphosphine to enable reactivity at low temperatures in a variety of metal chalcogenide systems to selectively form stable low-temperature phases. It additionally explains the guiding principles behind the reactivity, wherein a reactive metal (a metal with a lower density and higher melting point) and a more reactive adduct are necessary. These properties are also able to predict future reactivity. Knowing these guiding principles allows for synthesis by design and expanding this reaction to other systems.

Chapter 4

A New Cobalt-Selenium-Triphenylphosphine Cluster Synthesized with a Triphenylphosphine Flux³

4.1 Overview

Metal chalcogenide clusters have shown promise for a wide array of applications including catalysis and energy storage. Finding new clusters and new ways to make these clusters is therefore important for advancing these technologies. This chapter describes a new possible cobalt-selenium-triphenylphosphine cluster synthesized in a non-traditional elemental reaction performed in molten triphenylphosphine. While the evidence points to this material being a cluster with the approximate size of $\text{Co}_{12}\text{Se}_{16}(\text{PPh}_3)_{10}$, the exact size and composition is yet undetermined. Therefore, some alternate hypotheses for the identity of the material are discussed including a selenium radical complex, and a simpler cobalt selenide based material. Regardless of the identification, this work describes a new material, sheds light on a reaction pathway, and demonstrates the utility of using reactions involving molten organic compounds to discover new materials.

4.2 Introduction

Monolayer protected metal chalcogenide clusters are a topic of intense contemporary research. These species can be synthesized to atomic precision and have proven effective in an array of applications including catalysis and energy storage. [33] Cobalt selenide clusters, including cobalt-

³This chapter is a manuscript in preparation, with additional experiments still necessary. M. Jewels Fallon completed the synthesis, most of the characterization and properties measurements, and wrote the initial manuscript. Ian D. Anderson, under guidance of Christopher J. Ackerson, completed the MALDI-MS experiments, and provided valuable assistance with analysis and writing. Clara A. Tibbetts, under guidance of Amber T. Krummel, did the FTIR experiments and analysis. James R. Neilson assisted with data analysis, editing, and provided useful discussion. This work was supported by the National Science Foundation (DMR-1653863). The authors wish to thank the Analytical Resources Core (RRID: SCR_021758) at Colorado State University for instrument access, training, and assistance with sample analysis. This research used resources of the Advanced Photon Source, a U.S. Department of Energy (DOE) Office of Science User Facility operated for the DOE Office of Science by Argonne National Laboratory under Contract No. DE-AC02-06CH11357. The mail-in program at Beamline 11-ID-B contributed to the data.

selenide-triethylphosphine (PEt₃) clusters, show particular promise as recyclable sodium ion battery electrode materials, when assembled into hierarchical microporous structures. [34] Such assemblies differ substantially from other storage materials, as the cluster precursor affords a degree of tunability which is generally inaccessible for bulk or amorphous counterparts. [35, 36]

The relatively high symmetry and small size of these clusters also gives rise to a concentric series of electronic shells with a valence reminiscent of a single atom. [37, 38] Molecular clusters of this kind are generally referred to as superatoms and can be viewed as an extension of the standard periodic table into a third dimension, wherein specific physical properties can be obtained through judicious control of the superatom size, shape, and composition. [39, 40] This principle has been applied recently using Co₆Se₈L₆, where L represents various phosphine ligands. [41] Overall this cobalt selenide cluster serves as a good model system to investigate superatomic cluster chemistry given its high electronic stability and affinity for ligand variation.

However, there is currently a relative dearth of cobalt selenide clusters beyond this nuclearity. In order to more completely explore the properties of cluster-assembled materials, it is of general interest to develop pathways to additional cluster sizes and shapes. Champsaur *et al.* recently demonstrated that Co₆Se₈(PEt₃)₆ can be transformed into Co₁₂Se₁₆(PEt₃)₁₀ through a three-step process involving i) carbonyl-for-phosphine exchange, ii) carbene-for-carbonyl exchange, and iii) subsequent irradiation to remove the labile carbene thereby inducing dimerization. [5] The resulting product retained the overall geometry of the individual cluster monomers and exhibited strong electronic coupling and electron delocalization across the dimerized cluster.

Herein we describe the synthesis of a potential cobalt-selenium-triphenylphosphine (PPh₃) cluster, with a composition approximately matching Co₁₂Se₁₆(PPh₃)₁₀, but whose physical properties differ from the abovementioned case. To our knowledge, this may be the first reported example of a direct synthetic route to this species, and therefore could represent a significant development in metal chalcogenide cluster chemistry. The formation conditions are also rather unique for the field, given the elemental reaction is a single step. Based on a series of characterizations we offer some insight towards the stability of this new cluster species, as well as a putative formation pathway.



Figure 4.1: Picture of the completed reaction in sealed tube (left) with the blue material on the top of cobalt selenide powder. The product after solidifying and being ground (middle) and the crystals scraped from the side of the tube (right).

Alternate hypotheses for what this material could be are also discussed, as structure determination via diffraction remains elusive. This work provides evidence of a new metal chalcogenide cluster as well as insight into the synthesis of these materials.

4.3 Experimental

4.3.1 Synthesis

Cobalt powder (NOAH Technologies Corporation, 99.9%), selenium powder (Sigma Aldrich, 99.5%) and triphenylphosphine flakes (Alfa Aesar, 99+%) were used for this reaction. A 6:6:1 mole ratio of cobalt:selenium:triphenylphosphine was sealed under vacuum ($p \leq 15$ mTorr) in a fused SiO_2 ampoule (10 mm ID/12 mm OD). The ampoule was heated at a rate of 10 °C/min to 325 °C and dwelled at that temperature for 5 days. After 5 days at 325 °C, the furnace was turned off and the ampoule was cooled in the furnace. After the reaction was completed, the blue liquid poured off the top and collected and the blue crystals (Figure 4.1) were scraped off the inside of the tube using a metal spatula leaving the black cobalt selenide powder behind in the tube.

A control reaction between cobalt and triphenylphosphine was completed in the same way as described above but with a 1:1 mole ratio of cobalt:triphenylphosphine.

4.3.2 Crystallization attempts

To attempt crystallization through reheating, the blue powder was sealed in a fused SiO_2 ampoule (10 mm ID/12 mm OD) under vacuum ($p \leq 15$ mTorr). The ampoule was heated at a rate of

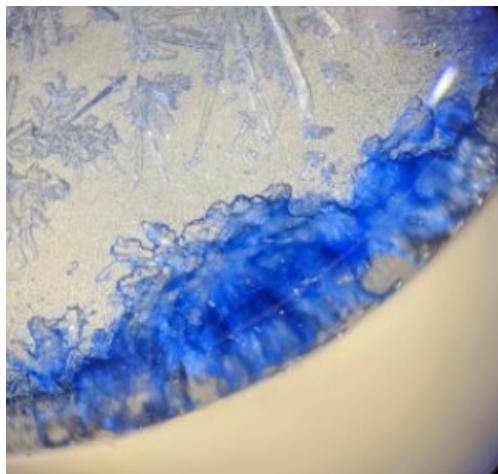


Figure 4.2: Picture of the crystals formed after slow-evaporation of Benzene.

10 °C/min to 500 °C where it dwelled for 24 h before being cooled in the furnace. An additional attempt repeated this same process heating up to 400 °C.

To attempt crystallization through solvent-based dissolution and evaporation, the blue material was placed in several different solvents. Benzene, dichloromethane, tetrahydrofuran, acetone, toluene, isopropanol, and chloroform were used in an attempt to dissolve the material, and each showed partial dissolution. The sample added to Benzene was from a 1:1:1 molar ratio of Co:Se:PPh₃ which was a lighter blue color likely due to the dilution caused by excess triphenylphosphine. This sample was left loosely capped to evaporate over the course of a week. This sample formed crystals of triphenylphosphine surrounded by an amorphous, blue, gel-like material (Figure 4.2).

4.3.3 Matrix-Assisted Laser Desorption/Ionization Mass Spectrometry (MALDI-MS)

0.2 mg of the matrix trans-2-[3-(4-tert-Butylphenyl)-2-methyl-2-propenylidene]malononitrile (Sigma Aldrich, 99.0% [HPLC]) was dissolved in 0.2 mL dichloromethane (Sigma Aldrich, 99.5%, stabilized with 40-150 ppm amylene). 2.0 µL of the cluster sample suspended in dichloromethane was added to the solution to produce a mixture of approximate 1:100 sample to matrix ratio. 0.2 µL of this combined solution was spotted on a steel MALDI plate and allowed to dry for one hour.

Data was collected using a Bruker Microflex LFR MALDI-TOF. Positive mode spectra were collected as they provided better signal-to-noise ratios relative to negative mode spectra.

4.3.4 X-ray diffraction

For powder X-ray diffraction (PXRD), a mortar and pestle was used to grind the products for 2-3 min until homogeneous. Of note, the blue cluster proved challenging to grind, and tended to clump together rather than grind into a powder. The samples were then placed on a zero-diffraction Si wafer and PXRD was collected using a Bruker D8 Discover diffractometer with $\text{CuK}\alpha$ radiation and a Lynxeye XE-T position-sensitive detector.

Some crystals collected from the inside of the ampoule were set aside for single crystal X-ray diffraction (SCXRD). The crystals were measured on a Bruker D8 Advance QUEST at room temperature. These crystals were found to be amorphous according to diffraction and attempts to recrystallize them were unsuccessful. Information on re-crystallization attempts is provided in the SI

Due to the large amount of diffuse scattering observed in PXRD, Pair Distribution Function (PDF) analysis of synchrotron total scattering data was used to investigate local order. The material was packed in a 0.0395" inner diameter x 0.0435" outer diameter kapton capillary and sealed using epoxy. Data were collected on the 11-ID-B beamline at the Advanced Photon Source at Argonne National Laboratory. All samples were collected with a detector distance of around 200 mm. To calibrate the sample-detector distance, a CeO_2 standard was measured, and to calibrate instrument parameters in quantitative modeling of the PDF, a Ni standard was also measured. The wavelength was 0.2115 Å and a Q_{max} of 23 Å⁻¹ for PDF was used during data transformation. The raw data was transformed to PDF using GSAS-II and then PDFgui was used to analyze the transformed data. [23, 24]

4.3.5 Fourier transform infrared spectroscopy

All attenuated total reflectance (ATR) Fourier transform infrared spectroscopy (FTIR) measurements were made on a Bruker Optics Hyperion 3000 spectrometer with a germanium crystal

tipped ATR attachment. Samples for FTIR were all ground as explained above before measurement. Samples were placed on a glass microscope slide and flattened with a scoopula before measurement. Pressure level 1 (contact pressure equal to 0.5 N) was used, the spectral resolution is 2 cm^{-1} , and 64 scans were averaged together. The detector used was a single element mercury cadmium telluride (MCT) detector.

4.3.6 Magnetism

Approximately 10 mg of the material was placed into a Vibrating Sample Magnetometry (VSM) capsule. The capsule was loaded onto a Quantum Design Inc. Magnetic Properties Measurement System (MPMS3). VSM was used to collect the zero field cooled magnetization from 1.8 K to 300 K at a field strength of $H = 100\text{ Oe}$.

4.3.7 Ultraviolet-Visible spectroscopy

The sample was prepared for UV-Visible spectroscopy (UV-Vis) by mixing 5 wt% of the powdered cluster with 95 wt% of barium sulfate (Baker Chemical Co., 99+%). UV-Vis data was collected on the sample in a scintillation vial using an Ocean Insight Flame miniature spectrometer with an Ocean Optics halogen light source HL-2000-FHSA. A dark measurement and light measurement of a barium sulfate standard in a scintillation vial were also collected.

4.4 Results

The blue material recovered from the Co-Se-PPh₃ reaction was characterized using a number of different techniques. MALDI-MS shows the upper bound of the envelope being around 6000 m/z with the center being at 4214.9 m/z. The matrix for this sample does not have any signal above 1000 m/z and therefore is not seen in this data. Looking at the differences between peaks, there are changes in m/z that correspond to both the loss of selenium and the loss of cobalt, indicating the presence of both elements.

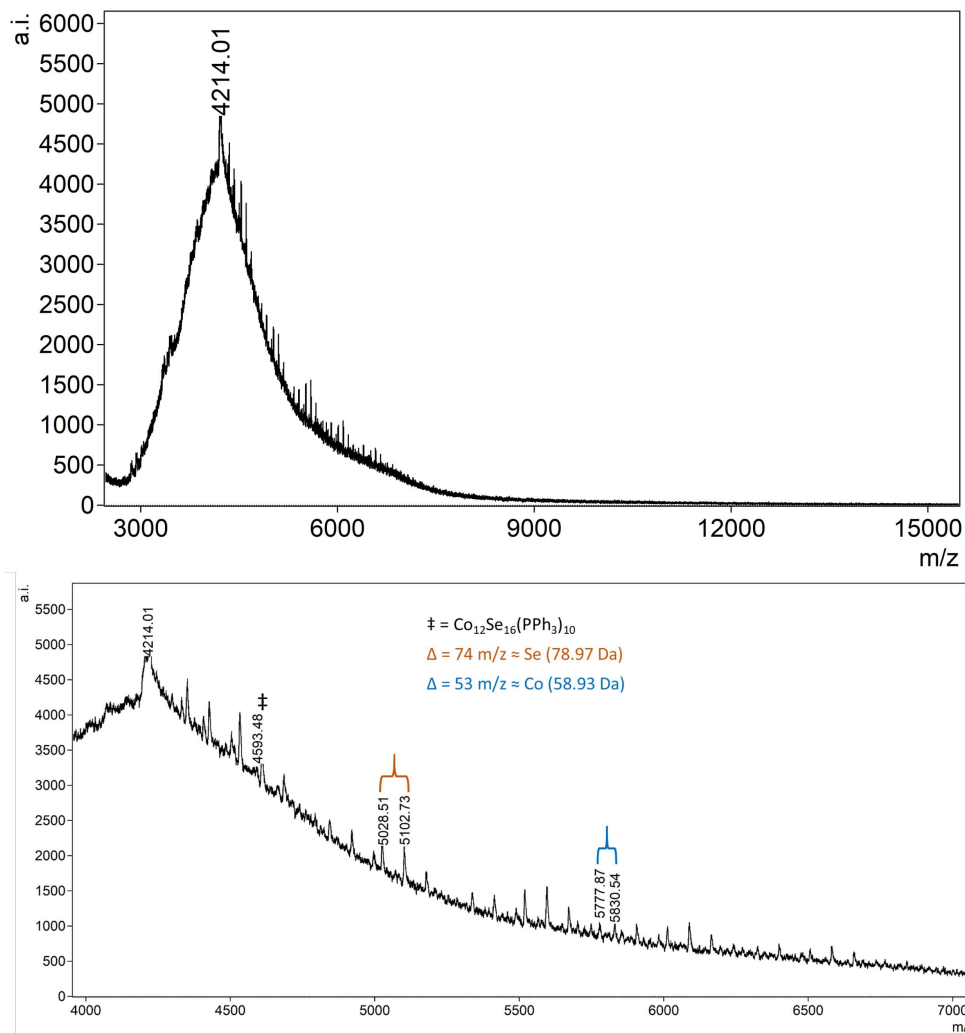


Figure 4.3: Complete MALDI-MS spectrum of the blue material (top) and zoomed in section of the spectrum (bottom) labelled with the hypothesized cluster size and peak differences corresponding to loss of selenium and loss of cobalt.

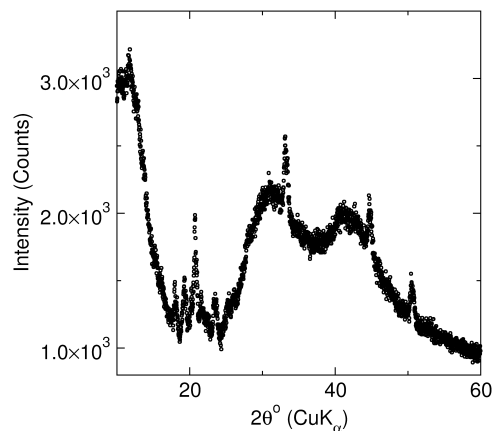


Figure 4.4: PXRD of the blue material

PXRD (Figure 4.4) shows that the material is largely amorphous with weak peaks visible in the powder pattern corresponding to cobalt selenide. SCXRD of the crystals shown in Figure 4.2 formed through slow-evaporation of benzene indicate that the clear crystals are triphenylphosphine. SCXRD of the needle-like blue material scraped directly from the tube shown in Figure 4.1 was unsuccessful, as the material did not diffract. Thus, pair distribution function (PDF) analysis was used as a tool to explore the atomic structure. The PDF analysis is able to be mostly fit by CoSe with some peaks being fit by triphenylphosphine and some peaks at shorter r values are not well fit (Figure 4.5). Explanations for these peaks are explored in the discussion section.

Attempts to recrystallize the material through heating or through dissolution and slow-evaporation were unsuccessful. For all the solvents attempted, the blue material was only partially soluble, creating a slurry instead of fully dissolving. Slow evaporation of benzene did not produce any crystals. Heating the blue material up to 500 °C caused it to decompose into Co_3Se_4 , Co_2P , and CoP as well as turned the ampoule a gold color (Figure 4.6). The recrystallization attempt at 400 °C also seemed to decompose the blue material. The decomposition products at this temperature were not able to be identified as they produced a large number of weaker peaks at lower angle in the diffraction pattern (Figure 4.7). As a wide array of materials could fit these peaks it was not possible to identify the decomposition products; although, the presence of peaks at low angle suggests a large complex unit cell which could be organic in nature.

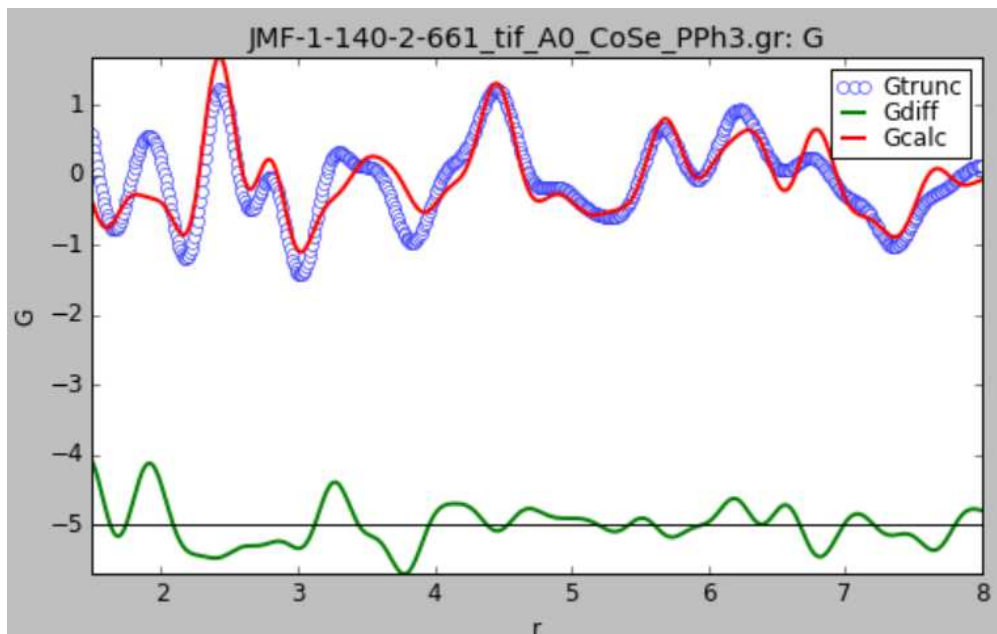


Figure 4.5: PDF analysis of the blue material fit with CoSe (red line) with the difference curve in blue.

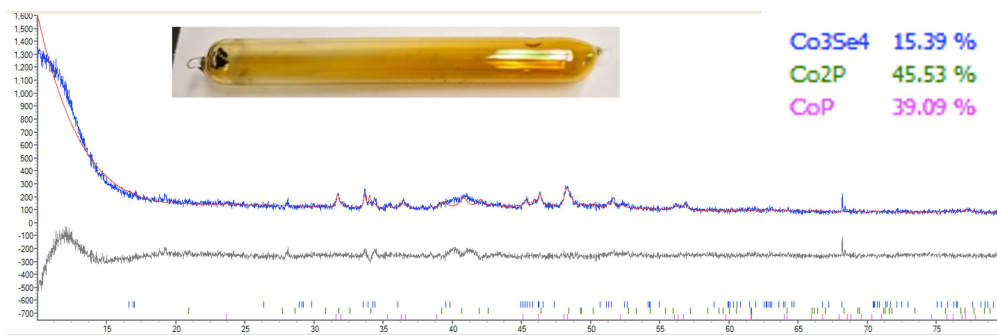


Figure 4.6: Diffraction pattern of the products from the attempted recrystallization reaction at 500 °C. Rietveld refinement (red line) includes the materials listed in the upper right with their weight percents. Inset shows the tube when it was removed from the furnace.

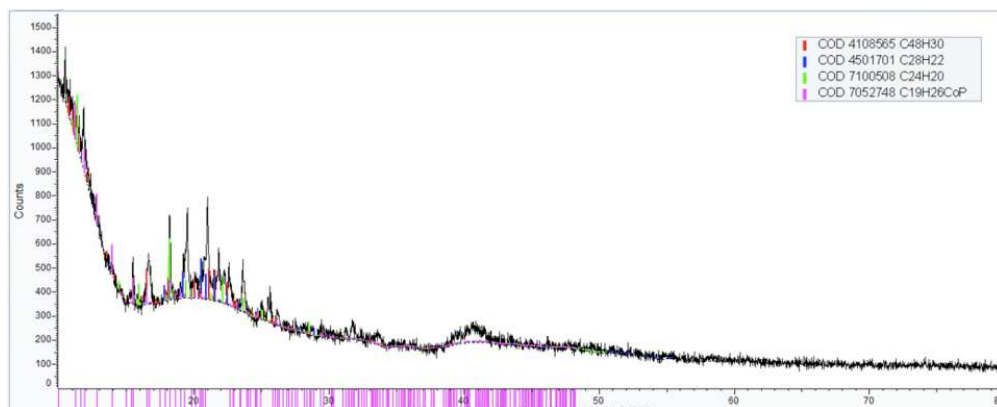


Figure 4.7: Diffraction pattern of the products from the attempted recrystallization reaction at 400 °C. Tick marks show the peaks for the phases listed in the top right.

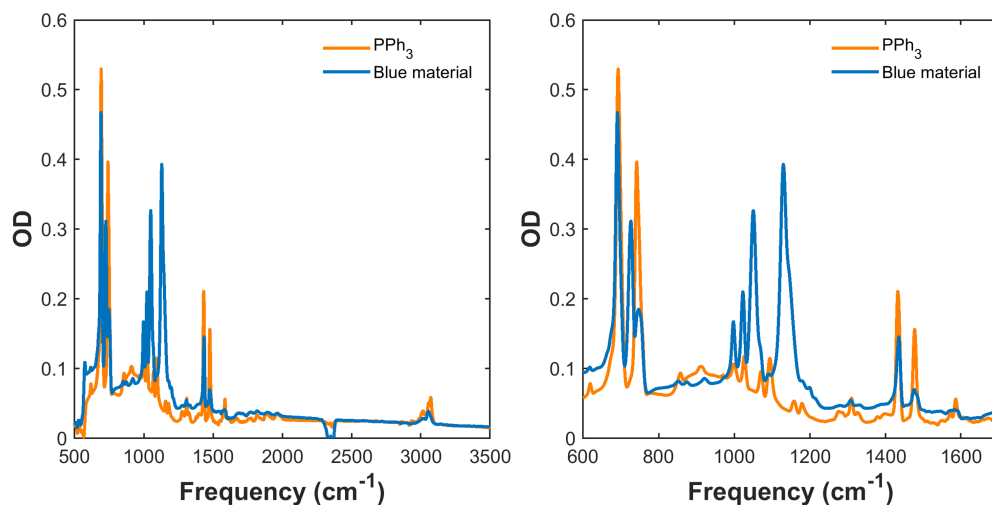


Figure 4.8: Full FTIR spectra (left) and spectra zoomed in on the lower wavenumber peaks (right) of triphenylphosphine (orange) and the blue material (blue).

Attempts to acquire characteristic Nuclear Magnetic Resonance (NMR) spectra of the blue material were unsuccessful due to the difficulty getting the material to dissolve. NMR was attempted in both benzene and chloroform and the partial solubility in both these solvents was not enough to produce a signal in the measurement.

FTIR shows differences between the spectra for triphenylphosphine and the blue material. The numerous vibrational modes associated with triphenylphosphine have been laid out in prior research by Clark *et al.* [42] The peaks in the spectra of both triphenylphosphine and the blue material align with peak identifications for triphenylphosphine described by Clark *et al.* [42] There are some peak shifts to higher wavenumber in the blue material.

Magnetism measurements show that the blue material is paramagnetic based on the decrease in magnetic susceptibility with increased temperature, which is characteristic of paramagnetism (Figure 4.9).

The UV-Vis spectrum shows a broad absorbance range from 500-700 nm. It appears to contain a series of peaks with centered around 600 nm which aligns with the blue color of the compound.

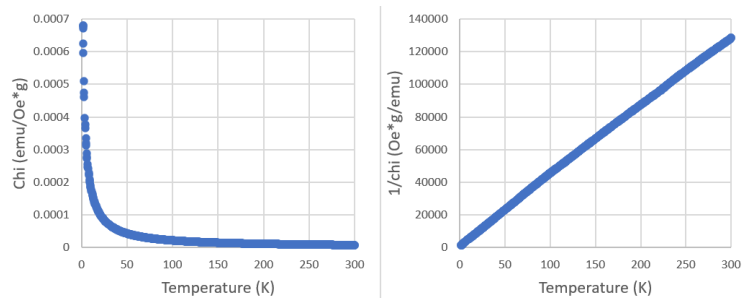


Figure 4.9: Magnetic susceptibility (left) and inverse magnetic susceptibility (right) versus temperature of the blue material.

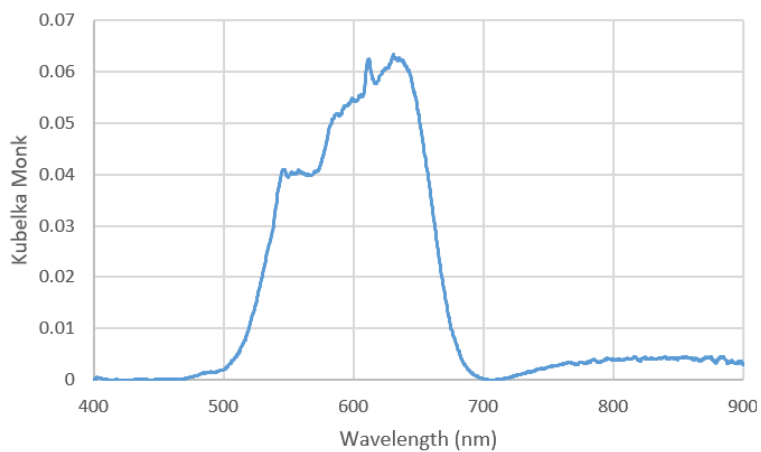


Figure 4.10: Kubelka Monk function converting the reflectance data into absorbance of the blue material from diffuse reflectance data.



Figure 4.11: Sealed ampoule containing the cobalt-triphenylphosphine reactions (left) and the blue material from this reaction after being removed from the ampoule (right).

Completing the reaction without selenium also forms a liquid, but a more teal color instead of blue (Figure 4.11). Additionally, the liquid did not solidify like the blue material did upon opening the tube.

4.5 Discussion

4.5.1 Hypothesis: $\text{Co}_{12}\text{Se}_{16}(\text{PPh}_3)_{10}$ Cluster

MALDI-MS is capable of identifying cluster products, as it provides detail regarding formulation and surface chemistry. [43–46] Figure 4.3 shows the MALDI mass spectrum of the obtained synthetic product, which features a single envelope roughly 3000 m/z in width with a center near 4214.9 m/z. The best match for this data corresponds to the formula $\text{Co}_{12}\text{Se}_{16}(\text{PPh}_3)_{10}$ (calculated: 4593.65 m/z). Given the sub-ideal matrix-sample combination used due to the difficulty dissolving the samples, this difference of 300 m/z is within the expected error for this measurement. A peak corresponding to this formula, as well as several peak differences corresponding to the loss of selenium or cobalt, can be observed within the upper bound of the envelope (Figure 4.3).

Envelopes such as this one are generally indicative of i) impure sample containing multiple closely-spaced nuclearities, ii) a high degree of fragmentation resulting from suboptimal matrix-sample interaction, or iii) a combination of the two. Due to the high sensitivity towards impurities in clusters particularly inherent to magnetism measurements (Figure 4.9), we rule out the likelihood of a complex product mixture. Previous research has demonstrated that product mixtures lead

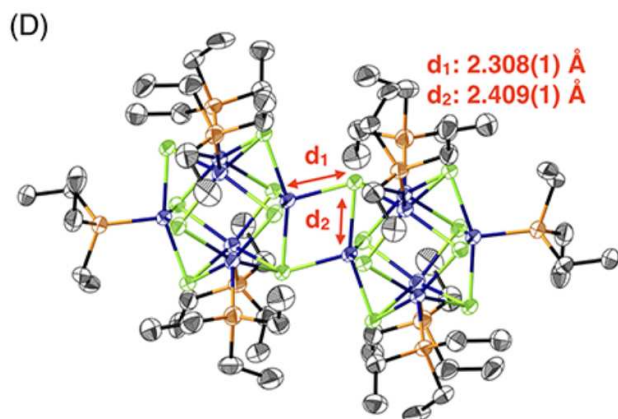


Figure 4.12: Structure of the $\text{Co}_{12}\text{Se}_{16}(\text{PET}_3)_{10}$ cluster with blue being cobalt, green being selenium, orange being phosphorous, and grey being carbon. Hydrogens omitted for clarity. Figure from Champsaur *et al.*. [5]

to complex magnetism data. [47] The novel nature of this sample renders direct comparison to other studies tenuous, as MALDI-MS is known to be sensitive to the specific cluster identity. [48] $\text{Co}_{12}\text{Se}_{16}(\text{PET}_3)_{10}$, the most related reported cluster, unfortunately does not currently have any available mass spectrometric data. [5] This may be due in part to the lack of an optimal matrix pairing for cobalt selenide clusters, as this area to date has almost exclusively been advanced for coinage metal clusters. [49]

Additional evidence supporting the blue material being a cluster is provided through total scattering studies. Although the PDF analysis is largely fit by cobalt selenide and triphenylphosphine, the peaks at lower r that are not well fit are consistent with a cluster. Due to their size, clusters tend to have more intense peaks at short r values. The PDF analysis compared to a calculation of the $\text{Co}_{12}\text{Se}_{16}(\text{PET}_3)_{10}$ cluster shows some overlap in the peaks although it does not fit the data well. (Figure 4.13). The inability to fit the data better is possibly due to the fact that the comparison was attempted with the triethylphosphine cluster as an approximation which would fit differently than the triphenylphosphine cluster. It is also possible that the blue material is a cluster of a different size. The fact that the PDF analysis shows peaks at lower r supports the conclusion from the mass spec data of the blue material being a cluster potentially around the size of $\text{Co}_{12}\text{Se}_{16}(\text{PPh}_3)_{10}$.

The FTIR (Figure 4.8) data supports the hypothesis that the blue material is a cluster similar to the $\text{Co}_{12}\text{Se}_{16}(\text{PET}_3)_{10}$ cluster. In this cluster, triphenylphosphine is bound to cobalt and then se-

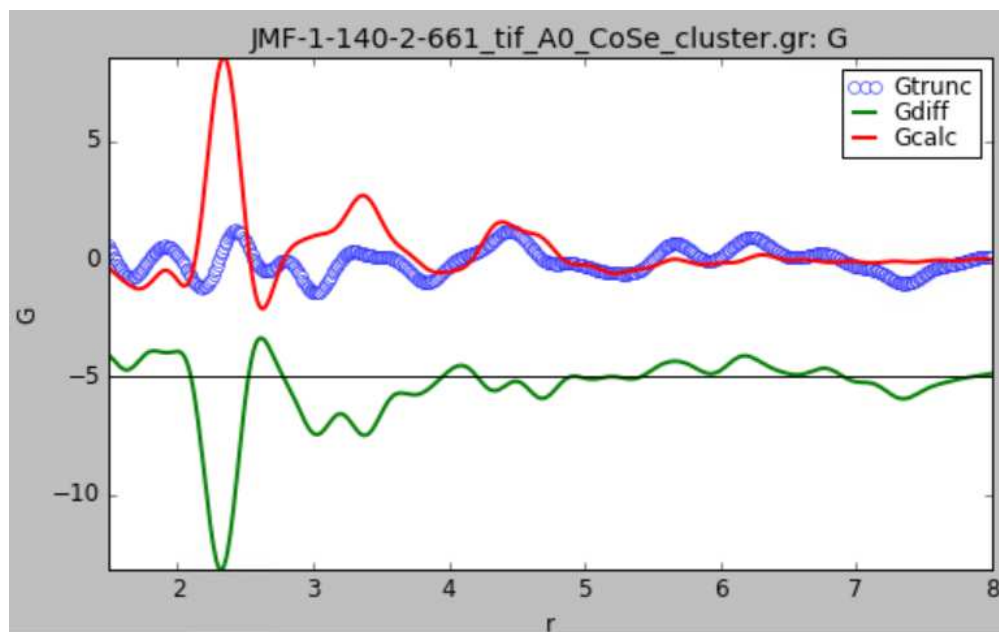


Figure 4.13: PDF analysis of the blue material compared with a calculation of the $\text{Co}_{12}\text{Se}_{16}(\text{PEt}_3)_{10}$ cluster (red line) with the difference curve in blue.

lenium, thus, it is likely that some observed differences in the spectra stem from mass dependent shifts. Clark *et al.* showed for a series of mass-sensitive modes that increased substituent mass led to a decreases in frequency. [42] For example, one of three C-X stretching motions in unsubstituted triphenylphosphine shows up around 1098 cm^{-1} . [42] [50] In the FTIR spectrum of triphenylphosphine we see a significant peak centered at 1096 cm^{-1} and in the cobalt cluster spectrum there is only a very weak peak. However, in the FTIR spectrum of the blue material, there is a large new peak at 1050 cm^{-1} (Figure 4.14). It is possible that this new peak is from a C-X stretching motion with X being the cobalt selenide unit that the triphenylphosphine is bound to. This provides additional evidence for cluster formation.

The difficulty with solubility also supports the hypothesis that the blue material is a cluster. Previous work on cobalt chalcogenide triphenylphosphine clusters has shown they have limited solubility in all common solvents. [51] This lack of solubility also causes a lack of NMR data on these compounds. Additionally, many metal chalcogenide clusters are paramagnetic and have broad absorbance as observed with this material. [51,52]

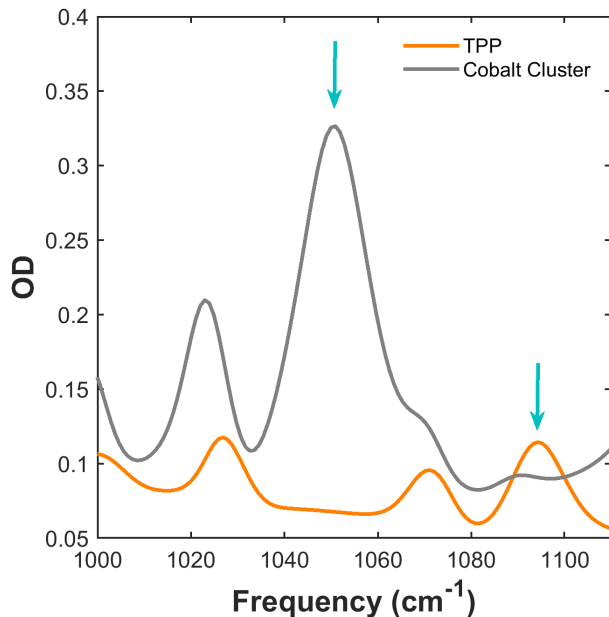


Figure 4.14: Section of the FTIR spectra of triphenylphosphine (orange) and the blue material (grey). Arrows show the mass-dependant peak shift

It is worth noting that while a cluster seems likely, the exact size of the cluster is undetermined, although comparison to the $\text{Co}_{12}\text{Se}_{16}(\text{PEt}_3)_{10}$ cluster provides a good estimation. This prompts the alternate hypothesis that the material is a cluster of a different size. Transmission electron microscopy (TEM) and Energy dispersive X-ray Spectroscopy (EDS) would be useful tools to help identify whether the material is a cluster and what the composition is. TEM would enable high-resolution imaging of the material on a small scale, which would show the presence of any clusters, and EDS would provide elemental analysis of these clusters. Since a confident identification of the blue material was not achieved, some alternate hypotheses are discussed below.

4.5.2 Alternate Hypothesis 1: Selenium radical

One alternate hypothesis to the cluster discussed above is the presence of a selenium radical nested in a cobalt-triphenylphosphine complex. Previous research on selenium radicals in a aryl-containing complex has shown that they are blue and paramagnetic, which matches the blue material in this work. [6] Additionally, the UV-Vis data on the selenium radical (Figure 4.15) roughly matches what is observed in the blue material. The UV-Vis spectrum shows a broad absorbance

from 400 nm to 800-nm that seems to be comprised of multiple peaks centered around 600 nm, which is the same as the blue material. For the presence of a selenium radical to be consistent with the MALDI-MS data, it would need to be part of a larger complex similar in size to the one discussed above. Additionally, the presence of a selenium radical would not have a large impact on the FTIR, and the PDF analysis would still contain the low r peaks observed in the blue material, therefore, this is a plausible hypothesis.

This hypothesis does seem less likely than the cluster due to the difficulty forming a selenium radical and the control reaction without selenium. Based on the reaction between cobalt and triphenylphosphine, the blue material is unlikely to be a selenium radical since a blue color was still observed without selenium present (Figure 4.11). Additionally, the difficulty with selenium binding to the phenyl ring makes this hypothesis less likely. However, more data needs to be collected to confidently disprove the presence of a selenium radical. Electron Paramagnetic Resonance (EPR) spectroscopy would be a valuable experiment to demonstrate the presence of a selenium radical and can be completed on a powder sample. EPR data could be compared to the data for the selenium radical and should show multiple peaks indicative of a selenium radical if there is one present. Without this additional data, the presence of a selenium radical cannot be fully ruled out.

4.5.3 Alternate Hypothesis 2: Cobalt Selenide

Due to the appearance of cobalt selenide in the X-ray diffraction and PDF analysis, the possibility of the blue material being cobalt selenide in triphenylphosphine remains. This is a less likely option when considering the rest of the data. Cobalt selenide absorbs most of the visible spectrum and appears black even when in nanoparticle form. [53] Additionally, the FTIR shows shifts in the triphenylphosphine peaks which indicates the presence of a bond triphenylphosphine that would not exist in cobalt selenide. Therefore, despite the presence of cobalt selenide in diffraction data, the material is not likely just cobalt selenide.

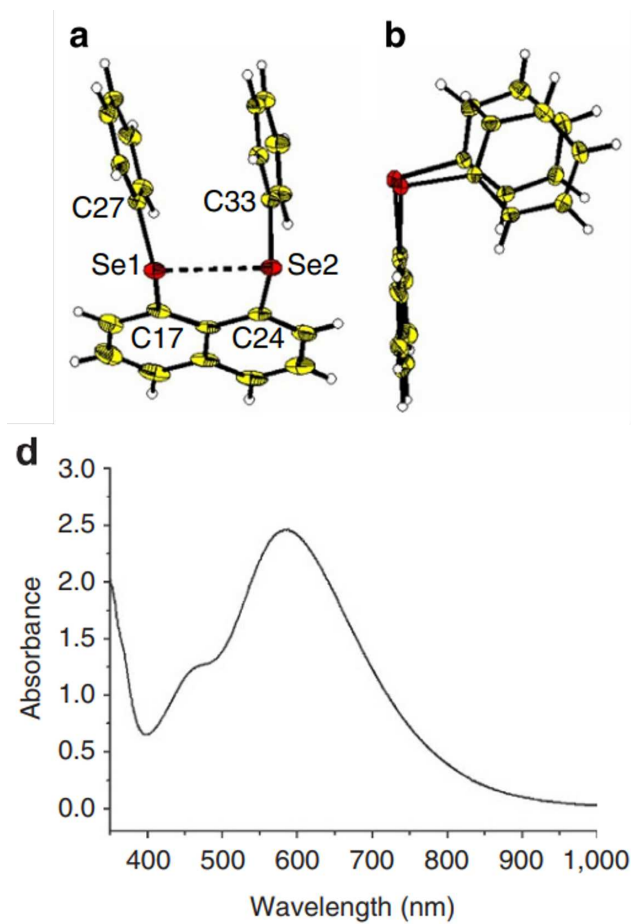


Figure 4.15: Structure (top) and absorbance spectrum (bottom) of the selenium radical complex. Figures from Zhang *et al.*. [6]

4.6 Conclusions

This study provides evidence for a novel cobalt-selenium-triphenylphosphine cluster. MALDI-MS, PDF analysis, FTIR, and solubility experiments support the hypothesis that this material is a cluster of approximately the size of $\text{Co}_{12}\text{Se}_{16}(\text{PPh}_3)_{10}$. Further experimentation including TEM and elemental analysis would need to be completed to confirm that the material is a cluster and determine the approximate size. Based on the hypothesis that the material is a cluster, this work demonstrates a non-standard synthetic approach to metal chalcogenide clusters. Additionally, this cluster can be explored for use in superatoms and the synthesis expanded to other metal chalcogenide clusters. This also demonstrates the utility of molten organic compounds in discovering new materials.

Chapter 5

Preliminary Results Exploring Other Organic

Fluxes⁴

5.1 Overview

Synthesis by design is essential for materials discovery; however, controlling reactivity can be difficult in the solid state. Expanding the number of selective and tunable reaction schemes available for solid-state synthesis would aid materials discovery. This preliminary work exploring the tunability of organic flux reactions demonstrates their ability for targeted synthesis. This proof of concept introduces the prospect of using the tunability of organic compounds to control reactivity in the solid-state through the use of organic fluxes.

5.2 Introduction

The ability for targeted synthesis is necessary for materials discovery in any field of chemistry. However, in solid-state chemistry, synthesis by design has been challenging to achieve. [8] There are limited tools for controlling reactivity in the solid-state and tuning reactions to target different products can be difficult. Expanding these synthetic tools would aid in the discovery of solid-state materials.

Triphenylphosphine fluxes open the door for studies involving other organic fluxes in solid-state synthesis. Introducing an organic material into solid-state synthesis increases the tunability of solid-state reactions. Preliminary results show that different fluxes selectively target different iron selenide phases. As discussed previously, in the case of a triphenylphosphine flux, iron selenide is selectively formed. [15] This selectivity is owing to the Lewis basicity of the triphenylphosphine enabling it to react with the selenium and change the convex hull such that iron selenide is the

⁴This chapter describes initial work that could be the start of a future publication. Experiments and writing were completed by M. Jewels Fallon with guidance from James R. Neilson.

only remaining phase. Since the selectivity of these reactions is based on the Lewis basicity of triphenylphosphine, this introduces the question of how a Lewis acid impacts the reaction. Boric acid is a good system for exploring this question as it is generally considered a Lewis acid with a melting point around 170 °C. Preliminary reactions with boric acid show the potential for targeting different materials by changing the flux.

5.3 Experimental

Iron powder (NOAH Technologies Corporation, 99.9%) was purified by heating it for 16 hours at 980 °C in a fused SiO₂ ampoule sealed under vacuum as explained previously. [15] Iron selenide was synthesized in a triphenylphosphine flux as described previously. [15] Purified iron, selenium powder (Sigma Aldrich, 99.5%), and boric acid (Alfa Aesar, 99.5%) in a 1:1:1 mole ratio were sealed in a fused SiO₂ ampoule (10 mm ID/12 mm OD) under vacuum ($p \leq 15$ mTorr). The ampoule was heated at a rate of 10 °C/min to 200 °C and held there for 24 h. The ampoule was then allowed to cool in the furnace to room temperature.

To prepare the sample for powder X-ray diffraction (PXRD), the flux was removed. A metal spatula was used to mechanically scrape away most of the flux and the rest was rinsed away by stirring the product in two approximately 10 mL aliquots of benzene (EMD Milipore, 99%) per 500 mg reaction. The remaining product was ground until homogeneous (approximately 2-3 min) with a mortar and pestle. The powder sample was then placed on a zero-diffraction Si wafer and PXRD data was collected on a Bruker D8 Discover diffractometer with CuK α radiation and a Lynxeye XE-T position-sensitive detector. Phase identification was completed using EVA V6 (Bruker) and Rietveld refinements were completed using TOPAS v6 (Bruker).

5.4 Results and discussion

While the triphenylphosphine flux reaction forms β -FeSe, the reaction with a boric acid flux selectively forms FeSe₂ (Figure 5.1). These reactions demonstrate how different fluxes are selective for different materials as Boric acid has the opposite reactivity to triphenylphosphine. Triph-

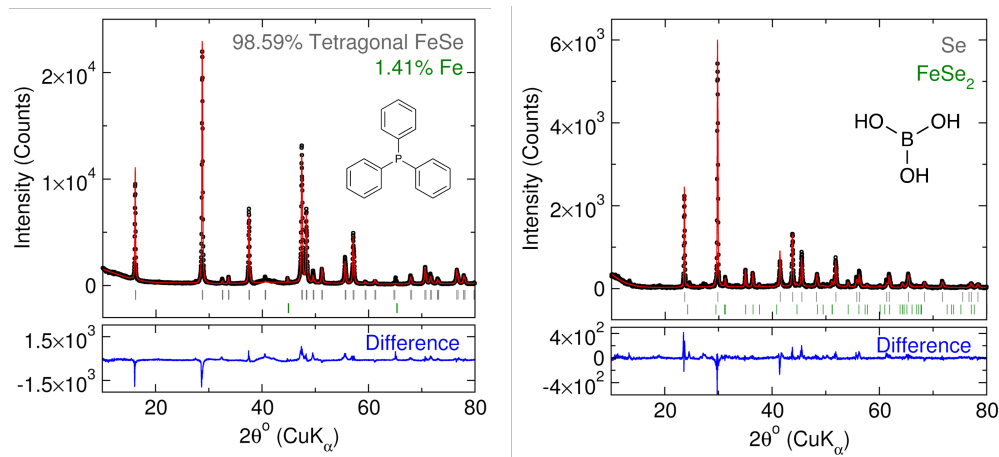


Figure 5.1: PXRD of the products of the iron selenide reactions completed with triphenylphosphine (left) and boric acid (right). Rietveld refinements are shown in red with tick marks below indicating the peak locations for each phase. The phases used for the refinement are in the upper right with mole percents. The difference curve is below each graph in blue.

enylphosphine reacts with selenium and changes the convex hull such that iron selenide is the only remaining phase. More analysis, such as *in situ* XRD, would be necessary to confirm the mechanism of reactivity for boric acid. However, based on the reaction products, boric acid seems to interact with the iron to change the convex hull in the opposite way of triphenylphosphine as shown in Figure 5.2. A boric acid-iron adduct analogous to the triphenylphosphine selenide adduct does not, to our knowledge, exist in the literature. Therefore, it is more likely that a complex containing iron, boron, and oxygen forms, changing the reactivity of the iron. This causes FeSe_2 to be the only phase remaining on the convex hull. Since it is the only stable phase, the boric acid flux reaction is selective for FeSe_2 . This promising initial reaction demonstrates the potential to tune reactivity in organic flux synthesis by changing the Lewis basicity and acidity of the flux.

5.5 Conclusion

This preliminary work demonstrates the utility of organic fluxes for synthesis by design and opens the door for exploring other fluxes for targeted synthesis in the solid-state. This provides a proof of concept for the prospect of changing the organic flux to target different materials. The tunability of organic compounds means that this reaction scheme is also highly tunable and thus

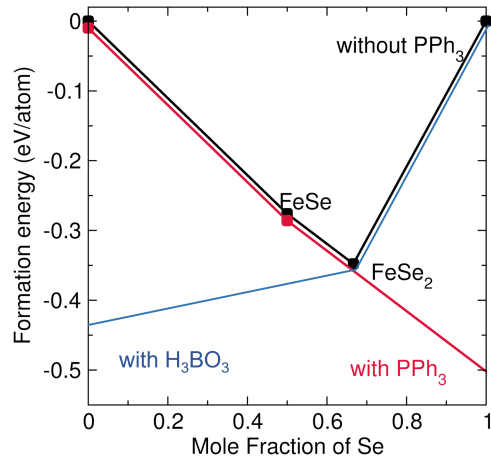


Figure 5.2: Formation energies ($T = 0$ K, DFT) [1] of computed and stable Fe–Se species that form the convex hull without triphenylphosphine (black line). Extrapolated effective chemical potential of selenium in the presence of excess triphenylphosphine (red) and boric acid (blue).

provides a new tool for synthesis by design in the solid state. Through expanding the known synthetic tools, organic fluxes can aid in solid-state materials discovery.

Chapter 6

Conclusions and Future Directions

6.1 Summary of organic flux reactions

This thesis demonstrates the utility of triphenylphosphine flux reactions to synthesize known materials and enable materials discovery. Beginning with iron selenide as a proof of concept for using triphenylphosphine as a reactive flux to target materials that are stable at low temperatures. The traditional synthesis of the low-temperature phase of iron selenide requires 12 days, specialized equipment to reach the high temperatures, and a multi-step reaction. [2] Using a triphenylphosphine flux simplified this to a single-step, 5-day reaction that occurs at much lower temperatures. [15] Triphenylphosphine initially reacts with the selenium to form the triphenylphosphine selenide adduct. This adduct changes the convex hull such that the desired iron selenide compound is the only stable phase remaining. Then, when the adduct reacts with the iron, it selectively forms that desired iron selenide phase. This proof of concept shows the ability of triphenylphosphine fluxes to simplify the synthesis of known materials that are only stable at low temperatures.

Knowing the guiding principals behind the triphenylphosphine flux reaction allows for the design of future syntheses using this reaction. To determine these principals, this reaction scheme was used to target a range of other metal chalcogenide binary systems. Based on the phase diagrams for these systems, the product for each reaction can be predicted. Most reactions were selective for the product predicted based on thermodynamics, however some reactions were not. Based on a combined thermodynamic and kinetic approach, principal component analysis, and a machine learning algorithm, the minimum chemical potential change, metal density, adduct bond dissociation energy, metal electronegativity, metal melting point, chalcogen melting point, chalcogen atomic number, and chalcogen ionization energy were found to be useful predictors for selectivity. Based on this, reactions that involve metals that are more reactive owing to their lower melting

point and lower density are more likely to be able to be synthesized using a triphenylphosphine flux. Additionally, changing the chalcogen down the periodic table lowers the bond dissociation energy which means a given reaction is more likely to be selective for the expected product. This work shows the broader applicability triphenylphosphine flux reactions in synthesizing binary metal chalcogenides, providing a tool for predicting the outcome of future reactions.

The utility of triphenylphosphine fluxes in materials discovery has also been demonstrated through the synthesis of the blue complex discussed in the fourth chapter. New solid-state materials are necessary to improve modern technologies such as solar cells, batteries, and hard drives. The more synthetic tools available to solid-state chemists, the more potential to discover new materials. The discovery of the blue material shows the potential for materials discovery using organic flux reactions. Additionally, the material is likely a cluster which would represent the first, to our knowledge, example of a metal chalcogenide cluster synthesized using an organic flux. Metal chalcogenide clusters have widespread applications in ranging from catalysis to energy storage. These widespread applications often stem from their ability to be organized into hierarchical structures which offer more tunability. Discovering new clusters enables progress in a vast array of modern technologies. Although a positive identification was not achieved for the blue material, it is evident that this material has not been made before. The discovery of this blue material demonstrates that organic fluxes can be used to synthesize new metal chalcogenide clusters and enable materials discovery.

Preliminary experiments exploring other organic fluxes have demonstrated their broader utility in targeted synthesis. Boric acid impacted the convex hull in the opposite way of triphenylphosphine allowing for FeSe_2 to be targeted as opposed to FeSe . This reaction shows the potential for synthesis by design through changing the flux in a given reaction and expands the number of materials able to be targeted using organic fluxes.

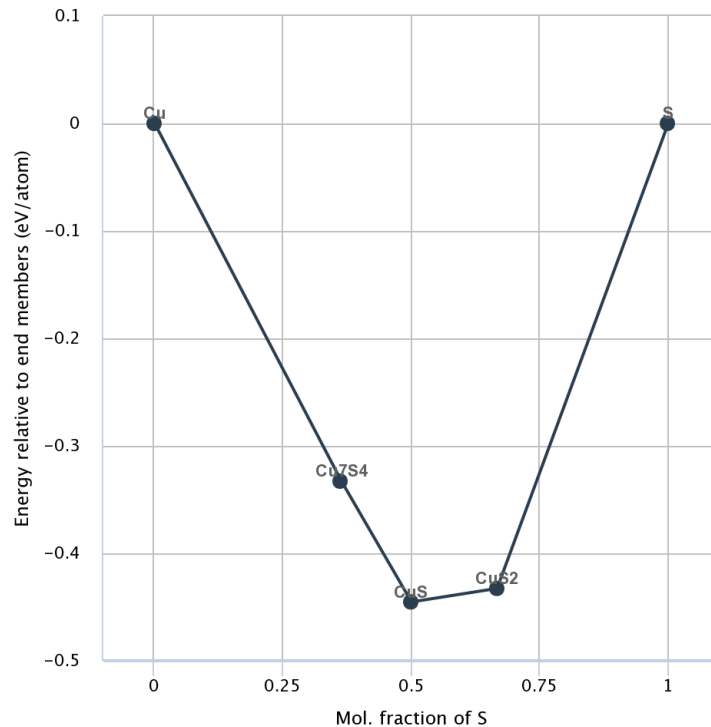


Figure 6.1: Formation energies ($T = 0$ K, DFT) [1] of computed and stable Cu–S species that form the convex hull.

6.2 Future directions for organic fluxes

The preliminary work exploring other fluxes prompts further questions regarding how to control product formation using organic fluxes. The prospect of using a mixture of organic compounds as a flux to target materials that are not the most metal-rich or chalcogen-rich phases on the convex hull is possible. For example, in the copper-sulfur system there are three phases on the convex hull (Figure 6.1). Based on the current knowledge of organic flux reactions, triphenylphosphine should selectively form Cu_7S_4 and boric acid should selectively form CuS_2 regardless of the initial ratio of reactants. However, CuS is also a stable phase on the convex hull. This leads to the question of whether a different flux or mixture of organic compounds as a flux could be used to selectively target CuS . Synthesis by design is difficult in solid-state chemistry and introducing organic compounds, which allow tunable reactivity, promises the idea of synthesis by design.

Along with exploring other fluxes, attempting to target other materials is also intriguing. Specifically, applying this synthesis to ternary systems and targeting new materials using this technique

is intriguing. Thus far, primarily binary metal chalcogenides have been formed. It seems likely that if organic fluxes can selectively target metal chalcogenide binaries, they can be applied to ternary chalcogenides with multiple metals. As ternary materials are also often challenging to make, finding new synthetic pathways to target these materials would be helpful. Additionally, the formation of the blue material discussed in the fourth chapter shows that this synthesis can be expanded to form other clusters or hybrid materials. Exploring the synthesis of more complicated materials and attempting to target new materials is a promising direction for organic flux research.

Overall, this work provides a promising new synthetic technique for solid-state materials. Synthesis by design is difficult with the limited library of tools available in solid-state chemistry. [8] Finding new techniques for targeted synthesis and understanding the guiding principals behind these techniques is therefore essential for advancing solid-state materials. The more synthetic tools and greater understanding available surrounding how these tools work, the easier it is to design a synthesis to target a specific material. With solid-state materials having such a huge impact on our society, advancing modern technologies hinges on our abilities to make and discover solid-state materials.

Bibliography

- [1] Anubhav Jain, Shyue Ping Ong, Geoffroy Hautier, Wei Chen, William Davidson Richards, Stephen Dacek, Shreyas Cholia, Dan Gunter, David Skinner, Gerbrand Ceder, and Kristin a. Persson. The Materials Project: A Materials Genome Approach to Accelerating Materials Innovation. *Appl. Phys. Lett. Mater.*, 1(1):011002, 2013.
- [2] T. M. McQueen, Q. Huang, V. Ksenofontov, C. Felser, Q. Xu, H. Zandbergen, Y. S. Hor, J. Allred, A. J. Williams, D. Qu, J. Checkelsky, N. P. Ong, and R. J. Cava. Extreme Sensitivity of Superconductivity to Stoichiometry in $\text{Fe}_{1+\delta}\text{Se}$. *Phys. Rev. B*, 79(1):014522, 2009.
- [3] Guijun Yang and Soo-Jin Park. Conventional and microwave hydrothermal synthesis and application of functional materials: A review. *Materials (Basel, Switzerland)*, 12:1177, 4 2019.
- [4] H.Jurgen Meyer. Solid State Metathesis Reactions as a Conceptual Tool in the Synthesis of New Materials. *Dalt. Trans.*, 39(26):5973–5982, 2010.
- [5] Anouck M. Champsaur, Taylor J Hochuli, Daniel W Paley, Colin Nuckolls, and Michael L Steigerwald. Superatom fusion and the nature of quantum confinement. *Nano Letters*, 18:4564–4569, 7 2018. doi: 10.1021/acs.nanolett.8b01824.
- [6] Senwang Zhang, Xingyong Wang, Yuanting Su, Yunfan Qiu, Zaichao Zhang, and Xinping Wang. Isolation and reversible dimerization of a selenium–selenium three-electron -bond. *Nature Communications*, 5:4127, 2014.
- [7] Laszlo Kurti and Barbara Czako. *Strategic Applications of Named Reactions in Organic Synthesis*. Academic Press Inc., 1 edition, 2005.
- [8] Andreas Stein, Steven W. Keller, and Thomas E. Mallouk. Turning Down the Heat: Design and Mechanism in Solid-State Synthesis. *Science*, 259(5101):1558–1564, 1993.

- [9] Georg Brauer. *Handbook of Preparative Inorganic Chemistry*. Academic Press Inc., 2 edition, 1963.
- [10] Joshua T. Greenfield, Saeed Kamali, Kathleen Lee, and Kirill Kovnir. A Solution for Solution-Produced β -FeSe: Elucidating and Overcoming Factors that Prevent Superconductivity. *Chem. Mater.*, 27(2):588–596, 2015.
- [11] M W Ma, D N Yuan, Y Wu, X L Dong, and F Zhou. Crystal growth of iron-based superconductor fese_{0.94} by kcl flux method. *Physica C: Superconductivity and its Applications*, 506:154–157, 2014.
- [12] Torsten Wölpl and Wolfgang Jeitschko. Crystal structures of vsn₂, nbsn₂ and crsn₂ with mg₂cu-type structure and nbsnsb with cual₂-type structure. *Journal of Alloys and Compounds*, 210:185–190, 1994.
- [13] Mercuri G. Kanatzidis, Rainer Pottgen, and Wolfgang Jeitschko. The Metal Flux: A Preparative Tool for the Exploration of Intermetallic Compounds. *Angew. Chem. Int. Ed.*, 44(43):6996–7023, 2005.
- [14] Andrew J. Martinolich, Robert F. Higgins, Matthew P. Shores, and James R. Neilson. Lewis Base Mediated Polymorph Selectivity of Pyrite CuSe₂ through Atom Transfer in Solid-State Metathesis. *Chem. of Mater.*, 28:1854–1860, 2016.
- [15] M. Jewels Fallon, Andrew J. Martinolich, Annalise E. Maughan, Leighanne C. Gallington, and James R. Neilson. Low-Temperature Synthesis of Superconducting Iron Selenide Using a Triphenylphosphine Flux. *Dalton Transactions*, 48(43):16298–16303, 2019.
- [16] T. A. Bither, R. J. Bouchard, W. H. Cloud, P. C. Dokohue, and W. J. Siemons. Transition Metal Pyrite Dichalcogenides. High-pressure Synthesis and Correlation of Properties. *Inorg. Chem.*, 59(1959):2208–2220, 1968.

- [17] S. B. Zhang, Y. P. Sun, X. D. Zhu, X. B. Zhu, B. S. Wang, G. Li, H. C. Lei, X. Luo, Z. R. Yang, W. H. Song, and J. M. Dai. Crystal Growth and Superconductivity of FeSe_x. *Supercond. Sci. Technol.*, 22(1):0–4, 2009.
- [18] T. Purnima A. Ruberu, Haley R. Albright, Brandon Callis, Brittney Ward, Joana Cisneros, Hua-jun Fan, and Javier Vela. Molecular Control of the Nanoscale: Effect of Phosphine - Chalcogenide Reactivity on CdS - CdSe Nanocrystal Composition and Morphology. *ACS Nano*, 6(6):5348–5359, 2012.
- [19] H. Okamoto. The FeSe System. *J. Phase Equilib.*, 12(3):383–389, jun 1991.
- [20] Fong-Chi Hsu, Jiu-Yong Luo, Kuo-Wei Yeh, Ta-Kun Chen, Tzu-Wen Huang, Phillip M. Wu, Yong-Chi Lee, Yi-Lin Huang, Yan-Yi Chu, Der-Chung Yan, and Maw-Kuen Wu. Superconductivity in the PbO-Type Structure α -FeSe. *Proc. Natl. Acad. Sci.*, 105(38):14262–14264, 2008.
- [21] F. Nitsche, T. Goltz, H.-H. Klauss, A. Isaeva, U. Muller, W. Schnelle, P. Simon, Th. Doert, and M. Ruck. Room-Temperature Synthesis, Hydrothermal Recrystallization, and Properties of Metastable Stoichiometric FeSe. *Inorg. Chem.*, 51:7370–7376, 2012.
- [22] Peter J. Chupas, Karena W. Chapman, Charles Kurtz, Jonathan C. Hanson, Peter L. Lee, and Clare P. Grey. A Versatile Sample-Environment Cell for Non-Ambient X-ray Scattering Experiments. *J. of Appl. Crystallogr.*, 41(4):822–824, 2008.
- [23] Brian H. Toby and Robert B. Von Dreele. GSAS-II: the Genesis of a Modern Open-Source All Purpose Crystallography Software Package. *J. Appl. Crystallogr.*, 46(2):544–549, Apr 2013.
- [24] C L Farrow, P Juhas, J W Liu, D Bryndin, E S Božin, J Bloch, Th Proffen, and S J L Billinge. PDFfit2 and PDFgui: Computer programs for studying nanostructure in crystals. *J. Phys.: Condens. Matter*, 19(33):335219, jul 2007.

- [25] Alexandra Navrotsky. Energetic Clues to Pathways to Biomineralization: Precursors, Clusters, and Nanoparticles. *Proc. Natl. Acad. Sci.*, 101(33):12096–12101, 2004.
- [26] Joseph Peterson, James TenCate, Thomas Proffen, Timothy Darling, Heinz Nakotte, and Katharine Page. Quantifying Amorphous and Crystalline Phase Content with the Atomic Pair Distribution Function. *J. Appl. Crystallogr.*, 46(2):332–336, 2013.
- [27] Gisbert Grossmann, Marek J. Potrzebowski, Ulrich Fleischer, Kerstin Krüger, Olga L. Malkina, and Włodzimierz Ciesielski. Anisotropy of Chemical Shift and J coupling for P-31 and Se-77 in Trimethyl and Triphenyl Phosphine Selenides. *Solid State Nucl. Mag. Res.*, 13(1-2):71–85, 1998.
- [28] Mercuri G. Kanatzidis. Molten Alkali-Metal Polychalcogenides as Reagents and Solvents for the Synthesis of New Chalcogenide Materials. *Chem. Mater.*, 2(4):353–363, 1990.
- [29] Shyue Ping Ong, William Davidson Richards, Anubhav Jain, Geoffroy Hautier, Michael Kocher, Shreyas Cholia, Dan Gunter, Vincent L. Chevrier, Kristin A. Persson, and Gerbrand Ceder. Python materials genomics (pymatgen): A robust, open-source python library for materials analysis. *Computational Materials Science*, 68:314–319, 2013.
- [30] Christopher J. Bartel, Samantha L. Millican, Ann M. Deml, John R. Rumpitz, William Tumas, Alan W. Weimer, Stephan Lany, Vladan Stevanović, Charles B. Musgrave, and Aaron M. Holder. Physical descriptor for the Gibbs energy of inorganic crystalline solids and temperature-dependent materials chemistry. *Nature Communications*, 9(1), 2018.
- [31] Michael L. Waskom. seaborn: statistical data visualization. *Journal of Open Source Software*, 6(60):3021, 2021.
- [32] F. Pedregosa, G. Varoquaux, A. Gramfort, V. Michel, B. Thirion, O. Grisel, M. Blondel, P. Prettenhofer, R. Weiss, V. Dubourg, J. Vanderplas, A. Passos, D. Cournapeau, M. Brucher, M. Perrot, and E. Duchesnay. Scikit-learn: Machine learning in Python. *Journal of Machine Learning Research*, 12:2825–2830, 2011.

- [33] Xavier Roy, Chul-Ho Lee, Andrew C. Crowther, Christine L. Schenck, Tiglet Besara, Roger A. Lalancette, Theo Siegrist, Peter W. Stephens, Louis E. Brus, Philip Kim, Michael L. Steigerwald, and Colin Nuckolls. Nanoscale atoms in solid-state chemistry. *Science*, 341:157–160, 7 2013.
- [34] Alexander P Aydt, Boyu Qie, Andrew Pinkard, Long Yang, Qian Cheng, Simon J L Billinge, Yuan Yang, and Xavier Roy. Microporous battery electrodes from molecular cluster precursors. *ACS Applied Materials Interfaces*, 11:11292–11297, 3 2019. doi: 10.1021/ac-sami.8b18149.
- [35] Shelley A Claridge, A. W Castleman, Shiv N Khanna, Christopher B Murray, Ayusman Sen, and Paul S Weiss. Cluster-assembled materials. *ACS nano*, 3(2):244–255, 2009.
- [36] Ari Turkiewicz, Daniel W Paley, Tiglet Besara, Giselle Elbaz, Andrew Pinkard, Theo Siegrist, and Xavier Roy. Assembling hierarchical cluster solids with atomic precision. *Journal of the American Chemical Society*, 136(45):15873–15876, 2014.
- [37] T. P Martin, T Bergmann, H Goehlich, and T Lange. Shell structure of clusters. *Journal of physical chemistry (1952)*, 95(17):6421–6429, 1991.
- [38] Hannu Häkkinen. Electronic shell structures in bare and protected metal nanoclusters. *Advances in physics: X*, 1(3):467–491, 2016.
- [39] S.N Khanna and P Jena. Designing ionic solids from metallic clusters. *Chemical physics letters*, 219(5):479–483, 1994.
- [40] Puru Jena. Beyond the periodic table of elements: The role of superatoms. *The journal of physical chemistry letters*, 4(9):1432–1442, 2013.
- [41] Vikas Chauhan and Shiv N Khanna. Strong effect of organic ligands on the electronic structure of metal-chalcogenide clusters. *The journal of physical chemistry. A, Molecules, spectroscopy, kinetics, environment, general theory*, 122(28):6014–6020, 2018.

- [42] Robin J H Clark, Colin D Flint, Andrew J Hempleman, and * Christopher. and raman spectra of triphenylphosphine, triphenylarsine, triphenylstibine, and dibenzylsulphide, 1987.
- [43] Amala Dass, Anthony Stevenson, George R Dubay, Joseph B Tracy, and Royce W Murray. Nanoparticle maldi-tof mass spectrometry without fragmentation: Au₂₅(sch₂ch₂ph)₁₈ and mixed monolayer au₂₅(sch₂ch₂ph)_(18-x)(l)_(x). *Journal of the American Chemical Society*, 130(18):5940–5946, 2008.
- [44] Prasenjit Maity, Hironori Tsunoyama, Miho Yamauchi, Songhai Xie, and Tatsuya Tsukuda. Organogold clusters protected by phenylacetylene. *Journal of the American Chemical Society*, 133(50):20123–20125, 2011.
- [45] Anindya Ganguly, Indranath Chakraborty, Thumu Udayabhaskararao, and Thalappil Pradeep. A copper cluster protected with phenylethanethiol. *Journal of nanoparticle research : an interdisciplinary forum for nanoscale science and technology*, 15(4):1–, 2013.
- [46] Yizhong Lu and Wei Chen. Application of mass spectrometry in the synthesis and characterization of metal nanoclusters. *Analytical chemistry (Washington)*, 87(21):10659–10667, 2015.
- [47] Mikhail Agrachev, Sabrina Antonello, Tiziano Dainese, Marco Ruzzi, Alfonso Zoleo, Edoardo Apra, Niranjana Govind, Alessandro Fortunelli, Luca Sementa, and Flavio Maran. Magnetic ordering in gold nanoclusters. *ACS omega*, 2(6):2607–2617, 2017.
- [48] Haru Hirai, Shun Ito, Shinjiro Takano, Kiichirou Koyasu, and Tatsuya Tsukuda. Ligand-protected gold/silver superatoms: current status and emerging trends. *Chemical science (Cambridge)*, 11(45):12233–12248, 2020.
- [49] Andrew W Cook and Trevor W Hayton. Case studies in nanocluster synthesis and characterization: Challenges and opportunities. *Accounts of chemical research*, 51(10):2456–2464, 2018.

- [50] By D H Whiffen. Whiffen : Vibrational frequencies and thermodynamic 273. vibrational frequencies and thermodynamic properties of fluoro-, chloro-, bromo-, and iodo-benzene.
- [51] Dieter Fenske, Johannes Ohmer, Johannes Hachgenei, and Kurt Merzweiler. New transition metal clusters with ligands from main groups five and six. *Angewandte Chemie International Edition in English*, 27:1277–1296, 10 1988.
- [52] Olaf Fuhr, Stefanie Dehnen, and Dieter Fenske. Chalcogenide clusters of copper and silver from silylated chalcogenide sources. *Chemical Society reviews*, 42(4):1871–1906, 2013.
- [53] P. K. Khanna and V. V. Dhapte. One-pot synthesis of cobalt selenide nanoparticles. *International Journal of Green Nanotechnology*, 4:425–429, 10 2012.
- [54] R. Krishnan, J. S. Binkley, R. Seeger, and J. A. Pople. Self-consistent molecular orbital methods. xx. a basis set for correlated wave functions. *The Journal of chemical physics*, 72(1):650–654, 1980.
- [55] Jianmin Tao, John P Perdew, Viktor N Staroverov, and Gustavo E Scuseria. Climbing the density functional ladder: nonempirical meta-generalized gradient approximation designed for molecules and solids. *Physical review letters*, 91(14):146401–146401, 2003.
- [56] M. J. Frisch, G. W. Trucks, H. B. Schlegel, G. E. Scuseria, M. A. Robb, J. R. Cheeseman, G. Scalmani, V. Barone, G. A. Petersson, H. Nakatsuji, X. Li, M. Caricato, A. V. Marenich, J. Bloino, B. G. Janesko, R. Gomperts, B. Mennucci, H. P. Hratchian, J. V. Ortiz, A. F. Izmaylov, J. L. Sonnenberg, D. Williams-Young, F. Ding, F. Lipparini, F. Egidi, J. Goings, B. Peng, A. Petrone, T. Henderson, D. Ranasinghe, V. G. Zakrzewski, J. Gao, N. Rega, G. Zheng, W. Liang, M. Hada, M. Ehara, K. Toyota, R. Fukuda, J. Hasegawa, M. Ishida, T. Nakajima, Y. Honda, O. Kitao, H. Nakai, T. Vreven, K. Throssell, J. A. Montgomery, Jr., J. E. Peralta, F. Ogliaro, M. J. Bearpark, J. J. Heyd, E. N. Brothers, K. N. Kudin, V. N. Staroverov, T. A. Keith, R. Kobayashi, J. Normand, K. Raghavachari, A. P. Rendell, J. C. Burant, S. S. Iyengar, J. Tomasi, M. Cossi, J. M. Millam, M. Klene, C. Adamo, R. Cammi,

- J. W. Ochterski, R. L. Martin, K. Morokuma, O. Farkas, J. B. Foresman, and D. J. Fox. Gaussian~16 Revision C.01, 2016. Gaussian Inc. Wallingford CT.
- [57] Willard R. Wadt and P. Jeffrey Hay. Ab initio effective core potentials for molecular calculations. potentials for main group elements na to bi. *The Journal of chemical physics*, 82(1):284–298, 1985.
- [58] Christopher L. Rom, M. Jewels Fallon, Allison Wustrow, Amy L. Prieto, and James R. Neilson. Bulk synthesis, structure, and electronic properties of magnesium zirconium nitride solid solutions. *Chemistry of Materials*, 33(13):5345–5354, 2021.
- [59] Paul K. Todd, M. Jewels Fallon, James R. Neilson, and Andriy Zakutayev. Two-step solid-state synthesis of ternary nitride materials. *ACS Materials Letters*, 3(12):1677–1683, 2021.
- [60] Gengtao Fu, Zhiming Cui, Yifan Chen, Lin Xu, Yawen Tang, and John B. Goodenough. Hierarchically mesoporous nickel-iron nitride as a cost-efficient and highly durable electrocatalyst for zn-air battery. *Nano Energy*, 39:77–85, 2017.
- [61] Melissa E Kreider, Alessandro Gallo, Seoin Back, Yunzhi Liu, Samira Siahrostami, Dennis Nordlund, Robert Sinclair, Jens K Nørskov, Laurie A King, and Thomas F Jaramillo. Precious metal-free nickel nitride catalyst for the oxygen reduction reaction. *ACS applied materials interfaces*, 11(30):26863–26871, 2019.
- [62] D.H. Gregory, M.G. Barker, P.P. Edwards, M. Slaski, and D.J. Siddons. Synthesis, structure, and magnetic properties of the new ternary nitride BaHfN_2 and of the $\text{BaHf}_{1-x}\text{Zr}_x\text{N}_2$ solid solution. *Journal of Solid State Chemistry*, 137(1):62–70, 1998.
- [63] R. Verrelli, M. E. Arroyo-de Dompablo, D. Tchitchekova, A. P. Black, C. Frontera, A. Fuertes, and M. R. Palacin. On the viability of mg extraction in MgMnO_2 : a combined experimental and theoretical approach. *Phys. Chem. Chem. Phys.*, 19:26435–26441, 2017.

- [64] Roberta Verrelli, Ashley Philip Black, Carlos Frontera, Judith Oro-Sole, Maria Elena Arroyo-de Dompablo, Amparo Fuertes, and M. Rosa Palacin. On the study of ca and mg deintercalation from ternary tantalum nitrides. *ACS omega*, 4(5):8943–8952, 2019.
- [65] Ann L Greenaway, Celeste L Melamed, M. Brooks Tellekamp, Rachel Woods-Robinson, Eric S Toberer, James R Neilson, and Adele C Tamboli. Ternary nitride materials: Fundamentals and emerging device applications. *Annual review of materials research*, 51(1):591–618, 2021.

Appendix A

Supplemental Information: Low-Temperature

Synthesis of Superconducting Iron Selenide Using a Triphenylphosphine Flux

Reactions were completed with varying mole ratios of FeSe:PPh₃ (1:0.5, 1:1, 1:1.5, and 1:2), reaction temperatures (150, 200, 250, 275, 325, 350, 375, and 400 °C), reaction times (16, 24, 72, 117, and 168 h), and cooling times (water quench, air quench, 30 h, 45 h, 60 h).

Phase fractions calculated from *in situ* XRD (Figure A.2) do not take into account amorphous phases. Triphenylphosphine is also not included in this analysis as the peaks for this phase are barely observable due to the large X-ray scattering cross-section of iron. Additionally, spots observed in the diffraction pattern before data reduction indicate iron single crystal formation that could impact the phase fractions. Triphenylphosphine selenide is observed in the room temperature PDF indicating that ball milling initiated adduct formation which accounts for the excess iron compared to selenium observed in the diffraction at room temperature.

Laboratory *ex situ* PDF analysis of the reaction 8Fe + Se + PPh₃ (Figures A.3, A.4) was completed using HighScore Plus to reduce the data and PDFgui to model the data. Each of these PDF data sets were modeled with two iron phases along with the other phases present. The crystalline iron phase was modeled through refining lattice parameters, thermal parameters, correlated mo-

Table A.1: Phase fraction (mol%) determined through Rietveld analysis of PXRD patterns of products formed from reactions with varying fluxes.

	β -FeSe	α -FeSe	Fe ₃ Se ₄	FeSe ₂	Fe	Se
Triphenylamine	0.9		4.7	21.9	7.8	64.7
Eicosane	7.2	2.5	7.5	82.8		
No flux	46.3	6.1	39.4		8.2	

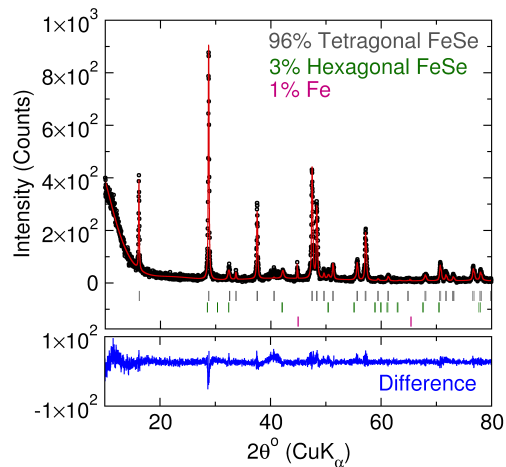


Figure A.1: Diffraction pattern of products from the reaction between PPh_3Se and Fe. Rietveld analysis is shown in red and difference curve in blue. The tick marks indicate peak locations for β -FeSe (grey), α -FeSe (green), and Fe (pink) and the phase fraction (mol%) is shown in the upper righthand corner.

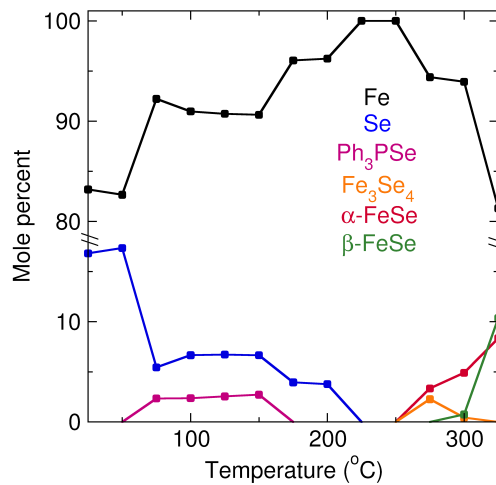


Figure A.2: Phase fraction (mol%) of each phase determined from Rietveld analysis of PXRD data collected *in situ* during the iron selenide reaction.

Table A.2: Inorganic reaction products across the ternary Fe-Se-PPh₃ phase space. Phase fraction (mol%) are written in parentheses.

Ratio Fe:Se:PPh ₃	Product 1	Product 2	Product 3	Product 4	Product 5	Product 6
3:1:6	β -FeSe (88)	Fe (12)				
1:3:6	β -FeSe (95)	α -FeSe (5)				
1:1:8	β -FeSe (98)	Fe (2)				
8:1:1	β -FeSe (61)	Fe (39)				
6:3:1	β -FeSe (93)	Fe (7)				
6:1:3	β -FeSe (71)	Fe (29)				
1:8:1	Se (93)	β -FeSe (4)	FeSe ₂ (3)			
3:6:1	Se (48)	FeSe ₂ (27)	β -FeSe (16)	Fe ₃ Se ₄ (7)	α -FeSe (2)	
1:6:3	Se (57)	FeSe ₂ (14)	Fe (18)	β -FeSe (6)	Fe ₃ Se ₄ (4)	α -FeSe (1)
4:2:4	β -FeSe (93)	Fe (7)				
2:4:4	β -FeSe (84)	α -FeSe (16)				
4:4:2	β -FeSe (93)	α -FeSe (7)				

Table A.3: Formation energies accessed from the Materials Project (Date: 5/16/2019). [1]

Compound	Formation energy (eV/atom)	Materials project ID
Fe	0	mp-13
FeSe	-0.276	mp-20311
FeSe ₂	-0.348	mp-760
Se	0	mp-570481

tion parameters, and the scale factor. The amorphous iron phase was modeled by duplicating the crystalline iron phase but with a spherical particle size cut-off which refined to 7 Å.

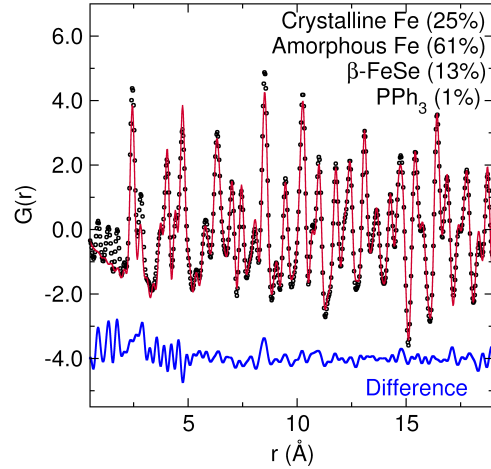


Figure A.3: *Ex situ* PDF analysis of of $8\text{Fe} + \text{Se} + \text{PPh}_3$ reaction product. The phase fractions (mol%) of the refined phases are included in the top right corner. The data are shown as black circles, the fit is the red line, and the difference is the blue line.

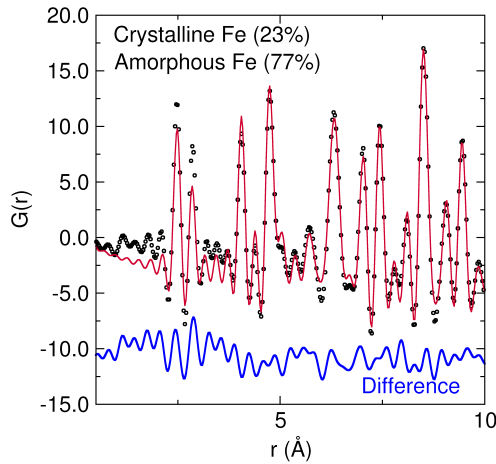


Figure A.4: *Ex situ* PDF analysis of the iron starting material. The phase fractions (mol%) of the refined phases are included in the top left corner. The data are shown as black circles, the fit is the red line, and the difference is the blue line.

Appendix B

Supplemental Information: The Reactivity of Triphenylphosphine Fluxes in the Synthesis of Metal Chalcogenides

A table of the reactants used and their information is provided in table B.1

The table of the features for each metal chalcogenide reaction that were used in the machine learning analysis is provided in table B.3. The product expected is the product that would be predicted based on the phase diagram. The formation energy and density of that product are from the Materials Project Database. [1] The bond dissociation energies were calculated using density functional theory. Reported geometry optimizations used the 6-311g(2d) basis set (except Te) [54], the TPSS functional [55], and the Gaussian 16 electronic structure package [56]. For Te the LANL basis [57], with 2 augmented d functions ($\zeta=0.433, 0.144$). Total energies (Hartree) and binding energies (kcal/mol) are collected in Table B.2. For all analyses involving principal component analysis (PCA) or machine learning algorithms, the "Did it work" column was converted to integer values.

Table B.1: List of the sources and purity of each reactant used.

Reactant	Source	Purity
Triphenylphosphine flakes	Alfa Aesar	99+
Selenium powder	Sigma Aldrich	99.5
Sulfur powder	NOAH Technologies Corporation	99.5
Tellurium broken ingot	Alfa Aesar	99.9
Iron powder	NOAH Technologies Corporation	99.9
Cobalt powder	NOAH Technologies Corporation	99.9
Manganese metal flakes	NOAH Technologies Corporation	99.99
Tin powder	TT Baker Chemical Co.	99.9
Lead shot	Alfa Aesar	97
Nickel powder	Aldrich Chem Co.	99
Gallium	Sigma Aldrich	99.99
Indium	Sigma Aldrich	99.9
Silver	Sigma Aldrich	99.9
Molybdenum	Alfa Aesar	99.95
Ruthenium	Alfa Aesar	99.99
Tantalum	Alfa Aesar	99.98

Table B.2: Energies of the chalcogen and chalcogen adducts from DFT calculations.

Compound	Total energies (Hartree)	Binding energies (kcal/mol)
S	-398.1	
Se	-2401.4	
Te	-8.0	
PPh ₃	-1036.6	
SPPh ₃	-1434.9	-78.6
SePPh ₃	-3438.1	-65.0
TePPh ₃	-1044.7	-41.2

Table B.3: Table of the chemical properties used to analyze the reactivity of these systems. Continued on following pages.

Reaction	Product expected	Purity with flux	Purity without flux	Purity difference	Hypothesis supported?	Formation energy (eV)
Fe-Se	FeSe	99	46	53	Yes	-0.2804
Fe-S	FeS	100	16	84	Yes	-0.8404
Fe-Te	FeTe ₂	100	100	0	unclear	-0.1768
Co-Se	Co ₉ Se ₈	9	0	9	Yes	-0.2759
Co-S	Co ₉ S ₈	100	13	87	Yes	-0.7809
Co-Te	CoTe ₂	86	75	11	Yes	-0.2034
Mn-Se	MnSe	62	60	2	No	-0.3676
Mn-S	MnS	86	57	29	Yes	-0.875
Mn-Te	MnTe	82	3	79	Yes	-0.0808
Ni-Te	mixture	mixture	mixture	NA	Yes	-0.1825
Sn-S	SnS	75	75	0	No	-0.7978
Pb-Se	PbSe	100	100	0	unclear	-0.5481
Pb-S	PbS	0	95	-95	No	-0.8561
Pb-Te	PbTe	80	83	-3	No	-0.4033
Ga-Te	GaTe	100	1	99	Yes	-0.3717
In-Te	mixture	mixture	mixture	NA	Yes	-0.2582
Ag-S	Ag	100	7	93	Yes	-0.2689
Ag-Se	Ag	0	0	0	No	-0.0689
Ag-Te	Ag ₂ Te	100	68	32	Yes	-0.0736
Mo-S	MoS ₂	0	0	0	No	-1.3652
Mo-Se	MoSe ₂	50	52	-2	No	-0.7251
Ru-Se	RuSe ₂	0	0	0	No	-0.4382
Ru-S	Ru	100	100	0	unclear	-0.9908
Ta-Se	mixture	unreacted	unreacted	NA	No	-0.4615
Ta-S	mixture	unreacted	unreacted	NA	No	-1.0118
Ta-Te	mixture	unreacted	TaTe ₄	NA	No	-0.2832

Table B.4: Table of the chemical properties used to analyze the reactivity of these systems. Continued from the previous page.

Reaction	Adduct bond dissociation energy (kJ/mol)	Metal density (g/cm ³)	Chalcogen density (g/cm ³)	Average density (g/cm ³)
Fe-Se	-271.4932646	7.874	4.819	6.3465
Fe-S	-328.4786533	7.874	1.96	4.917
Fe-Te	-172.0593758	7.874	6.24	7.057
Co-Se	-271.4932646	8.9	4.819	6.8595
Co-S	-328.4786533	8.9	1.96	5.43
Co-Te	-172.0593758	8.9	6.24	7.57
Mn-Se	-271.4932646	7.47	4.819	6.1445
Mn-S	-328.4786533	7.47	1.96	4.715
Mn-Te	-172.0593758	7.47	6.24	6.855
Ni-Te	-172.0593758	8.908	6.24	7.574
Sn-S	-328.4786533	7.31	1.96	4.635
Pb-Se	-271.4932646	11.34	4.819	8.0795
Pb-S	-328.4786533	11.34	1.96	6.65
Pb-Te	-172.0593758	11.34	6.24	8.79
Ga-Te	-172.0593758	5.904	6.24	6.072
In-Te	-172.0593758	7.31	6.24	6.775
Ag-S	-328.4786533	10.49	1.96	6.225
Ag-Se	-271.4932646	10.49	4.819	7.6545
Ag-Te	-172.0593758	10.49	6.24	8.365
Mo-S	-328.4786533	10.28	1.96	6.12
Mo-Se	-271.4932646	10.28	4.819	7.5495
Ru-Se	-271.4932646	12.37	4.819	8.5945
Ru-S	-328.4786533	12.37	1.96	7.165
Ta-Se	-271.4932646	16.65	4.819	10.7345
Ta-S	-328.4786533	16.65	1.96	9.305
Ta-Te	-172.0593758	16.65	6.24	11.445

Table B.5: Table of the chemical properties used to analyze the reactivity of these systems. Continued from the previous page.

Reaction	Product density (g/cm ³)	Metal electronegativity	Chalcogen electronegativity	Electronegativity difference
Fe-Se	5.71	1.83	2.55	0.72
Fe-S	4.84	1.83	2.58	0.75
Fe-Te	8.06	1.83	2.1	0.27
Co-Se	6.8	1.88	2.55	0.67
Co-S	5.34	1.88	2.58	0.7
Co-Te	7.94	1.88	2.1	0.22
Mn-Se	5.49	1.55	2.55	1
Mn-S	4.02	1.55	2.58	1.03
Mn-Te	6.75	1.55	2.1	0.55
Ni-Te	8.23	1.91	2.1	0.19
Sn-S	5.17	1.96	2.58	0.62
Pb-Se	8.26	2.33	2.55	0.22
Pb-S	6.66	2.33	2.58	0.25
Pb-Te	8.24	2.33	2.1	-0.23
Ga-Te	5.47	1.81	2.1	0.29
In-Te	6.33	1.78	2.1	0.32
Ag-S	8.79	1.93	2.58	0.65
Ag-Se	8.21	1.93	2.55	0.62
Ag-Te	8.42	1.93	2.1	0.17
Mo-S	5	2.16	2.58	0.42
Mo-Se	6.96	2.16	2.55	0.39
Ru-Se	8.23	2.2	2.55	0.35
Ru-S	6.21	2.2	2.58	0.38
Ta-Se	12.22	1.5	2.55	1.05
Ta-S	10.89	1.5	2.58	1.08
Ta-Te	10.22	1.5	2.1	0.6

Table B.6: Table of the chemical properties used to analyze the reactivity of these systems. Continued from the previous page.

Reaction	Metal melting point (°C)	Chalcogen melting point (°C)	Metal atomic number	Chalcogen atomic number
Fe-Se	1538	221	26	34
Fe-S	1538	115.21	26	16
Fe-Te	1538	449.51	26	52
Co-Se	1495	221	27	34
Co-S	1495	115.21	27	16
Co-Te	1495	449.51	27	52
Mn-Se	1246	221	25	34
Mn-S	1246	115.21	25	16
Mn-Te	1246	449.51	25	52
Ni-Te	1455	449.51	28	52
Sn-S	231.93	115.21	50	16
Pb-Se	327.46	221	82	34
Pb-S	327.46	115.21	82	16
Pb-Te	327.46	449.51	82	52
Ga-Te	29.76	449.51	31	52
In-Te	156.6	449.51	49	52
Ag-S	961.78	115.21	47	16
Ag-Se	961.78	221	47	34
Ag-Te	961.78	449.51	47	52
Mo-S	2623	115.21	42	16
Mo-Se	2623	221	42	34
Ru-Se	2334	221	44	34
Ru-S	2334	115.21	44	16
Ta-Se	3017	221	73	34
Ta-S	3017	115.21	73	16
Ta-Te	3017	449.51	73	52

Table B.7: Table of the chemical properties used to analyze the reactivity of these systems. Continued from the previous page.

Reaction	Metal ionization energy (kJ/mol)	Chalcogen ionization energy (kJ/mol)	Metal electron affinity (kJ/mol)	Chalcogen electron affinity (kJ/mol)
Fe-Se	762.5	941	15.7	195
Fe-S	762.5	999.6	15.7	200
Fe-Te	762.5	869.3	15.7	190.2
Co-Se	760.4	941	63.7	195
Co-S	760.4	999.6	63.7	200
Co-Te	760.4	869.3	63.7	190.2
Mn-Se	717.3	941	0	195
Mn-S	717.3	999.6	0	200
Mn-Te	717.3	869.3	0	190.2
Ni-Te	737.1	869.3	112	190.2
Sn-S	708.6	999.6	107.3	200
Pb-Se	715.6	941	35.1	195
Pb-S	715.6	999.6	35.1	200
Pb-Te	715.6	869.3	35.1	190.2
Ga-Te	578.8	869.3	28.9	190.2
In-Te	558.3	869.3	28.9	190.2
Ag-S	731	999.6	125.6	200
Ag-Se	731	941	125.6	195
Ag-Te	731	869.3	125.6	190.2
Mo-S	684.3	999.6	71.9	200
Mo-Se	684.3	941	71.9	195
Ru-Se	710.2	941	101.3	195
Ru-S	710.2	999.6	101.3	200
Ta-Se	761	941	31	195
Ta-S	761	999.6	31	200
Ta-Te	761	869.3	31	190.2

Table B.8: Table of the chemical properties used to analyze the reactivity of these systems. Continued from the previous page.

Reaction	Minimum chemical potential change (eV/atom)	Maximum chemical potential change (eV/atom)
Fe-Se	-0.4955	-0.5586
Fe-S	-1.1532	-1.6757
Fe-Te	0	-0.2613
Co-Se	-0.3423	-0.5856
Co-S	-0.9189	-1.6577
Co-Te	0	-0.2973
Mn-Se	-0.1532	-0.7297
Mn-S	-1.4144	-1.6126
Mn-Te	0	-0.1712
Ni-Te	-0.2703	-0.4505
Sn-S	-0.8829	-1.5766
Pb-Se	0	-1.0901
Pb-S	0	-1.7117
Pb-Te	0	-0.8018
Ga-Te	-0.1622	-0.7387
In-Te	-0.4505	-0.5946
Ag-S	0	-0.8018
Ag-Se	0	0.1982
Ag-Te	-0.009	-0.2162
Mo-S	0	-2.045
Mo-Se	0	-1.0811
Ru-Se	0	-0.6577
Ru-S	0	-1.4775
Ta-Se	-1.2432	-1.3784
Ta-S	-2.2432	-2.5225
Ta-Te	-0.5676	-0.7387

Table B.9: Table of all the algorithms explored and their accuracy.

Model	Accuracy
Decision Tree	0.57
Neural Net	0.57
Naive Bayes	0.57
QDA	0.57
Nearest Neighbors	0.71
Linear SVM	0.71
RBF SVM	0.71
Gaussian Process	0.71
L1 Logistic	0.71
Random Forest	0.71

Appendix C

Python Code: The Reactivity of Triphenylphosphine Fluxes in the Synthesis of Metal Chalcogenides

The following pages contain the python code used for the analysis in chapter 3. The code was written in jupyter notebook and the output of the code is also included.

MetalChalc_coding

May 28, 2022

```
import numpy as np
import pandas as pd
from copy import deepcopy
from sklearn.preprocessing import normalize
import seaborn as sns
sns.set_style('darkgrid')
import matplotlib.pyplot as plt
%matplotlib inline
from matplotlib.colors import ListedColormap
from sklearn.model_selection import train_test_split
from sklearn.preprocessing import StandardScaler
from sklearn.metrics import classification_report, confusion_matrix, accuracy_score
from sklearn.neural_network import MLPClassifier
from sklearn.neighbors import KNeighborsClassifier
from sklearn.svm import SVC
from sklearn.gaussian_process import GaussianProcessClassifier
from sklearn.gaussian_process.kernels import RBF
from sklearn.tree import DecisionTreeClassifier
from sklearn.ensemble import RandomForestClassifier, AdaBoostClassifier
from sklearn.naive_bayes import GaussianNB
from sklearn.discriminant_analysis import QuadraticDiscriminantAnalysis
from sklearn.decomposition import PCA
from sklearn.linear_model import LogisticRegression
from time import time
```

1 Prepping the data:

```
# import data
```

```
df_all = pd.read_csv("MetalChalcogenideRxns_updated.csv")
df = deepcopy(df_all)
```

```
# prep data
```

```
# remove all rows that had a "unclear" under 'Hypothesis supported'
```

```

df = df[df['Hypothesis supported?'] != 'unclear']

# change 'did it work' column to integer
deditwork={"Yes":1,"No":0}
df['HypothesisSupportedInt']=df["Hypothesis supported?"].map(deditwork)

df

```

	Reaction	Product	expected Purity with flux	Purity without flux \
0	Fe-Se	FeSe	99	46
1	Fe-S	FeS	100	16
3	Co-Se	Co9Se8	9	0
4	Co-S	Co9S8	100	13
5	Co-Te	CoTe2	86	75
6	Mn-Se	MnSe	62	60
7	Mn-S	MnS	86	57
8	Mn-Te	MnTe	82	3
9	Ni-Te	mixture	mixture	mixture
10	Sn-S	SnS	75	75
12	Pb-S	PbS	0	95
13	Pb-Te	PbTe	80	83
14	Ga-Te	GaTe	100	1
15	In-Te	mixture	mixture	mixture
16	Ag-S	Ag	100	7
17	Ag-Se	Ag	0	0
18	Ag-Te	Ag2Te	100	68
19	Mo-S	MoS2	0	0
20	Mo-Se	MoSe2	50	52
21	Ru-Se	RuSe2	0	0
23	Ta-Se	mixture	unreacted	unreacted
24	Ta-S	mixture	unreacted	unreacted
25	Ta-Te	mixture	unreacted	TaTe4

	Purity difference	Hypothesis supported?	Formation energy (eV) \
0	53.0	Yes	-0.2804
1	84.0	Yes	-0.8404
3	9.0	Yes	-0.2759
4	87.0	Yes	-0.7809
5	11.0	Yes	-0.2034
6	2.0	No	-0.3676
7	29.0	Yes	-0.8750
8	79.0	Yes	-0.0808
9	NaN	Yes	-0.1825
10	0.0	No	-0.7978
12	-95.0	No	-0.8561
13	-3.0	No	-0.4033
14	99.0	Yes	-0.3717

15	NaN	Yes	-0.2582
16	93.0	Yes	-0.2689
17	0.0	No	-0.0689
18	32.0	Yes	-0.0736
19	0.0	No	-1.3652
20	-2.0	No	-0.7251
21	0.0	No	-0.4382
23	NaN	No	-0.4615
24	NaN	No	-1.0118
25	NaN	No	-0.2832

	Adduct bond dissociation energy (kJ/mol)	Metal density (g/cm ³)	\
0	-271.493265	7.874	
1	-328.478653	7.874	
3	-271.493265	8.900	
4	-328.478653	8.900	
5	-172.059376	8.900	
6	-271.493265	7.470	
7	-328.478653	7.470	
8	-172.059376	7.470	
9	-172.059376	8.908	
10	-328.478653	7.310	
12	-328.478653	11.340	
13	-172.059376	11.340	
14	-172.059376	5.904	
15	-172.059376	7.310	
16	-328.478653	10.490	
17	-271.493265	10.490	
18	-172.059376	10.490	
19	-328.478653	10.280	
20	-271.493265	10.280	
21	-271.493265	12.370	
23	-271.493265	16.650	
24	-328.478653	16.650	
25	-172.059376	16.650	

	Chalcogen density (g/cm ³)	...	Chalcogen melting point (C)	\
0	4.819	...	221.00	
1	1.960	...	115.21	
3	4.819	...	221.00	
4	1.960	...	115.21	
5	6.240	...	449.51	
6	4.819	...	221.00	
7	1.960	...	115.21	
8	6.240	...	449.51	
9	6.240	...	449.51	
10	1.960	...	115.21	

12	1.960	...	115.21
13	6.240	...	449.51
14	6.240	...	449.51
15	6.240	...	449.51
16	1.960	...	115.21
17	4.819	...	221.00
18	6.240	...	449.51
19	1.960	...	115.21
20	4.819	...	221.00
21	4.819	...	221.00
23	4.819	...	221.00
24	1.960	...	115.21
25	6.240	...	449.51

	Metal atomic number	Chalcogen atomic number	\
0	26	34	
1	26	16	
3	27	34	
4	27	16	
5	27	52	
6	25	34	
7	25	16	
8	25	52	
9	28	52	
10	50	16	
12	82	16	
13	82	52	
14	31	52	
15	49	52	
16	47	16	
17	47	34	
18	47	52	
19	42	16	
20	42	34	
21	44	34	
23	73	34	
24	73	16	
25	73	52	

	Metal ionization energy (kJ/mol)	Chalcogen ionization energy (kJ/mol)	\
0	762.5	941.0	
1	762.5	999.6	
3	760.4	941.0	
4	760.4	999.6	
5	760.4	869.3	
6	717.3	941.0	
7	717.3	999.6	

8	717.3	869.3
9	737.1	869.3
10	708.6	999.6
12	715.6	999.6
13	715.6	869.3
14	578.8	869.3
15	558.3	869.3
16	731.0	999.6
17	731.0	941.0
18	731.0	869.3
19	684.3	999.6
20	684.3	941.0
21	710.2	941.0
23	761.0	941.0
24	761.0	999.6
25	761.0	869.3

	Metal electron affinity (kJ/mol)	Chalcogen electron affinity (kJ/mol) \
0	15.7	195.0
1	15.7	200.0
3	63.7	195.0
4	63.7	200.0
5	63.7	190.2
6	0.0	195.0
7	0.0	200.0
8	0.0	190.2
9	112.0	190.2
10	107.3	200.0
12	35.1	200.0
13	35.1	190.2
14	28.9	190.2
15	28.9	190.2
16	125.6	200.0
17	125.6	195.0
18	125.6	190.2
19	71.9	200.0
20	71.9	195.0
21	101.3	195.0
23	31.0	195.0
24	31.0	200.0
25	31.0	190.2

	Minimum chemical potential change (eV/atom) \
0	-0.4955
1	-1.1532
3	-0.3423
4	-0.9189

5	0.0000
6	-0.1532
7	-1.4144
8	0.0000
9	-0.2703
10	-0.8829
12	0.0000
13	0.0000
14	-0.1622
15	-0.4505
16	0.0000
17	0.0000
18	-0.0090
19	0.0000
20	0.0000
21	0.0000
23	-1.2432
24	-2.2432
25	-0.5676

	Maximum chemical potential change (eV/atom)	HypothesisSupportedInt
0	-0.5586	1
1	-1.6757	1
3	-0.5856	1
4	-1.6577	1
5	-0.2973	1
6	-0.7297	0
7	-1.6126	1
8	-0.1712	1
9	-0.4505	1
10	-1.5766	0
12	-1.7117	0
13	-0.8018	0
14	-0.7387	1
15	-0.5946	1
16	-0.8018	1
17	0.1982	0
18	-0.2162	1
19	-2.0450	0
20	-1.0811	0
21	-0.6577	0
23	-1.3784	0
24	-2.5225	0
25	-0.7387	0

[23 rows x 26 columns]

```

# remove columns
columnstodrop=['Purity with flux', 'Purity without flux', 'Purity difference',
               'Product expected', "Hypothesis supported?", 'Reaction']

df = df.drop(columns=columnstodrop)

df

```

	Formation energy (eV)	Adduct bond dissociation energy (kJ/mol)	\
0	-0.2804	-271.493265	
1	-0.8404	-328.478653	
3	-0.2759	-271.493265	
4	-0.7809	-328.478653	
5	-0.2034	-172.059376	
6	-0.3676	-271.493265	
7	-0.8750	-328.478653	
8	-0.0808	-172.059376	
9	-0.1825	-172.059376	
10	-0.7978	-328.478653	
12	-0.8561	-328.478653	
13	-0.4033	-172.059376	
14	-0.3717	-172.059376	
15	-0.2582	-172.059376	
16	-0.2689	-328.478653	
17	-0.0689	-271.493265	
18	-0.0736	-172.059376	
19	-1.3652	-328.478653	
20	-0.7251	-271.493265	
21	-0.4382	-271.493265	
23	-0.4615	-271.493265	
24	-1.0118	-328.478653	
25	-0.2832	-172.059376	

	Metal density (g/cm ³)	Chalcogen density (g/cm ³)	\
0	7.874	4.819	
1	7.874	1.960	
3	8.900	4.819	
4	8.900	1.960	
5	8.900	6.240	
6	7.470	4.819	
7	7.470	1.960	
8	7.470	6.240	
9	8.908	6.240	
10	7.310	1.960	
12	11.340	1.960	
13	11.340	6.240	
14	5.904	6.240	

15	7.310	6.240
16	10.490	1.960
17	10.490	4.819
18	10.490	6.240
19	10.280	1.960
20	10.280	4.819
21	12.370	4.819
23	16.650	4.819
24	16.650	1.960
25	16.650	6.240

	Average density (g/cm ³)	Product density (g/cm ³) \
0	6.3465	5.71
1	4.9170	4.84
3	6.8595	6.80
4	5.4300	5.34
5	7.5700	7.94
6	6.1445	5.49
7	4.7150	4.02
8	6.8550	6.75
9	7.5740	8.23
10	4.6350	5.17
12	6.6500	6.66
13	8.7900	8.24
14	6.0720	5.47
15	6.7750	6.33
16	6.2250	8.79
17	7.6545	8.21
18	8.3650	8.42
19	6.1200	5.00
20	7.5495	6.96
21	8.5945	8.23
23	10.7345	12.22
24	9.3050	10.89
25	11.4450	10.22

	Metal electronegativity	Chalcogen electronegativity \
0	1.83	2.55
1	1.83	2.58
3	1.88	2.55
4	1.88	2.58
5	1.88	2.10
6	1.55	2.55
7	1.55	2.58
8	1.55	2.10
9	1.91	2.10
10	1.96	2.58

12	2.33	2.58
13	2.33	2.10
14	1.81	2.10
15	1.78	2.10
16	1.93	2.58
17	1.93	2.55
18	1.93	2.10
19	2.16	2.58
20	2.16	2.55
21	2.20	2.55
23	1.50	2.55
24	1.50	2.58
25	1.50	2.10

	Electronegativity difference	Metal melting point (C) \
0	0.72	1538.00
1	0.75	1538.00
3	0.67	1495.00
4	0.70	1495.00
5	0.22	1495.00
6	1.00	1246.00
7	1.03	1246.00
8	0.55	1246.00
9	0.19	1455.00
10	0.62	231.93
12	0.25	327.46
13	-0.23	327.46
14	0.29	29.76
15	0.32	156.60
16	0.65	961.78
17	0.62	961.78
18	0.17	961.78
19	0.42	2623.00
20	0.39	2623.00
21	0.35	2334.00
23	1.05	3017.00
24	1.08	3017.00
25	0.60	3017.00

	Chalcogen melting point (C)	Metal atomic number	Chalcogen atomic number \
0	221.00	26	34
1	115.21	26	16
3	221.00	27	34
4	115.21	27	16
5	449.51	27	52
6	221.00	25	34
7	115.21	25	16

8	449.51	25	52
9	449.51	28	52
10	115.21	50	16
12	115.21	82	16
13	449.51	82	52
14	449.51	31	52
15	449.51	49	52
16	115.21	47	16
17	221.00	47	34
18	449.51	47	52
19	115.21	42	16
20	221.00	42	34
21	221.00	44	34
23	221.00	73	34
24	115.21	73	16
25	449.51	73	52

	Metal ionization energy (kJ/mol)	Chalcogen ionization energy (kJ/mol)	\
0	762.5	941.0	
1	762.5	999.6	
3	760.4	941.0	
4	760.4	999.6	
5	760.4	869.3	
6	717.3	941.0	
7	717.3	999.6	
8	717.3	869.3	
9	737.1	869.3	
10	708.6	999.6	
12	715.6	999.6	
13	715.6	869.3	
14	578.8	869.3	
15	558.3	869.3	
16	731.0	999.6	
17	731.0	941.0	
18	731.0	869.3	
19	684.3	999.6	
20	684.3	941.0	
21	710.2	941.0	
23	761.0	941.0	
24	761.0	999.6	
25	761.0	869.3	

	Metal electron affinity (kJ/mol)	Chalcogen electron affinity (kJ/mol)	\
0	15.7	195.0	
1	15.7	200.0	
3	63.7	195.0	
4	63.7	200.0	

5	63.7	190.2
6	0.0	195.0
7	0.0	200.0
8	0.0	190.2
9	112.0	190.2
10	107.3	200.0
12	35.1	200.0
13	35.1	190.2
14	28.9	190.2
15	28.9	190.2
16	125.6	200.0
17	125.6	195.0
18	125.6	190.2
19	71.9	200.0
20	71.9	195.0
21	101.3	195.0
23	31.0	195.0
24	31.0	200.0
25	31.0	190.2

Minimum chemical potential change (eV/atom) \

0	-0.4955
1	-1.1532
3	-0.3423
4	-0.9189
5	0.0000
6	-0.1532
7	-1.4144
8	0.0000
9	-0.2703
10	-0.8829
12	0.0000
13	0.0000
14	-0.1622
15	-0.4505
16	0.0000
17	0.0000
18	-0.0090
19	0.0000
20	0.0000
21	0.0000
23	-1.2432
24	-2.2432
25	-0.5676

	Maximum chemical potential change (eV/atom)	HypothesisSupportedInt
0	-0.5586	1

1	-1.6757	1
3	-0.5856	1
4	-1.6577	1
5	-0.2973	1
6	-0.7297	0
7	-1.6126	1
8	-0.1712	1
9	-0.4505	1
10	-1.5766	0
12	-1.7117	0
13	-0.8018	0
14	-0.7387	1
15	-0.5946	1
16	-0.8018	1
17	0.1982	0
18	-0.2162	1
19	-2.0450	0
20	-1.0811	0
21	-0.6577	0
23	-1.3784	0
24	-2.5225	0
25	-0.7387	0

2 Plotting Pairplots:

We know minimum change in chemical potential should be important

By plotting minimum change in chemical potential vs all the other features we can visualize correlations as clusters

We can then analyze these plots with SVM to determine what other features are most important

```
h = 0.02 # step size in the mesh

names = [
    "Formation energy (eV)",
    """"Adduct bond dissociation
energy (kJ/mol)""",
    "Metal density ( $\text{g/cm}^3$ )",
    "Chalcogen density ( $\text{g/cm}^3$ )",
    "Average density ( $\text{g/cm}^3$ )",
    "Product density ( $\text{g/cm}^3$ )",
    "Metal electronegativity",
    "Chalcogen electronegativity",
    "Electronegativity difference",
    "Metal melting point ( $\text{K}$ )",
    "Chalcogen melting point ( $\text{K}$ )",
    "Metal atomic number",
```

```

    "Chalcogen atomic number",
    """Metal ionization
energy (kJ/mol)""",
    """Chalcogen ionization
energy (kJ/mol)""",
    """Metal electron
affinity (kJ/mol)""",
    """Chalcogen electron
affinity (kJ/mol)""",
    """Minimum chemical potential
change (eV/atom)""",
    """Maximum chemical potential
change (eV/atom)""",
]

Xvalues = [
    df["Formation energy (eV)"],
    df["Adduct bond dissociation energy (kJ/mol)"],
    df["Metal density (g/cm^3)"],
    df["Chalcogen density (g/cm^3)"],
    df["Average density (g/cm^3)"],
    df["Product density (g/cm^3)"],
    df["Metal electronegativity"],
    df["Chalcogen electronegativity"],
    df["Electronegativity difference"],
    df["Metal melting point (C)"],
    df["Chalcogen melting point (C)"],
    df["Metal atomic number"],
    df["Chalcogen atomic number"],
    df["Metal ionization energy (kJ/mol)"],
    df["Chalcogen ionization energy (kJ/mol)"],
    df["Metal electron affinity (kJ/mol)"],
    df["Chalcogen electron affinity (kJ/mol)"],
    df["Minimum chemical potential change (eV/atom)"],
    df["Maximum chemical potential change (eV/atom)"]
]

yvalue1 = df["Minimum chemical potential change (eV/atom)"].to_numpy()

yvalue = df['HypothesisSupportedInt'].to_numpy()

figure = plt.figure(figsize=(30, 30))
i = 1

# iterate over Xvalues
for name, Xvalue in zip(names, Xvalues):

```

```

# Prep datasets
X = np.dstack((Xvalue.values, yvalue1))[0]
y= yvalue
X = StandardScaler().fit_transform(X)
X_train, X_test, y_train, y_test = train_test_split(X, y, test_size=0.3,
                                                    random_state=42)

x_min, x_max = X[:, 0].min() - 0.5, X[:, 0].max() + 0.5
y_min, y_max = X[:, 1].min() - 0.5, X[:, 1].max() + 0.5
xx, yy = np.meshgrid(np.arange(x_min, x_max, h), np.arange(y_min, y_max, h))

# Create the model
clf = SVC(kernel='linear', C=1000)
clf.fit(X_train, y_train)
score = clf.score(X_test, y_test)

# Predict values based on the model
y_pred = clf.predict(X_test)

# Determine accuracy of predictions/model
print("Accuracy for", name, "is:", accuracy_score(y_test, y_pred))

# Graph the model
ax = plt.subplot(4, 5, i)
if i==1 or i==6 or i==11 or i==16:
    ax.set_ylabel("""Minimum chemical potential
change (eV/atom)""", fontsize=30)
clf.fit(X_train, y_train)

# Plot the decision boundary. For that, we will assign a color to each point
#in the mesh [x_min, x_max]x[y_min, y_max].
if hasattr(clf, "decision_function"):
    Z = clf.decision_function(np.c_[xx.ravel(), yy.ravel()])
else:
    Z = clf.predict_proba(np.c_[xx.ravel(), yy.ravel()])[:, 1]

# Put the result into a color plot
cm = plt.cm.RdBu
cm_bright = ListedColormap(["#FF0000", "#0000FF"])
Z = Z.reshape(xx.shape)
ax.contourf(xx, yy, Z, cmap=cm, alpha=0.8)

# Plot the training points
ax.scatter(
    X_train[:, 0], X_train[:, 1], s=300, c=y_train, cmap=cm_bright,
    →edgecolors="k"

```

```

)

# Plot the testing points
ax.scatter(
    X_test[:, 0], X_test[:, 1], s = 300, c=y_test, cmap=cm_bright,
    ↪edgecolors="k",
    alpha=0.5,
)

ax.set_xlim(xx.min(), xx.max())
ax.set_ylim(yy.min(), yy.max())
ax.set_xticks(())
ax.set_yticks(())
ax.set_title(name, fontsize=30)
ax.text(
    xx.max() - 0.3,
    yy.min() + 0.3,
    ("% .2f" % score).lstrip("0"),
    size=40, weight='bold',
    horizontalalignment="right",
)
i+=1
plt.tight_layout()
plt.show()

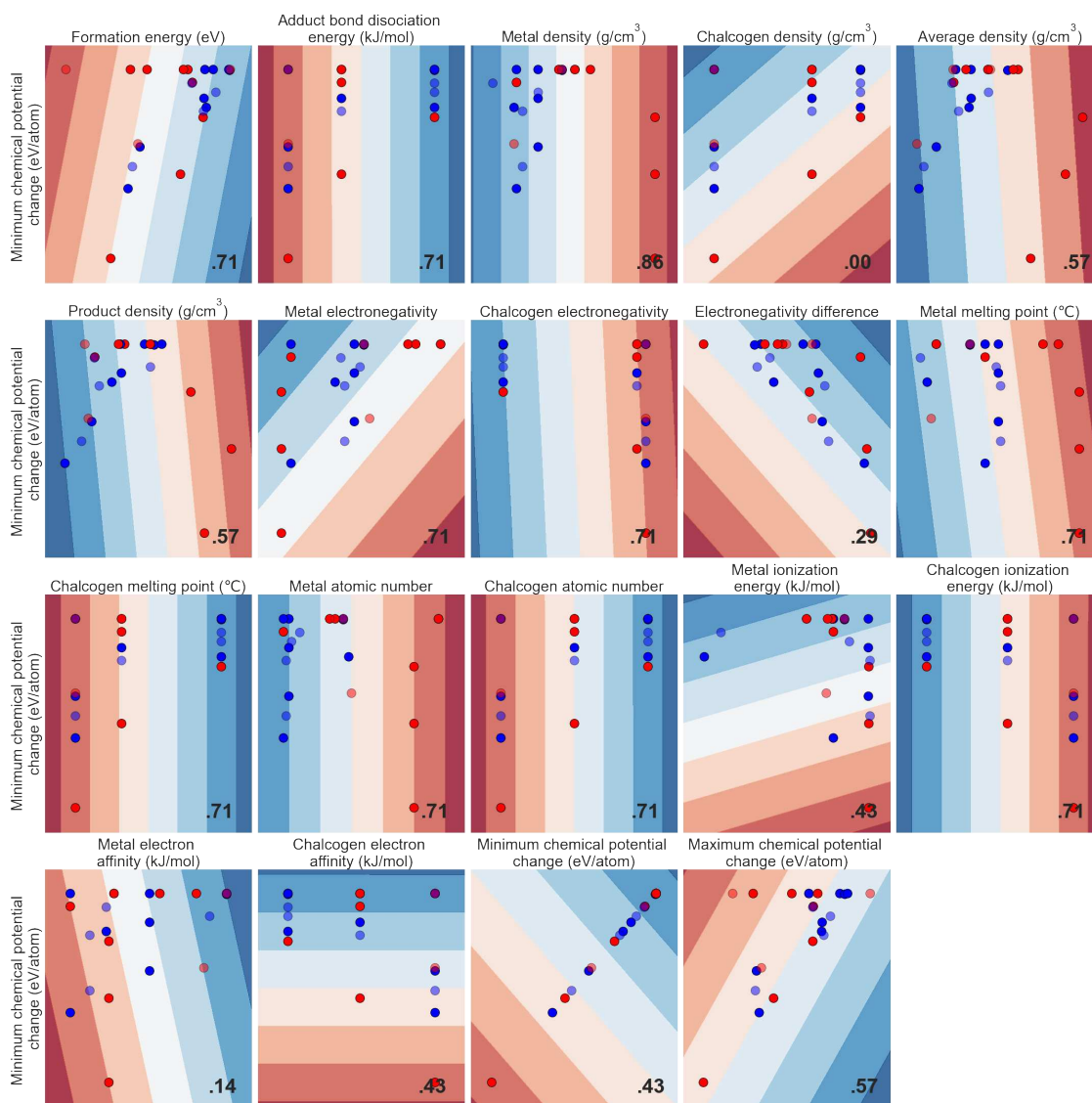
```

Accuracy for Formation energy (eV) is: 0.7142857142857143
 Accuracy for Adduct bond dissociation
 energy (kJ/mol) is: 0.7142857142857143
 Accuracy for Metal density (g/cm^3) is: 0.8571428571428571
 Accuracy for Chalcogen density (g/cm^3) is: 0.0
 Accuracy for Average density (g/cm^3) is: 0.5714285714285714
 Accuracy for Product density (g/cm^3) is: 0.5714285714285714
 Accuracy for Metal electronegativity is: 0.7142857142857143
 Accuracy for Chalcogen electronegativity is: 0.7142857142857143
 Accuracy for Electronegativity difference is: 0.2857142857142857
 Accuracy for Metal melting point (°C) is: 0.7142857142857143
 Accuracy for Chalcogen melting point (°C) is: 0.7142857142857143
 Accuracy for Metal atomic number is: 0.7142857142857143
 Accuracy for Chalcogen atomic number is: 0.7142857142857143
 Accuracy for Metal ionization
 energy (kJ/mol) is: 0.42857142857142855
 Accuracy for Chalcogen ionization
 energy (kJ/mol) is: 0.7142857142857143
 Accuracy for Metal electron
 affinity (kJ/mol) is: 0.14285714285714285
 Accuracy for Chalcogen electron
 affinity (kJ/mol) is: 0.42857142857142855
 Accuracy for Minimum chemical potential

change (eV/atom) is: 0.42857142857142855

Accuracy for Maximum chemical potential

change (eV/atom) is: 0.5714285714285714



Based on this chemical intuition approach the following features are the most important: - Minimum chemical potential change (eV/atom) - Metal density (g/cm³)

second most - Formation energy (eV) - Adduct bond dissociation energy (kJ/mol) - Metal electronegativity - Chalcogen electronegativity - Metal melting point (C) - Chalcogen melting point (C) - metal atomic number - Chalcogen atomic number - Chalcogen ionization energy (kJ/mol)

Lets confirm this with machine learning


```

result_dict[name] = {
    'model_params': clf.get_params(),
    'score': score,
    'time': dt}

```

```

Now fitting and evaluating model Nearest Neighbors, Score: 0.7142857142857143
Now fitting and evaluating model Linear SVM, Score: 0.7142857142857143
Now fitting and evaluating model RBF SVM, Score: 0.7142857142857143
Now fitting and evaluating model Gaussian Process, Score: 0.7142857142857143
Now fitting and evaluating model Decision Tree, Score: 0.5714285714285714
Now fitting and evaluating model Random Forest, Score: 0.7142857142857143
Now fitting and evaluating model Neural Net, Score: 0.5714285714285714
Now fitting and evaluating model Naive Bayes, Score: 0.5714285714285714
Now fitting and evaluating model QDA, Score: 0.5714285714285714
Now fitting and evaluating model L1 Logistic, Score: 0.7142857142857143

```

```

C:\ProgramData\Anaconda3\lib\site-
packages\sklearn\neural_network\_multilayer_perceptron.py:614:
ConvergenceWarning: Stochastic Optimizer: Maximum iterations (200) reached and
the optimization hasn't converged yet.
    warnings.warn(
C:\ProgramData\Anaconda3\lib\site-packages\sklearn\discriminant_analysis.py:808:
UserWarning: Variables are collinear
    warnings.warn("Variables are collinear")

```

Variables are collinear- which is not surprising based on the features chosen

```

# look at results in a table
results_df = pd.DataFrame.from_dict(result_dict)
results_df = results_df.sort_values('score',axis=1).transpose()
results_df

```

	model_params \	
Decision Tree	{'ccp_alpha': 0.0, 'class_weight': None, 'crit...	
Neural Net	{'activation': 'relu', 'alpha': 0.0001, 'batch...	
Naive Bayes	{'priors': None, 'var_smoothing': 1e-09}	
QDA	{'priors': None, 'reg_param': 0.0, 'store_cova...	
Nearest Neighbors	{'algorithm': 'auto', 'leaf_size': 30, 'metric...	
Linear SVM	{'C': 1.0, 'break_ties': False, 'cache_size': ...	
RBF SVM	{'C': 1.0, 'break_ties': False, 'cache_size': ...	
Gaussian Process	{'copy_X_train': True, 'kernel': None, 'max_it...	
Random Forest	{'bootstrap': True, 'ccp_alpha': 0.0, 'class_w...	
L1 Logistic	{'C': 1.0, 'class_weight': None, 'dual': False...	
	score	time
Decision Tree	0.571429	0.0
Neural Net	0.571429	0.206904
Naive Bayes	0.571429	0.004516
QDA	0.571429	0.010778

Nearest Neighbors	0.714286	0.074535
Linear SVM	0.714286	0.008022
RBF SVM	0.714286	0.005762
Gaussian Process	0.714286	0.018182
Random Forest	0.714286	0.183304
L1 Logistic	0.714286	0.010528

3.0.2 Fine tuning the model

```
# define the model
classifier = RandomForestClassifier(random_state=1)
classifier.fit(X_train, y_train)
# show accuracy
y_pred = classifier.predict(X_test)
y_pred
print(confusion_matrix(y_test, y_pred))
print(classification_report(y_test, y_pred))
print(accuracy_score(y_test, y_pred))
```

```
[[3 1]
 [1 2]]
```

	precision	recall	f1-score	support
0	0.75	0.75	0.75	4
1	0.67	0.67	0.67	3
accuracy			0.71	7
macro avg	0.71	0.71	0.71	7
weighted avg	0.71	0.71	0.71	7

0.7142857142857143

```
from sklearn.model_selection import GridSearchCV
classifier = RandomForestClassifier(random_state=1)
classifier.fit(X_train, y_train)
y_pred = classifier.predict(X_test)

# Parameters to explore
parameters = {'n_estimators':range(10,100), 'max_depth':range(2,20),
              'min_samples_split':range(2,3), 'min_samples_leaf':range(1,3)}
# make model with those parameters
clf_GridCV = GridSearchCV(RandomForestClassifier(random_state=1), parameters,
                           cv=3)

clf_GridCV.fit(X=X_train, y=y_train)

print(clf_GridCV.best_score_, clf_GridCV.best_params_)
```

```
1.0 {'max_depth': 3, 'min_samples_leaf': 1, 'min_samples_split': 2,
'n_estimators': 13}
```

```
classifier = RandomForestClassifier(n_estimators=13, max_depth=3,
    ↪min_samples_split=2,
                                min_samples_leaf=1, random_state=1)
classifier.fit(X_train, y_train)
# predict values
y_pred = classifier.predict(X_test)
y_pred
print(confusion_matrix(y_test, y_pred))
print(classification_report(y_test, y_pred))
print(accuracy_score(y_test, y_pred))
```

```
[[3 1]
 [0 3]]
```

	precision	recall	f1-score	support
0	1.00	0.75	0.86	4
1	0.75	1.00	0.86	3
accuracy			0.86	7
macro avg	0.88	0.88	0.86	7
weighted avg	0.89	0.86	0.86	7

```
0.8571428571428571
```

3.0.3 Figuring out which features are the most important

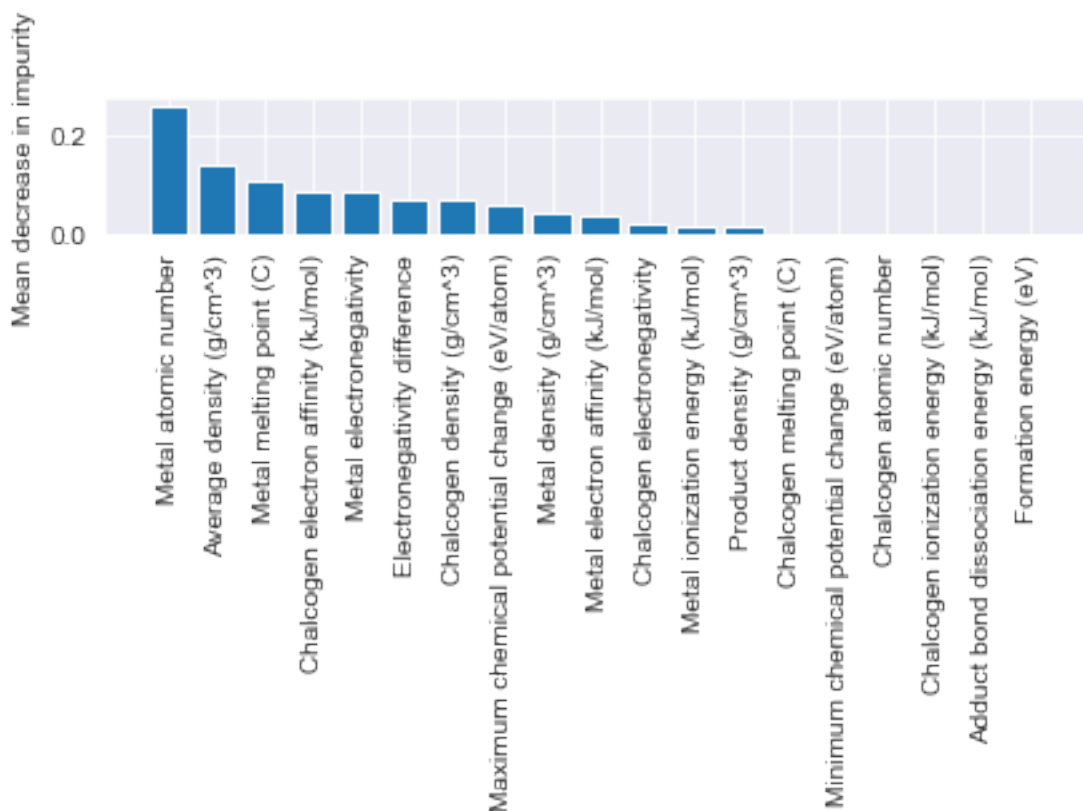
```
# plot the feature importances using MDI
classifier = RandomForestClassifier(n_estimators=13, max_depth=3,
    ↪min_samples_split=2,
                                min_samples_leaf=1, random_state=1)
classifier.fit(X_train, y_train)

importances = classifier.feature_importances_

sorted = np.argsort(importances)[::-1]

feature_names = [X_train.columns[i] for i in sorted]

plt.figure()
plt.ylabel("Mean decrease in impurity")
plt.bar(range(X.shape[1]), importances[sorted])
plt.xticks(range(X.shape[1]), feature_names, rotation=90)
plt.tight_layout()
plt.show()
```



Based on this the most important features according to machine learning are as follows:

- Metal atomic number
- Average density (g/cm³)
- Metal melting point (C)
- Chalcogen electron affinity (kJ/mol)
- Metal electronegativity

Reminder: the most important features according to the chemical intuition approach were

- Minimum chemical potential change (eV/atom)
- Metal density (g/cm³)

second most - Formation energy (eV) - Adduct bond dissociation energy (kJ/mol) - Metal electronegativity - Chalcogen electronegativity - Metal melting point (C) - Chalcogen melting point (C) - Chalcogen atomic number - Chalcogen ionization energy (kJ/mol)

So in common they have - metal density - metal electronegativity - metal melting point

3.0.4 Principal component Analysis

```
# scale/split the data
HypothesisSupported={1:"Yes",0:"No"}
df['Hypothesis supported?']=df['HypothesisSupportedInt'].map(HypothesisSupported)
X = df.select_dtypes(include=np.number).drop(columns=['HypothesisSupportedInt'])
X = X.reset_index(drop=True)
y = df['Hypothesis supported?']
y = y.reset_index(drop=True)
X_train, X_test, y_train, y_test = train_test_split(X,y, test_size=0.
    →3,random_state=0)
scaler = StandardScaler()
scaler.fit(X_train)
scaled_data = scaler.transform(X_train)
scaler.fit(X_test)
scaled_data_test = scaler.transform(X_test)
```

```
# Complete PCA and print some potentially important values
pca = PCA(n_components=2)
pca.fit(scaled_data)
print(pca.explained_variance_ratio_)
print(pca.singular_values_)

x_pca = pca.transform(scaled_data)
df_pca = pd.DataFrame(data=x_pca,columns=["PC1", "PC2"])
df_pca['Hypothesis supported?'] = y
```

```
[0.51872644 0.18558464]
[12.55758083  7.51117368]
```

```
# determine accuracy of PCA through regression
from sklearn.linear_model import LogisticRegression

train_data = pca.transform(scaled_data)
test_data = pca.transform(scaled_data_test)

logisticRegr = LogisticRegression()
logisticRegr.fit(train_data, y_train)

y_test_hat=logisticRegr.predict(test_data)
test_accuracy=accuracy_score(y_test,y_test_hat)*100
test_accuracy
print("Accuracy for our testing dataset is : {:.3f}%".format(test_accuracy) )
```

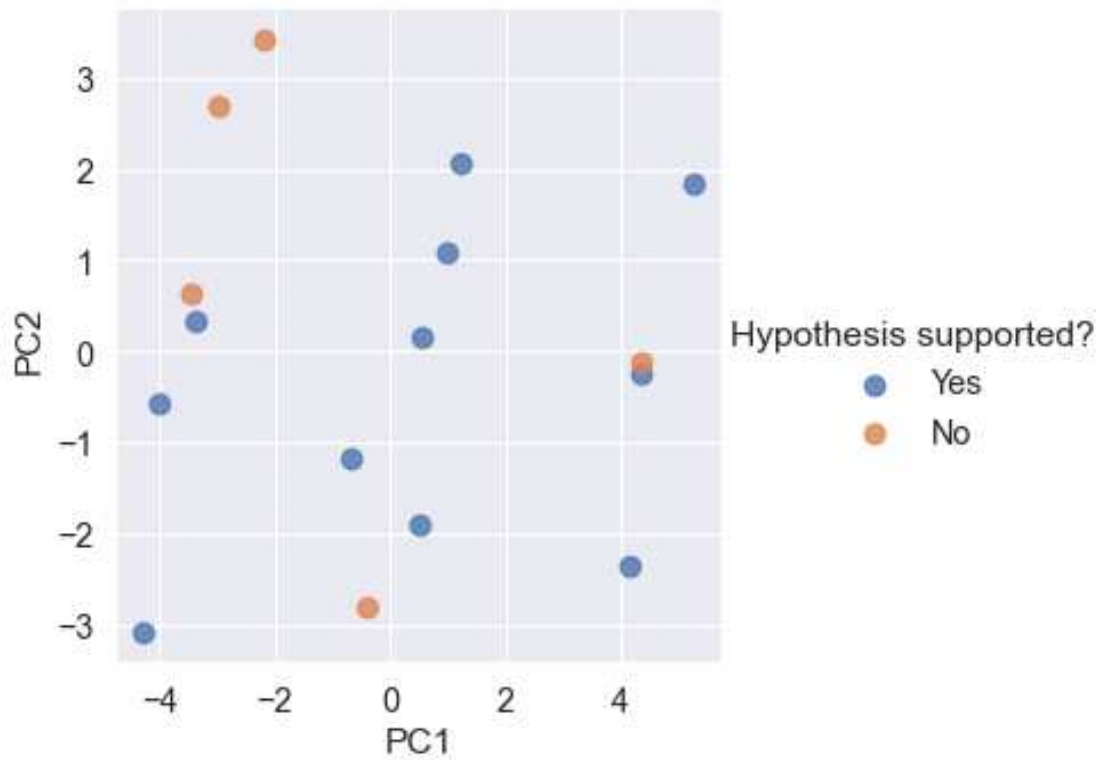
Accuracy for our testing dataset is : 71.429%

```
# plots the PCA
sns.set(font_scale=1.3)
```

```

sns.lmplot( x="PC1", y="PC2",
            data=df_pca,
            fit_reg=False,
            hue='Hypothesis supported?', # color by cluster
            legend=True,
            scatter_kws={"s": 80}) # specify the point size
plt.savefig('PCA.png', dpi=600)

```



```

# Plots which component accounts for the most variance
dfpc = pd.DataFrame({'var':pca.explained_variance_ratio_,
                    'PC':['PC1','PC2']})
sns.barplot(x='PC',y="var",
            data=dfpc, color="c");

```

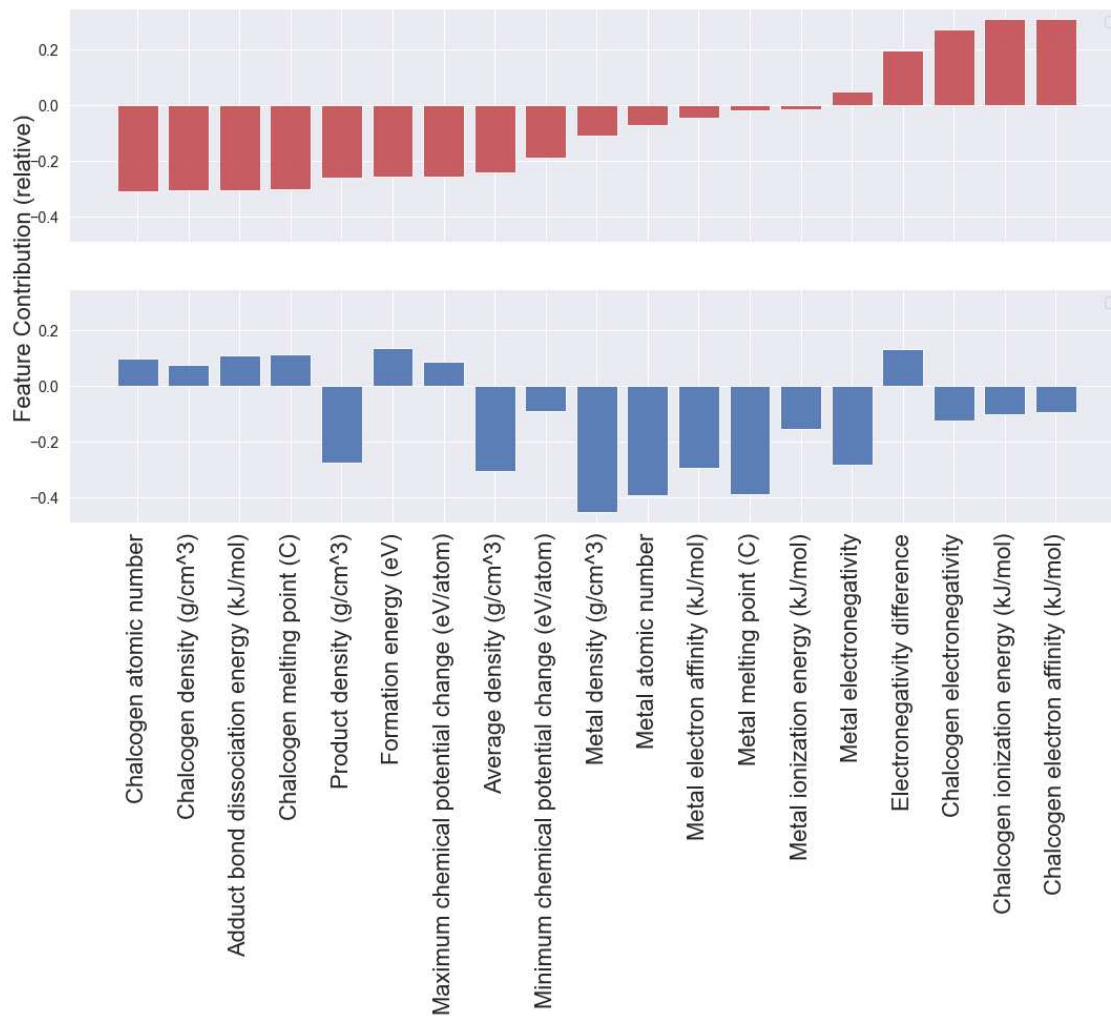


```
# plots how much each feature contributed to each component
indices = np.argsort(pca.components_[0])
fig,ax=plt.subplots(nrows=2, ncols=1, sharey=True, sharex=True, figsize=(18,9))
ax[0].bar(range(X.shape[1]), pca.components_[0][indices],
          color="r", align="center",alpha=.9)
ax[1].bar(range(X.shape[1]), pca.components_[1][indices],
          color="b", align="center",alpha=0.9)
plt.xticks(range(X.shape[1]), X.columns[indices],rotation='vertical', fontsize=22)
fig.text(0.085, 0.5, 'Feature Contribution (relative)', fontsize= 22,
        va='center', rotation='vertical')
ax[0].legend()
ax[1].legend()
```

No handles with labels found to put in legend.

No handles with labels found to put in legend.

<matplotlib.legend.Legend at 0x1c4d1a8b970>



Features that create the most separation according to PCA:

- Chalcogen atomic number
- Chalcogen density
- Adduct BDE
- Chalcogen melting point
- Chalcogen electron affinity
- Chalcogen ionization energy

Reminder: the most important features according to the chemical intuition approach were

- Minimum change in chemical potential
- Metal density

second most - Formation E - BDE of adduct - M electroneg - Ch electroneg - m.p. of metal - m.p. of chalc - chalc atomic # - IE of chalc

And according to machine learning:

- metal electroneg
- metal atomic number
- metal density
- avg density
- m.p. of metal

The limited feature set chosen is as follows: - Minimum change in chemical potential - Metal density - BDE of adduct - M electroneg - m.p. of metal - m.p. of chalc - chalc atomic # - IE of chalc

4 Analysis with limited features:

```
# create a dataframe with a reduced number of features

# features included are Metal density, BDE of adduct, M electroneg, m.p. of metal,
#m.p. of chalc, chalc atomic #, IE of chalc, min change in chem pot
columnstodrop_limitedFeatures=["Product density (g/cm^3)",
                               "Chalcogen density (g/cm^3)",
                               "Chalcogen electronegativity",
                               "Electronegativity difference",
                               "Metal atomic number",
                               "Metal ionization energy (kJ/mol)",
                               "Metal electron affinity (kJ/mol)",
                               "Chalcogen electron affinity (kJ/mol)",
                               "Maximum chemical potential change (eV/atom)",
                               "Formation energy (eV)",
                               "Average density (g/cm^3)"]

df3 = deepcopy(df)
df3 = df3.drop(columns=columnstodrop_limitedFeatures)
df3.head
```

```
<bound method NDFrame.head of
Metal density (g/cm^3) \      Adduct bond dissociation energy (kJ/mol)
0                          -271.493265                7.874
1                          -328.478653                7.874
3                          -271.493265                8.900
4                          -328.478653                8.900
5                          -172.059376                8.900
6                          -271.493265                7.470
7                          -328.478653                7.470
8                          -172.059376                7.470
9                          -172.059376                8.908
10                         -328.478653                7.310
12                         -328.478653                11.340
13                         -172.059376                11.340
```

14	-172.059376	5.904
15	-172.059376	7.310
16	-328.478653	10.490
17	-271.493265	10.490
18	-172.059376	10.490
19	-328.478653	10.280
20	-271.493265	10.280
21	-271.493265	12.370
23	-271.493265	16.650
24	-328.478653	16.650
25	-172.059376	16.650

	Metal electronegativity	Metal melting point (C)	\
0	1.83	1538.00	
1	1.83	1538.00	
3	1.88	1495.00	
4	1.88	1495.00	
5	1.88	1495.00	
6	1.55	1246.00	
7	1.55	1246.00	
8	1.55	1246.00	
9	1.91	1455.00	
10	1.96	231.93	
12	2.33	327.46	
13	2.33	327.46	
14	1.81	29.76	
15	1.78	156.60	
16	1.93	961.78	
17	1.93	961.78	
18	1.93	961.78	
19	2.16	2623.00	
20	2.16	2623.00	
21	2.20	2334.00	
23	1.50	3017.00	
24	1.50	3017.00	
25	1.50	3017.00	

	Chalcogen melting point (C)	Chalcogen atomic number	\
0	221.00	34	
1	115.21	16	
3	221.00	34	
4	115.21	16	
5	449.51	52	
6	221.00	34	
7	115.21	16	
8	449.51	52	
9	449.51	52	

10	115.21	16
12	115.21	16
13	449.51	52
14	449.51	52
15	449.51	52
16	115.21	16
17	221.00	34
18	449.51	52
19	115.21	16
20	221.00	34
21	221.00	34
23	221.00	34
24	115.21	16
25	449.51	52

	Chalcogen ionization energy (kJ/mol) \
0	941.0
1	999.6
3	941.0
4	999.6
5	869.3
6	941.0
7	999.6
8	869.3
9	869.3
10	999.6
12	999.6
13	869.3
14	869.3
15	869.3
16	999.6
17	941.0
18	869.3
19	999.6
20	941.0
21	941.0
23	941.0
24	999.6
25	869.3

	Minimum chemical potential change (eV/atom)	HypothesisSupportedInt \
0	-0.4955	1
1	-1.1532	1
3	-0.3423	1
4	-0.9189	1
5	0.0000	1
6	-0.1532	0

7	-1.4144	1
8	0.0000	1
9	-0.2703	1
10	-0.8829	0
12	0.0000	0
13	0.0000	0
14	-0.1622	1
15	-0.4505	1
16	0.0000	1
17	0.0000	0
18	-0.0090	1
19	0.0000	0
20	0.0000	0
21	0.0000	0
23	-1.2432	0
24	-2.2432	0
25	-0.5676	0

Hypothesis supported?

0	Yes
1	Yes
3	Yes
4	Yes
5	Yes
6	No
7	Yes
8	Yes
9	Yes
10	No
12	No
13	No
14	Yes
15	Yes
16	Yes
17	No
18	Yes
19	No
20	No
21	No
23	No
24	No
25	No >

4.0.1 Principal component analysis:

```
# scale the data- this is scaling the unsplit data so this uses all the samples_
→available

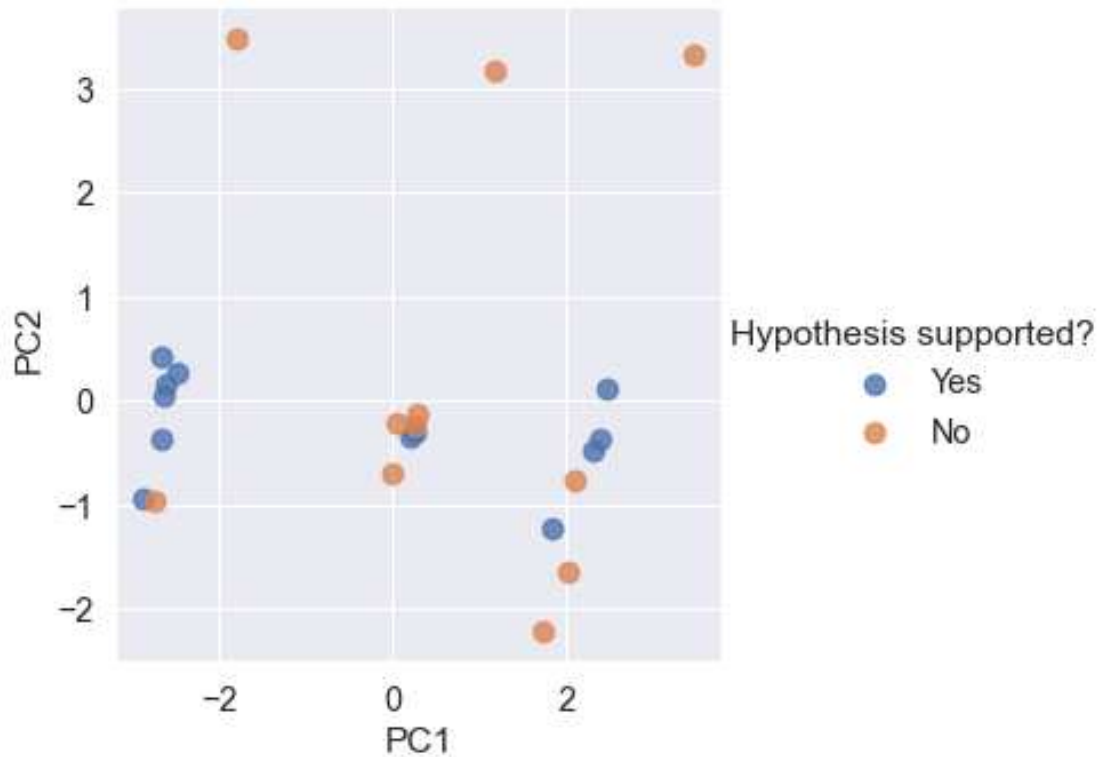
diditwork={1:"Yes",0:"No"}
df['Hypothesis supported?']=df['HypothesisSupportedInt'].map(diditwork)
X = df3.select_dtypes(include=np.number).drop(columns=['HypothesisSupportedInt'])
diditworkInt = df3['HypothesisSupportedInt']
X = X.reset_index(drop=True)
y = df['Hypothesis supported?']
y = y.reset_index(drop=True)
scaler = StandardScaler()
scaler.fit(X)
scaled_data = scaler.transform(X)
```

```
# Complete PCA and print some potentially important values
pca = PCA(n_components=2)
pca.fit(scaled_data)
print(pca.explained_variance_ratio_)
print(pca.singular_values_)

x_pca = pca.transform(scaled_data)
df_pca = pd.DataFrame(data=x_pca,columns=["PC1", "PC2"])
df_pca['Hypothesis supported?'] = y
```

```
[0.5387647  0.25258068]
[9.95654081  6.81724617]
```

```
# plots the PCA
sns.set(font_scale=1.3)
sns.lmplot( x="PC1", y="PC2",
            data=df_pca,
            fit_reg=False,
            hue='Hypothesis supported?', # color by cluster
            legend=True,
            scatter_kws={"s": 80}) # specify the point size
plt.savefig('PCA.png', dpi=600)
```



4.0.2 Applying all the machine learning models to the PCA:

```
# Put together dataset from PCA
X1 = x_pca
y = diditworkInt
y1 = y.to_numpy()
datasets = (X1,y1)
```

```
# Code source: Gaël Varoquaux
#               Andreas Müller
# Modified for documentation by Jaques Grobler
# License: BSD 3 clause
# Furthur modified by M. Jewels Fallon
# scikit-learn.org/stable/auto_examples/classification/
# →plot_classifier_comparison.html
```

```
import numpy as np
import matplotlib.pyplot as plt
from matplotlib.colors import ListedColormap
from sklearn.model_selection import train_test_split
from sklearn.preprocessing import StandardScaler
from sklearn.datasets import make_moons, make_circles, make_classification
```

```

from sklearn.neural_network import MLPClassifier
from sklearn.neighbors import KNeighborsClassifier
from sklearn.svm import SVC
from sklearn.gaussian_process import GaussianProcessClassifier
from sklearn.gaussian_process.kernels import RBF
from sklearn.tree import DecisionTreeClassifier
from sklearn.ensemble import RandomForestClassifier, AdaBoostClassifier
from sklearn.naive_bayes import GaussianNB
from sklearn.discriminant_analysis import QuadraticDiscriminantAnalysis

h = 0.02 # step size in the mesh

names = [
    "Nearest Neighbors",
    "Linear SVM",
    "RBF SVM",
    "Gaussian Process",
    "Decision Tree",
    "Random Forest",
    "Neural Net",
    "AdaBoost",
    "Naive Bayes",
    "QDA"
]

classifiers = [
    KNeighborsClassifier(3),
    SVC(kernel="linear", C=0.025),
    SVC(gamma=2, C=1),
    GaussianProcessClassifier(1.0 * RBF(1.0)),
    DecisionTreeClassifier(max_depth=5),
    RandomForestClassifier(max_depth=5, n_estimators=10, max_features=1),
    MLPClassifier(alpha=1, max_iter=1000),
    AdaBoostClassifier(),
    GaussianNB(),
    QuadraticDiscriminantAnalysis()
]

figure = plt.figure(figsize=(32, 21))
i = 1

# preprocess dataset, split into training and test part
X, y = datasets
X_train, X_test, y_train, y_test = train_test_split(
    X, y, test_size=.3, random_state=42
)

```

```

ds_cnt = 0

x_min, x_max = X[:, 0].min() - 0.5, X[:, 0].max() + 0.5
y_min, y_max = X[:, 1].min() - 0.5, X[:, 1].max() + 0.5
xx, yy = np.meshgrid(np.arange(x_min, x_max, h), np.arange(y_min, y_max, h))

# just plot the dataset first
cm = plt.cm.RdBu
cm_bright = ListedColormap(["#FF0000", "#0000FF"])
#ax = plt.subplot(len(datasets), len(classifiers) + 1, i)
ax = plt.subplot(3, 4, i)
if ds_cnt == 0:
    ax.set_title("Input data", fontsize=30)
# Plot the training points
ax.scatter(X_train[:, 0], X_train[:, 1], s=500, c=y_train,
           cmap=cm_bright, edgecolors="k")

# Plot the testing points
ax.scatter(
    X_test[:, 0], X_test[:, 1], c=y_test, cmap=cm_bright, alpha=0.6,
    →edgecolors="k"
)

ax.set_xlim(xx.min(), xx.max())
ax.set_ylim(yy.min(), yy.max())
ax.set_xticks(())
ax.set_yticks(())
i += 1

# iterate over classifiers
for name, clf in zip(names, classifiers):
#     ax = plt.subplot(len(datasets), len(classifiers) + 1, i)
    ax = plt.subplot(3, 4, i)
    clf.fit(X_train, y_train)
    score = clf.score(X_test, y_test)
    print("Accuracy for", name, "is:", score)

# Plot the decision boundary. For that, we will assign a color to each
# point in the mesh [x_min, x_max]x[y_min, y_max].
if hasattr(clf, "decision_function"):
    Z = clf.decision_function(np.c_[xx.ravel(), yy.ravel()])
else:
    Z = clf.predict_proba(np.c_[xx.ravel(), yy.ravel()])[:, 1]

# Put the result into a color plot
Z = Z.reshape(xx.shape)
ax.contourf(xx, yy, Z, cmap=cm, alpha=0.8)

```

```

# Plot the training points
ax.scatter(
    X_train[:, 0], X_train[:, 1], s = 500, c=y_train, cmap=cm_bright,
    →edgecolors="k"
)
# Plot the testing points
ax.scatter(
    X_test[:, 0],
    X_test[:, 1],
    s = 500,
    c=y_test,
    cmap=cm_bright,
    edgecolors="k",
    alpha=0.5,
)

ax.set_xlim(xx.min(), xx.max())
ax.set_ylim(yy.min(), yy.max())
ax.set_xticks(())
ax.set_yticks(())
if ds_cnt == 0:
    ax.set_title(name, fontsize=30)
ax.text(
    xx.max() - 0.3,
    yy.min() + 0.3,
    ("%.2f" % score).rstrip("0"),
    size=40, weight='bold',
    horizontalalignment="right",
)
i+=1

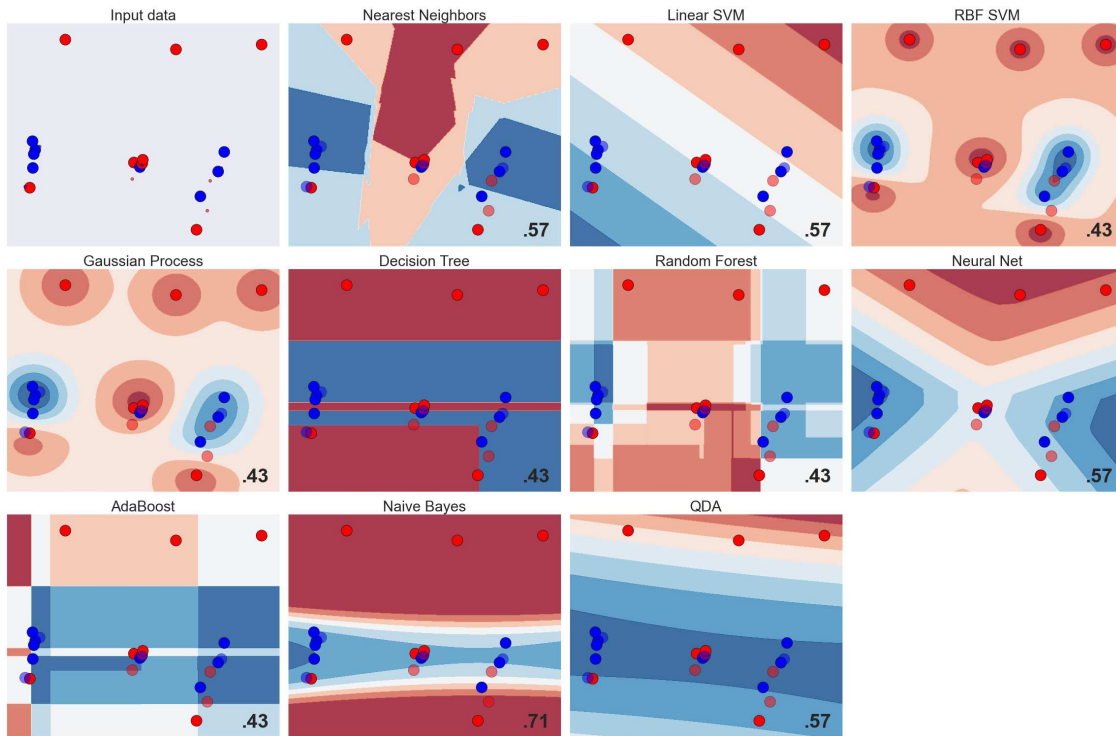
plt.tight_layout()
plt.show()

```

```

Accuracy for Nearest Neighbors is: 0.5714285714285714
Accuracy for Linear SVM is: 0.5714285714285714
Accuracy for RBF SVM is: 0.42857142857142855
Accuracy for Gaussian Process is: 0.42857142857142855
Accuracy for Decision Tree is: 0.42857142857142855
Accuracy for Random Forest is: 0.42857142857142855
Accuracy for Neural Net is: 0.5714285714285714
Accuracy for AdaBoost is: 0.42857142857142855
Accuracy for Naive Bayes is: 0.7142857142857143
Accuracy for QDA is: 0.5714285714285714

```



Seems like RBF SVM is the most accurate so this will be used for predictions

5 Predicting other reactions:

```
# import data on reactions to predict

df_test = pd.read_csv("ToTest_Updates.csv")
df2 = deepcopy(df_test)

df2['HypothesisSupportedInt'] = 3
X_test = df2.select_dtypes(include=np.number).
    →drop(columns=['HypothesisSupportedInt'])
X_test = X_test.reset_index(drop=True)
y_test = df3['HypothesisSupportedInt']
y_test = y_test.reset_index(drop=True)
scaler = StandardScaler()
scaler.fit(X_test)
scaled_test_data = scaler.transform(X_test)

# scale the data- this is scaling the unsplit data so this uses all the samples
→available
X = df3.select_dtypes(include=np.number).drop(columns=['HypothesisSupportedInt'])
```

```

X_train = X.reset_index(drop=True)
y = df3['HypothesisSupportedInt']
y_train = y.reset_index(drop=True)
scaler = StandardScaler()
scaler.fit(X_train)
scaled_train_data = scaler.transform(X_train)

# Complete PCA and print some potentially important values
pca = PCA(n_components=2)
pca.fit(scaled_train_data)

x_pca = pca.transform(scaled_train_data)
df_pca = pd.DataFrame(data=x_pca, columns=["PC1", "PC2"])
df_pca['Class'] = y

# determine accuracy of PCA through regression
classifier = SVC(gamma=2, C=1)
classifier.fit(scaled_train_data, y_train)

y_pred = classifier.predict(scaled_test_data)

# print table of the predicted reactions and the predicted outcome
reaction = df2["Product expected"]
df4 = pd.DataFrame(y_pred, columns = ['HypothesisSupportedInt'])
dicitwork={1:"Yes",0:"No"}
df4['Should it work']=df4["HypothesisSupportedInt"].map(dicitwork)
df4 = df4.drop(columns='HypothesisSupportedInt')
predictions = pd.concat([reaction, df4], axis=1, join='inner')
print (predictions)

```

	Product expected	Should it work
0	Nb2Se	No
1	Nb14S5	No
2	Cr2Se3	Yes
3	Cr2S3	No
4	Cr2Te3	Yes
5	V5Se4	No
6	V3S	Yes
7	V5Te4	Yes
8	Cu3Se2	No
9	Cu7S4	No
10	CuTe	No

Appendix D

Overview of Other Contributions

Outside of my work with organic fluxes, I have had the opportunity to collaborate on projects involving metathesis reactions to target ternary metal nitrides. [58, 59] Ternary metal nitrides have widespread applications including catalysts [60, 61], magnets [62], and battery materials [63, 64], so making new ternary metal nitrides could advance these technologies. However, they are an under-explored materials class as they can be difficult to make owing to nitrogen's relative inertness. [65] Therefore, non-traditional synthetic techniques are necessary. In these cases, metathesis reactions were used. Metathesis reactions are double exchange reactions that use the formation of a stable salt to drive product formation. Through the use of metathesis reactions in these systems, ternary nitrides are able to be made in bulk.

The first publication, authored by Christopher L. Rom, reported the synthesis of bulk $\text{Mg}_x\text{Zr}_{2-x}\text{N}_2$ powders ($0 < x < 1$) from metathesis reactions involving ZrCl_4 and Mg_2NCl or Mg_3N_2 . [58] As second author for this publication, I assisted with the collection of *in situ* X-ray Diffraction (XRD) data which helped elucidate the mechanism of reactivity. Since the Panalytical Empyrean diffractometer arrived at Colorado State University in 2017, I have been in charge of maintaining the instrument and training others. This means I was able to contribute expertise in collecting the *in situ* XRD data which was valuable for exploring the reaction mechanism and comparing the two precursors. It was found that both precursors progressed through the same reaction pathway with the same intermediates. The Mg_2NCl reaction initially reacted sooner than the Mg_3N_2 reaction but the product did not crystallize until 600 °C for either reaction. This work demonstrates the use of metathesis reactions to target ternary metal nitrides.

The second publication, authored by Paul K. Todd, discusses the synthesis of MgZrN_2 , Mg_2NbN_3 , and MgMoN_2 using metathesis reactions. [59] In these reactions, Mg_2NCl was reacted with the metal chloride corresponding to the desired product. For this research, I ran the magnetism measurements and completed the analysis on those data. These measurements were used to confirm the

product composition and purity as the magnetic properties of these materials are highly sensitive to impurities. This research provides additional examples of the utility of metathesis reactions to target ternary metal nitride materials.

These projects both demonstrate progress in making ternary metal nitrides. They provide examples of how metathesis reactions can be used to target phases that are traditionally difficult to make, which shows the utility of alternate synthetic techniques in solid-state chemistry. The reaction schemes explained in these publications could be expanded to other ternary metal nitrides and enable the discovery of new materials.

Appendix E

Jargon-Free Research Overview

Most of us would probably prefer a diamond ring to a graphite pencil. But both diamond and graphite are made of the same thing, carbon. How we make things is just as important as what we make them from. This is true for pretty much all solid-state materials. Solid-state materials allow us to charge our phones, harvest energy from the sun, and go to all of our zoom meetings. In order to advance these technologies we need to improve our abilities to make new solid-state materials. One big challenge preventing us from moving forward is the limited number of techniques we have to make these materials.

Imagine taking two chunks of metal, like iron and selenium, and trying to get them to combine to form a new material. Bashing them together is just going to tire you out. Solid materials by nature are not very reactive unless under extreme temperatures. For iron and selenium, you would need a specialized furnace capable of 2000 °F, which is literally the temperature of lava. Even once you achieve this temperature, simply pulling the mixture out of the furnace to cool on the counter would cause it to cool too quickly producing a useless blob similar to our metaphorical graphite. Instead, to produce the diamond we want, iron selenide must cool over the course of 4 days in the furnace. Like iron selenide and diamonds, many materials can only be made through a complex reaction scheme.

This is where my research comes in. My research focuses on using an organic compound acting as sort of a molecular mixer to enable reactivity at lower temperatures thus reducing the steps necessary to form your metaphorical diamond. Instead of taking my starting materials and heating them up to extreme temperatures, I take my starting materials along with an organic compound and heat them up to much lower temperatures around what your standard kitchen oven can reach. Once the reaction is completed it is easy to remove that organic compound leaving me with my desired material.

In the case of iron selenide, I found that the key to low-temperature reactivity was the organic compound interacting with the selenium. This simplified the preparation of iron selenide from a multi-step, 12 day process to a single-step, 5 day reaction. From this, I was able to expand to other systems showing that this reaction scheme is broadly applicable. Additionally, I demonstrated that changing the organic compound changes which material forms, which introduces tunability into solid-state reactions.

This provides solid-state chemists a new tool that can simplify the preparation of many materials and potentially enable the discovery of new materials that were previously unable to be made. This opens the door to new materials with widespread applications such as batteries with longer lifetimes, more efficient solar cells or other metaphorical diamonds we have yet to even think of.

Appendix F

Photos of Colorado

Here are a few of my favorite photos I've taken during graduate school. Enjoy!



LIST OF ABBREVIATIONS

PPh₃ - Triphenylphosphine

XRD - X-ray Diffraction

PXRD - Powder X-ray Diffraction

SCXRD - Single Crystal X-ray Diffraction

NMR - Nuclear Magnetic Resonance

PDF - Pair Distribution Function

MPMS - Magnetic Properties Measurement

PCA - Principal Component Analysis

DFT - Density Functional Theory

SVM - Support Vector Machine

MDI - Mean Decrease in Impurity

MALDI-MS - Matrix-Assisted Laser Desorption/Ionization Mass Spectrometry

FTIR - Fourier Transform Infrared

ATR - Attenuated Total Reflectance

VSM - Vibrating Sample Magnetometry

UV-Vis - Ultraviolet Visible

TEM - Transmission Electron Microscopy

EDS - Energy-Dispersive X-ray Spectroscopy

EPR - Electron Paramagnetic Resonance